Optical Single-Sideband Modulation with Tunable Optical Carrier to Sideband Ratio in Radio over Fiber Systems

Nan Song

A Thesis

in

The Department

of

Electrical and Computer Engineering

Presented in Partial Fulfillment of the Requirements

for the Degree of Master of Applied Science (Electrical and Computer Engineering) at

Concordia University

Montreal, Quebec, Canada

May, 2010

Your file Votre référence
ISBN: 978-0-494-71017-3
Our file Notre référence
ISBN: 978-0-494-71017-3

ABSTRACT

Optical Single-Sideband Modulation with Tunable Optical Carrier to Sideband Ratio in Radio over Fiber Systems

Nan Song

Radio over fiber (RoF) has been considered as a promising technology for the distribution of the future high capacity wireless signals such as ultra-wideband and millimeter-wave signals. In RoF systems, optical subcarrier modulation (SCM) is commonly used, such as optical double sideband (ODSB) modulation, and optical single sideband (OSSB) modulation. However, ODSB modulation will introduce RF signal power fading due to the fiber chromatic dispersion. To evade this problem, conventional optical single sideband (OSSB) modulation was proposed and demonstrated. Unfortunately in the conventional OSSB, the modulation efficiency, defined as optical carrier-to-sideband ratio (OCSR) in optical power, is extremely low for small modulation index, i.e. low driven voltage used. On the other hand, when high voltage is applied to the modulator, i.e. high modulation index used, the nonlinear distortion will be induced due to the nonlinearities of the optical modulator response, which will degrade the receiver

sensitivity and lead to a poor bit error rate (BER) and spurious free dynamic range (SFDR). Eventually, this will increase RoF system cost and render it impractical.

So far, suppressing the OCSR has become a popular way to improve the modulation efficiency. Lots of related techniques have been proposed and demonstrated. The objective of this thesis is to develop a simple modulation technology that OSSB modulation and tunable OCSR are obtained simultaneously only by adjusting the direct current (DC) bias of two parallel non-ideal Mach-Zehnder Modulators (MZMs).

In this thesis, the theoretical analyses to prove the functions of this modulation technique are given out first. Then by comparing the theoretical analyses with simulation results, it is found that the results are well matched. Here the impacts of imperfect situations are concerned: bias voltage drift, phase imbalance of the two parallel MZMs, mismatch of splitting and combining coupler's factors, MZM extinction ratio imbalance, inter-modulation distortions (IMDs), high order distortions and chromatic dispersion. The functions and reliability of this modulation technique are deeply discussed. Furthermore, some methods to compensate the impacts due to the non-ideal situations are also considered. Finally, the experimental results are presented to validate the proposed technique.

ACKNOWLEDGEMENTS

Here I wish to express my sincere appreciation to my supervisor Dr. John Xiupu Zhang for his help and support during my study at Concordia.

I would like to express my deep thanks and appreciation to the members of the Advanced Photonics System Lab at Concordia University, Montréal, Canada, especially Mohmoud Mohamed and Bouchaib Hraimel, without their help, I could not finish this study. Last but not the least, I would like to thank my parents for their love and support.

TABLE OF CONTENTS

LIST OF FIGURES

LIST OF TABLES

LIST OF ABBREVIATIONS

ADSL	Asynchronous digital subscriber line
AWG	Arrayed waveguide grating
BS	Base station
CATV	Cable television
CO	Central office
CW	Continuous wave
DBS	Direct broadcast satellite
DC	Direct current
DE-MZM	Dual electrode mach-zehnder modulator
DWDM	Dense wavelength division multiplexing
EDFA	Erbium doped fiber amplifier
EMI	Electromagnetic interference
FBG	Fiber bragg grating
FDMA	Frequency division multiple access
HDs	Harmonic distortion
IM-DD	Intensity modulation-direct detection
IMDs	Intermodulation distortions
IMD3	Third order intermodulation distortion

MI	Modulation index
MW	Millimeter wave
MZI	Mach-zehnder interferometer
MZM	Mach-zehnder modulator
OCSR	Optical carrier to sideband ratio
ODSB	Optical double sideband
OSSB	Optical single sideband
OTDM	Optical time division multiplexing
PD	Photo detector
RAU	Remote antenna unit
RF	Radio frequency
RHD	Remote heterodyne detection
RoF	Radio over fiber
SBS	Stimulated brillouin scattering
SCM	Subcarrier modulation
S/U-R	Sideband to undesired sideband optical power ratio
WDM	Wavelength division multiplexing

LIST OF SYMBOLS

a	Intensity division ratio of upper path in a single DE-MZM
r	Intensity division ratio of lower path in a single DE-MZM
ER	Extinction ratio
V_π	The voltage inducing π phase shift in DE-MZM
V_{RF}	Amplitude of RF signal
σ	Modulation index V_{RF} / V_π
ξ_1	Normalized DE-MZM bias V_{1DCop} / V_π
ξ_2	Normalized DE-MZM bias V_{2DCop} / V_π
t_{ff}	Insertion loss of DE-MZM
ω	The angular frequency of RF signal
θ	The initial phase of RF signal
E_0	The intensity of incident light wave from CW laser
E_1	The intensity of modulated light wave along path-1
E_2	The intensity of modulated light wave along path-2
E_3	The intensity of modulated light wave along path-3
E_4	The intensity of modulated light wave along path-4
E_{out}	The intensity of modulated light wave after the proposed modulator

$J_n(z)$	N-th order Bessel function
$\Re$	Responsivity of PD
k_{in}	Splitting factor (front coupler)
k_{out}	Combining factor (rear coupler)

Chapter 1

Introduction

1.1 Introduction

Recently, wireless communication plays an important role in telecommunication. However, due to the demand of high quality service like high definition video conference, and internet data transferring increase considerably, the capacity of the current narrowband wireless access networks is insufficient. Therefore it is deeply necessary to figure out how to increase the capacity of wireless systems.

One natural way to increase the capacity of wireless communication systems is increasing the carrier frequencies. Higher carrier frequencies offer greater modulation bandwidth, but may lead to increased costs of radio front-ends in the base stations. In conventional wireless communication systems, the medium for transmission channel is atmosphere. However, radio signals with high frequencies will attenuate greatly when propagating over air, especially the penetration ability of going through obstacles into building will decrease extremely. When millimeter-wave signals at the frequency of 60 GHz propagate in the air, the atmosphere attenuation can be as high as 10-15 dB/km. In other words, if we transmit typical radio signal at 60 GHz directly over the air, it will only be able to propagate for less than 2 km.

Another way to increase capacity of wireless communication systems is to deploy smaller cells (micro-cells and pico-cells) [3] [4]. However, smaller cell size means that a large number of base stations is needed in order to achieve the wide coverage required of

ubiquitous communication systems. Furthermore, extensive feeder networks are needed to service the large number of base stations. Therefore, unless the cost of the base stations and the feeder network are significantly low, the system-wide installation and maintenance costs of such systems would be rendered prohibitively high. This is where Radio-over-Fiber (RoF) technology comes in. It achieves the simplification of the base stations through consolidation of radio system functionalities at a centralized head end, which is then shared by multiple base stations.

RoF technology combines the advantages of optical fiber communication by its super broad bandwidth, lower signal attenuation, and small signal distortion; and the advantages of wireless communication by its flexibility. Therefore, RoF systems enable high capacity and more than 1 Gbit/s ultra-band wireless access in an effective cost manner. Furthermore, digital baseband and RF analog signals both can be transmitted in RoF system, and realize the convergence of wireless access and fixed access. Until now, RoF systems have attracted tremendous research interests, and the main issue is how to obtain the good performance of RoF system. So far, lots of techniques concerned have been proposed and demonstrated to improve the modulation efficiency which is the crucial parameter to influence the performance of RoF. For instance, Brillouin [5], external optical filtering [6][7][8] and optical attenuation [9], but all of them will increase the complication of RoF systems considerably.

Furthermore, RoF systems are an enabling technology, which will allow telecommunications companies to relay digital baseband and RF analog signals, such as WiFi, WiMax and mm-wave through the wide bandwidth of fiber in a cost effective

manner. RoF systems make use of SCM and frequency division multiple access (FDMA), so it is inherently able to transport synchronous and asynchronous communication data. The main issue is to accurately recuperate the transmitted RF signals, which is where the issue of system nonlinearity plays a monumental role. The nonlinearity arises mainly from the frequency response of the optical transmitter, and receiver, along with other optical components, such as fiber. For example, the Mach-Zehnder modulator (MZM) has a sinusoidal frequency response, which will produce an optical transmission with nonlinearities. In situations where composite multiple RF channels need to be transmitted, higher-order distortion may be induced by nonlinearities in RoF systems, and thus these higher order distortion components will lead to lower SNR for neighboring channels. Optical system designers typically would have to install expensive optical filters, increase optical transmission power or unequally space RF channels allocations to increase SNR, which would undoubtedly increase complexity and cost. It is known that in the case of analog transport, there is a steady decline in performance due to nonlinear distortion, while for digital transport there is a constant performance until it is overcome by quantization noise and synchronization loss. Beyond this point there is a dramatic performance loss. This indicates that digital communication transport is a better choice for long haul transmission systems, and analog communication transport is a better choice for short haul transmission systems or as an access network, because of the gradual decline in performance and lower cost, so optical system designers are opting to use them together [10].

1.2 RoF Technology

1.2.1 RoF Architecture

Basically, RoF is a technology that entails the use of optical fiber links to distribute RF signals from a central office (CO) to base stations (BS). Figure 1.1 shows the general RoF architecture, where each simple base station is connected back to the central office through optical fibers. Any wireless service may be received by the transceiver and the RF signal will be modulated onto a specific optical carrier allotted to that specific base station. Many optical carriers may be modulated and then optically coupled together before being transmitted back to the central station [11].

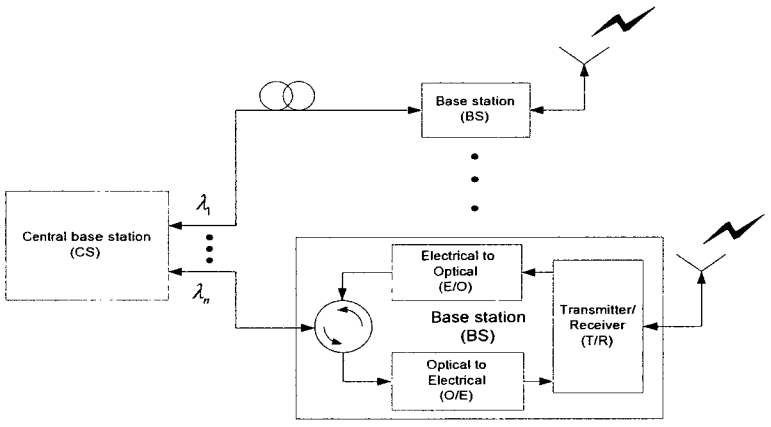

Figure 1.1 Block diagram of a RoF broadcast architecture

In traditional narrowband wireless communication systems, RF signal processing functions, such as frequency up-conversion, carrier modulation, and multiplexing, are performed at the base stations, then immediately fed into the antennas. On the contrary, RoF makes it possible to centralize the RF signal processing functions in one shared

location (central office), and then use optical fiber with low-loss (0.2 dB/km for 1550 nm, and 0.5 dB/km for 1310 nm wavelengths) to distribute the RF signals to the remote base stations. Thus, base stations are simplified significantly, as they only need to perform optoelectronic conversion, amplification, emitting and receiving functions. The centralization of RF signal processing functions enables equipment sharing, dynamic allocation of resources, and simplified system operation and maintenance. These benefits can translate into major system installation and operational savings, [12], especially in wide-coverage broadband wireless communication systems, where a high density of base stations is necessary as discussed above.

1.2.2 Advantages of RoF Technology

Some of the advantages and benefits of the RoF technology are given below.

a. Low attenuation loss

Commercially available standard single mode fibers which are made of glass (silicon dioxide) have attenuation of below 0.2 dB/km and 0.5 dB/km in the 1550 nm and the 1310 nm windows, respectively. We have mentioned the situation of RoF over the air above. Obviously, it is not suitable for being the transmission medium when RF signals' frequencies increase greatly. As another common type of transmission medium, coaxial cables' losses are higher by three orders of magnitude at higher frequencies. For instance, the attenuation of a 0.5 inch coaxial cable (RG-214) is higher than 500 dB/km for carrier of above 5 GHz [13]. Therefore, by transmitting microwaves in the optical fiber,

transmission distances are increased several folds and the required transmission powers are reduced greatly.

b. Large bandwidth

Optical fibers offer enormous bandwidth. There are three main transmission windows, which offer low attenuation, namely the 850 nm, 1310 nm, and 1550 nm wavelengths. For a SMF, the combined bandwidth of the three windows is in the excess of 50 THz. However, today's state-of-the-art commercial systems utilize only a fraction of this capacity (1.6 THz). But the developments to exploit more optical capacity per single fiber are still continuing. The main driving factors towards unlocking more and more bandwidth out of the optical fiber include the availability of low dispersion (or dispersion shifted) fiber, the Erbium Doped Fiber Amplifier (EDFA) for the 1550 nm window, and the use of advanced multiplex techniques namely Optical Time Division Multiplexing (OTDM) in combination with Dense Wavelength Division Multiplexing (DWDM) techniques. The enormous bandwidth offered by optical fibers has other benefits apart from the high capacity for transmitting microwave signals. The high optical bandwidth enables high speed signal processing that may be more difficult or impossible in electronic systems. In other words, some of the demanding microwave functions such as filtering, mixing, up- and down-conversion, can be implemented in the optical domain [14]. For instance, mm-wave filtering can be achieved by first converting the mm-wave signal into an optical signal, then performing the filtering in optical domain by using optical components such as the Mach Zehnder Interferometer (MZI) or Fiber Bragg

Gratings (FBG), and then converting the filtered signal back into electrical form. Furthermore, processing in the optical domain makes it possible to use cheaper low bandwidth optical components such as laser diodes and modulators, and still be able to handle high bandwidth signals [15]. The utilization of the enormous bandwidth offered by optical fibers is severely hampered by the limitation in bandwidth of electronic systems, which are the primary sources and receivers of transmission data. This problem is referred to as the "*electronic bottleneck*". The solution around the electronic bottleneck lies in effective multiplexing. OTDM and DWDM techniques mentioned above are used in digital optical systems. In analogue optical systems including RoF technology, Subcarrier Modulation (SCM) is used to increase optical fiber bandwidth utilization. In SCM, several microwave sub carriers, which are modulated with digital or analogue data, are combined and used to modulate the optical signal, which is then carried on a single fiber [16], [17]. This makes RoF systems cost-effective.

c. Immunity to radio frequency interference

Immunity to Electromagnetic Interference (EMI) is a very attractive property of optical fiber communications, especially for microwave transmission. This is so because signals are transmitted in the form of light through the fiber. Because of this immunity, fiber cables are preferred even for short connections at mm-waves. Related to EMI immunity is the immunity to eavesdropping, which is an important characteristic of optical fiber communications, as it provides privacy and security.

d. Easy installation and maintenance

In RoF systems, complex and expensive equipment is kept in the central office, thereby making the BSs simpler. For instance, most RoF techniques eliminate the need for a LO and related equipment at the BSs. In such cases a photo detector, an RF amplifier, and an antenna make up the BS. Modulation and switching equipment are kept in the central office and is shared by several BSs. This arrangement leads to smaller and lighter BSs, effectively reducing system installation and maintenance costs. Easy installation and low maintenance costs of BSs are very important requirements for mm-wave systems, because of the large numbers of the required BSs.

e. Reduced power consumption

Reduced power consumption is a consequence of having simple BSs with reduced equipment. Most of the complex equipment is kept in the central office. In some applications, the BSs are operated in passive mode. For instance, some 5 GHz Fiber-Radio systems employing pico-cells can have the BSs operated in passive mode [18]. Reduced power consumption at the remote antenna unit (RAU) is significant considering that BSs are sometimes placed in remote locations not fed by the power grid.

f. Dynamic resource allocation

Since the switching, modulation, and other RF functions are performed at a central office, it is possible to allocate capacity dynamically. For instance in a RoF distribution system for GSM traffic, more capacity can be allocated to an area (e.g. shopping mall) during

peak times and then re-allocated to other areas when off-peak (e.g. to populated residential areas in the evenings). This can be achieved by allocating optical wavelengths through Wavelength Division Multiplexing (WDM) as need arises [19]. Allocating capacity dynamically as need for it arises obviates the requirement for allocating permanent capacity, which would be a waste of resources in cases where traffic loads vary frequently and by large margins [12]. Furthermore, having the central office facilitates the consolidation of other signal processing functions, such as mobility functions, and macro diversity transmission [19].

1.3 Generating and Distribution of RF Signals over Fiber

Over the past few years, a lot of researches have been carried out to generate radio signal optically. RoF techniques may be classified in terms of the underlying modulation/detection principles employed. In that case, the techniques may be grouped into three categories, namely Intensity Modulation-Direct Detection (IM-DD), Remote Heterodyne Detection (RHD) [20], and harmonic up-conversion techniques. IM-DD is the simplest method and also the most widely used at present. Not only the modulation techniques discussed below but also our considered modulation technique belongs to this category. SCM is another principal technique which is used extremely widely in RoF systems. This technique can help RoF make full use of the sufficiency optical fiber bandwidth.

In IM-DD modulation scheme, the RF signal is directly modulated onto the optical carrier by an intensity modulator, and then recovered by direct detection at the photo detector. The optical modulation is divided into two kinds: direct modulation and external

modulation. The former one is to directly drive the current of semiconductor laser with the RF signal, while the latter is to modulate the RF signal onto the continuous wave (CW) emitted from laser source using an external modulator such as the Mach-Zehnder Modulator (MZM). The two options are shown in Fig.1.2. In both cases, baseband data is mixing with the RF carrier named first modulation, and then the hybrid RF signal is modulated on the optical carrier which we call it second modulation.

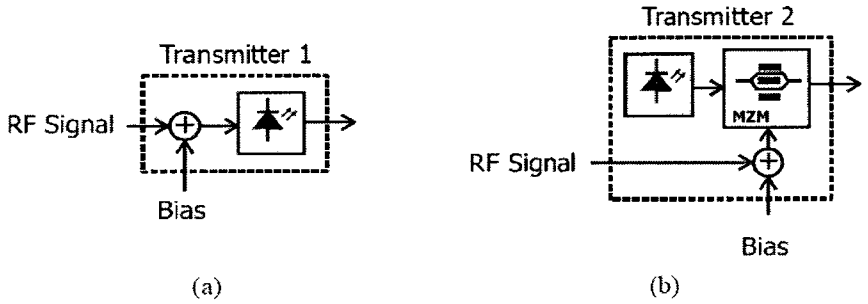

Figure 1.2 Electro-optic modulation schemes, (a) internal modulation; (b) external modulation

Evidently, direct intensity modulation is, in principle, simpler than external modulation. It is used frequently in low data rate case in order to reduce cost. The limiting factor to its use is the modulation bandwidth of the laser. Relatively simple semiconductor lasers can be modulated to frequencies of several giga-hertz, say 5-10 GHz. That is why at higher microwave frequencies like above 10 GHz, external modulation rather than direct modulation is applied.

In the RHD links, two phase-correlated optical carriers are generated in a dual-frequency laser transmitter with a frequency offset equal to the desired millimeter-wave (MW) frequency. Both optical signals are then transmitted by heterodyning of the two

optical signals in a photodiode [20]. Based on RHD, the fiber-optic technology can offer radio-system functionalities such as modulation and frequency conversion in addition to transparent signal transport.

A summary reviewing two modulation schemes for transporting RF signal over fiber is shown in Table 1.1

Table 1.1 Comparison of transporting RF signal methods

Schemes	Advantages	Disadvantages
IM-DD	Low cost, simple structure	Due to fiber chromatic dispersion the transmission distance is limited
RHD	No limitation on the generated frequency	Higher complexity and cost, phase correlated problem

1.4 Optical Single Sideband and Optical Double Sideband Modulation

At present, in RoF system, the most commonly used modulation schemes are optical single sideband (OSSB) and optical double sideband (ODSB), which are showed in Fig. 1.3.

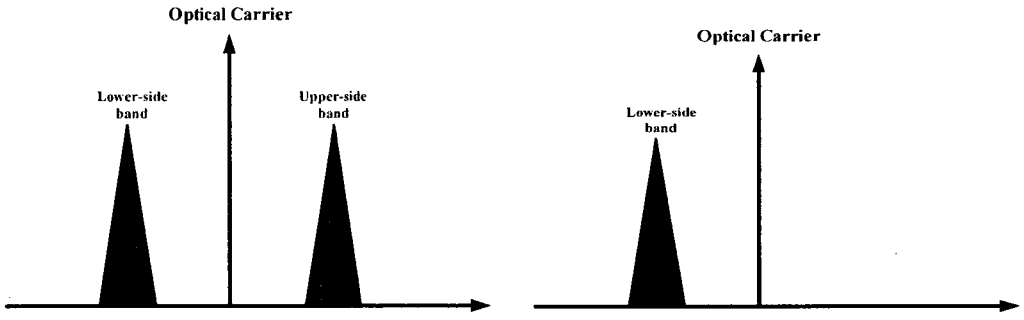

(a) (b)

Figure 1.3 (a) Optical double sideband (ODSB), (b) optical single sideband (OSSB)

In Fig. 1.3(a) it is found that in ODSB case, RF signal is modulated on the optical carrier, and two sidebands upper and lower than the optical carrier in frequency domain are generated respectively. While in Fig. 1.3(b), only the lower optical sideband is generated for OSSB modulation. Generally, ODSB can be realized by employing a single-electrode MZM, while typical OSSB is generated by employing a dual-electrode MZM (DE-MZM) [6]. ODSB and OSSB both can be used in RoF system. However, it is well known that OSSB is not degraded by RF power fading when transmitted through dispersive fiber, while ODSB will experience periodic power fading that is dependent on fiber length, chromatic dispersion and RF carrier frequency [21]. The power fades occur because of the use of SCM, which generates two optical sidebands that are at different propagation delays through dispersive fiber. This propagation delay will translate into a differential phase shift between the two sidebands. For example, set the RF carrier to frequency of 12 GHz and the fiber attenuation is compensated. In the case of OSSB modulation there is almost no RF carrier power fade, but in ODSB case there are two RF carrier power fades

occurring at 26.97 and 80.91 km of the 100 km fiber length [22]. Therefore OSSB modulation scheme attracts more interests in RoF links in order to overcome the power fading effect caused by fiber dispersion.

A summary reviewing two techniques for generation mm-wave signal and transmission over fiber link is shown in Table 1.2.

Table 1.2 Comparison of harmonic generation techniques using external modulation

Schemes	Advantages	Disadvantages
DSB	Support high frequency RF signal	Suffer from the fiber chromatic dispersion
SSB	Free fiber chromatic dispersion	Low modulation efficiency, high local oscillator frequency

1.5 Sub-carrier Modulation in RoF Systems

SCM is transmitting several analog or digital subcarrier-multiplexed RF channels over only one fiber link or network [8]. It is a maturing, simple and cost effective approach for exploiting optical fiber bandwidth in RoF systems. For many applications, it is quite advantageous to use this technique. These applications include: CATV (cable TV), interfacing wireless networks, microwave photonic systems, and transmitting control

information for optical packet switching. In SCM, multiple RF signals are used to modulate an optical carrier at the transmitter's side. In this thesis, maximally two sub-carriers are multiplexed to help us to investigate how SCM influences the system's performance. Fig. 1.3 illustrates what SCM is.

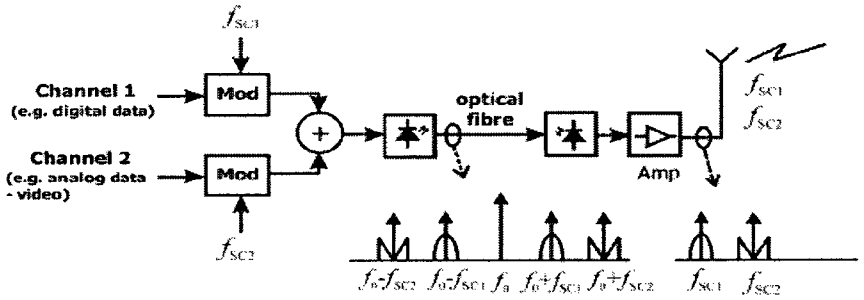

Figure 1.4 Sub-carrier modulation of mixed digital and analogue signals

To transmit multiple RF channels by only one optical carrier, multiple sub-carriers are first combined and then used to modulate the optical carrier as shown in Fig. 1.4. At the receiver's side the sub-carriers are recovered through direct detection and then radiated. Different modulation schemes may be used on separate sub-carriers. One sub-carrier may carry digital data, while another may be modulated with an analogue signal such as video or telephone traffic. In this way, SCM supports the multiplexing of various kinds of mixed mode broadband data. Modulation of the optical carrier may be achieved by either directly modulating the laser, or by using external modulators such as the MZM. In this thesis, MZMs are used.

1.6 Harmonic and Inter-modulation Distortions

Since RoF involves analogue modulation, and detection of light, it is fundamentally an analogue transmission system. Therefore, signal impairments such as noise and distortion, which are important in analogue communication systems, are important in RoF systems as well. These impairments tend to limit the performance of the RoF system.

There are a lot of sources of interference like shot noise, thermal noise, chromatic dispersion, although, nonlinear distortion is the dominant factor among all the harmful factors. Let's take an example for the systems in which MZM is used. MZM has a squared cosine transfer function in power. In another word, it has a nonlinear transfer function. When RF signals are applied to modulate the optical carrier in MZM, nonlinear distortions including harmonics distortions (HDs) and inter-modulation distortions will be generated. First, HDs mainly depends on modulation index (MI), which means more power of input signal, more power of HDs; the increase of MI will lead to the nonlinearity increase, so the intensities of HDs will become larger and larger. Second, intermodulation distortions (IMDs) are principally determined not only by MI, but also by the number of RF carriers. As MI increases, the intensities of IMDs will become more and more serious; as the number of RF carriers increase, every RF sub-carrier can inter-modulate with each other, the intensities of IMDs will increase also. Therefore, as multiple like two or more RF carriers are used to modulate the optical carrier, we need to consider the IMDs.

Theoretically, there are unlimited numbers of high order optical spectral components including HDs and IMDs after light wave modulated by RF signals. Due to the limited

bandwidth of the optical equipment like multiplexer, EDFA, photodetector and etc, the high order distortions will be filtered out. Therefore, those low order nonlinear distortions make great contribution to degrade the system's performance.

Compared with other low order nonlinear distortions, the third order IMDs (IMD3) are the most difficult to be filtered out by optical filters because they are very close to the fundamental spectral component. IMD3 may bring devastating impact on the receiver's sensitivity and the system's dynamic range if we can't handle this very well.

1.7 Technique Survey of OCSR Improvement

As mentioned before, in RoF systems, the main issue is obtaining good performance of the systems. In OSSB technique which is robust to fiber chromatic dispersion and is commonly chosen in RoF systems, when high power of RF signal is modulated onto the optical carrier by DE-MZM, considerably harmful nonlinear distortions, i.e. HDs and IMDs, are generated in the system due to the nonlinear modulation characteristic of DE-MZM. While when we choose small power RF signal to be modulated, the nonlinear distortion products can be reduced, however, very low modulation efficiency can be obtained [23]. Actually, low modulation efficiency means the waste of the system resource, and it can reduce the quality of the recovered RF signal. When the power of RF sideband is much lower than the optical carrier after modulation, the detected RF signal power will be small and this can degrade the signal to noise ratio.

To improve the performance of RoF transmission systems, the power of RF signal carried on optical carrier can be boosted by using the high power light sources or utilizing the optical amplifier [8]. However these techniques also increase the average optical power to the photo detector (PD) simultaneously. Due to the high incident optical power, the harmonic distortions, reduced responsivity, and the damage to PD can be caused to this semiconductor device [6][7][8].

So far, suppressing the optical carrier to sideband ratio has become a popular way to improve the modulation efficiency. Lots of techniques concerned have been proposed and demonstrated. For instance, external optical filtering [6][7][8], stimulated Brillouin scattering [5] and optical attenuation [9].

1.7.1 External Optical Filtering Technology

For external optical filtering technology, the main principle is removing the excessive power of optical carriers [6][7].

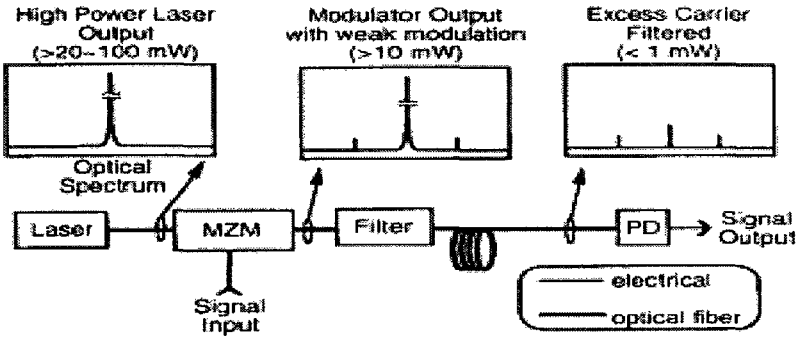

Figure 1.5 All-optical insertable technique to increase the efficiency of a typical fiber-optic system [6]

Fig. 1.5 shows the scheme of suppressing OCSR technology by the external optical filter. This technology is utilized in ODSB modulation, and the suppressing OCSR is implemented by filtering the optical carrier (Fabry-Perot filter), then increasing the optical power by a gain G_{opt} to yield the same PD current [6]. This technology can obtain 9-13 dB improvement of OCSR and especially useful for remote sensing of weak RF signals or in signal processing systems (e.g., finite impulse response filters) that unnecessarily add excess carrier, however the main issue with this method is the extra optical and electrical devices will introduce distortions into RF signal which will degrade the performance of RoF system considerably. Moreover, because ODSB is used that the transmission will experience power fading at periodic fiber length, which will require an automatic gain control at the receiver and more cost for the RoF system.

1.7.2 Stimulated Brillouin Scattering Technology

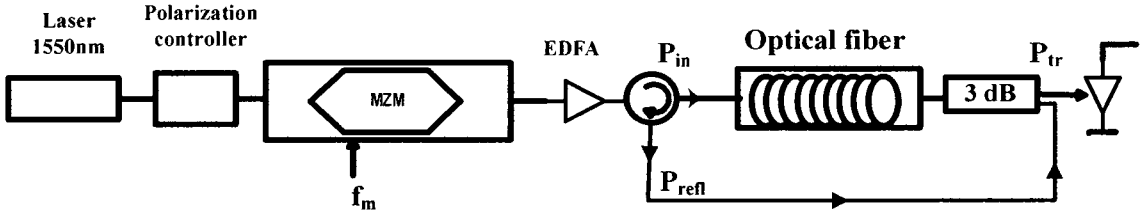

Figure 1.6 Experiment setup: multiple pass of Stokes wave in optical fiber [5]

Traditional stimulated Brillouin scattering (SBS) is used to increase the modulation depth of a weakly-modulated optical signal to improve the modulation efficiency. By rejecting the forward travelling carrier power and allowing the modulation sidebands to pass with

low loss, SBS technology realizes the suppressing OCSR. However it is found that SBS need high input power and induce system degradations. Furthermore, the process of SBS is unstable and noisy [5]. Later, a new method is proposed which is shown in Fig. 1.6. In this technology, an optical pump entering the optical fiber generates an acoustic grating moving in the direction of pump, which gives rise to backscattering of the optical pump (the so-called Stokes wave) frequency-downshifted from the pump. It results in a lower Brillouin threshold (6mW) than with a single pass configuration (20mW). Modulation depth enhancement is then even observable without the need for high input powers. The multiple-pass configuration also has better depletion efficiency because of the improved grating stability [5]. Nevertheless, the main drawback of this technology is the complexity and high cost. Moreover, because ODSB is used in this technology, the transmission will also need an automatic gain control to stabilize power fluctuations at the receiver, which will incur added system expense.

1.7.3 Optical Attenuation Technology

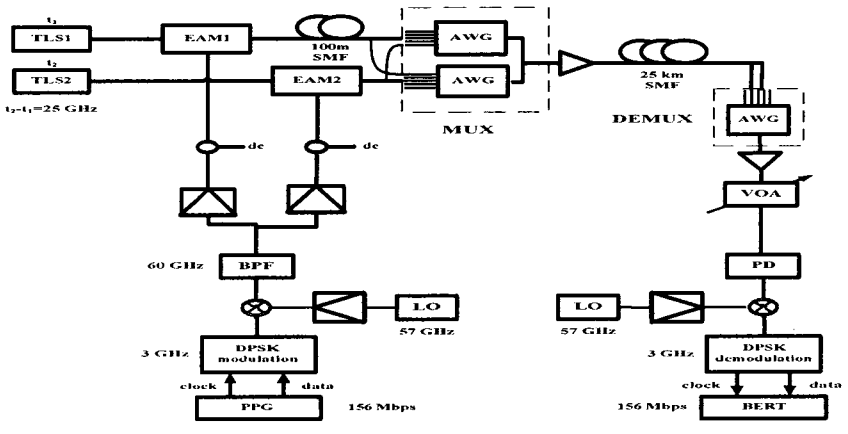

Figure 1.7 Experiment setup of DWDM multiplexing scheme [9]

In [9], a DWDM multiplexing scheme using an arrayed-waveguide grating (AWG) for optically frequency interleaved 60-GHz band radio-on-fiber systems is proposed and demonstrated. As shown in Fig. 1.7, the two parallel AWGs are tuned so that the carrier and one of the sidebands of each input channel are filtered out to the output waveguides respectively which realize the OSSB, then after demultiplexing by the single AWG, the carrier was suppressing almost 10 dB. In this technology, the AWG is utilized to attenuate the optical carrier to realize the suppressing OCSR, and no noticeable power penalty is observed after 25-km SMF transmission due to the OSSB modulation and interchannel interference. However, the complexity of the system, cross-talk and fixed permutation of input light-paths according to the wavelength will limit the RoF system.

1.7.4 Low Bias MZM Technology

Recently, a distinct way to suppress the OCSR is proposed by using a low bias MZM [24].

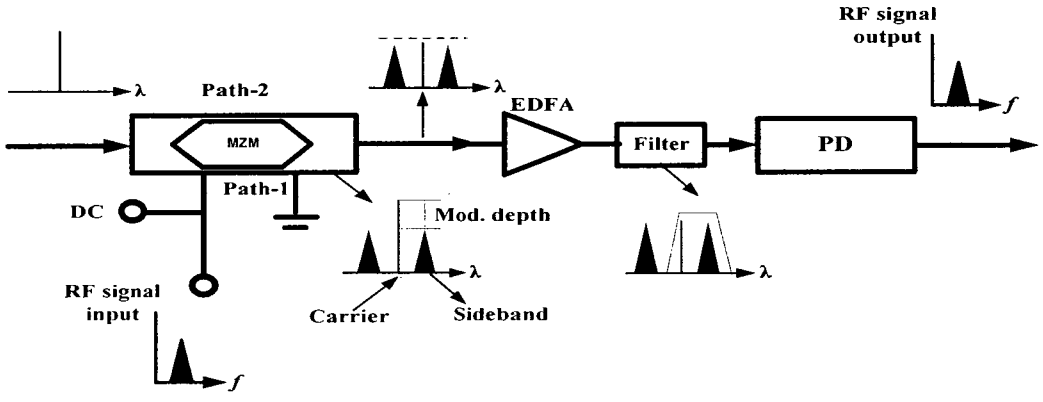

Figure 1.8 MZM with adjustment of DC-bias voltage [24]

Fig. 1.8. shows the scheme of a MZM with an adjustment of DC bias for the different optical path. When an RF signal is input through the DC bias-T to the MZM, light in path-1 is phase-modulated by the RF signal. At the output port, because path-2 is not modulated by an RF signal, interference between two paths only happens at the central carriers. Therefore, even if the modulation depth of path-1 is very low, we can adjust the DC bias voltage of the MZM to obtain a carrier with the same power level as the sidebands [24]. This method uses ODSB modulation and suppresses the OCSR enormously only by adjusting the DC bias, which is effective to obtain a large range of OCSR without utilizing other optical or electrical components. However, the main disadvantage is that this technique is only available for ODSB modulation scheme, which is extremely vulnerable to chromatic dispersion and degrades the performance of the RoF system.

Later, a new modulation technology that can realize OSSB with tunability of the OCSR simultaneously to improve the performance of RoF systems has been proposed by Minhong Zhou [25]. In this technique, two parallel MZMs are used to achieve OSSB; meanwhile, by adjusting the DC bias, it can obtain the tunable OCSR. Besides the large range of OCSR, this method is robust to the power fading because of the OSSB modulation. However, only the theoretical analysis and simulation results in ideal situations (ideal connect, matched extinction ratio of MZMs and no bias shift, etc) are shown in the thesis. In addition, the feasibility of this technology is not demonstrated.

1.8 Motivation and Research Problem

As stated in 1.7, suppressing the optical carrier to sideband ratio has become a popular way to improve the modulation efficiency. Lots of techniques concerned have been proposed and demonstrated, like Brillouin [5], external optical filtering [6][7][8] and optical attenuation [9]. However, all of these technologies have one common disadvantage, which increase the complexity of the RoF systems considerably, and inherently introduce more harmful distortions. There also is a new technology which can suppress the OCSR enormously without utilizing other optical or electrical components. Unfortunately, this technique is only available for ODSB modulation scheme, which is not spectrally efficient and will experience the power fading when transmission.

Recently, Zhou [25] proposed a new technology which can realize OSSB modulation and also the tunable OCSR simultaneously to improve the performance of RoF systems. In Zhou's thesis, only ideal MZMs are considered. Therefore it is worth comprehensively studying the technique considering non-ideal MZMs. In this thesis, a theory considering non-ideal MZMs are developed. The technique using non-ideal MZMs is simulated and compared to the theory. Finally the technique is experimentally verified. Consequently, this work is considered extension and further investigation for Zhou's technique.

1.9 Thesis Outlines

Chapter 1 provides the reader with background information of RoF systems being widely used today and explains the motivation for the research topic. The low efficient modulation issue in RoF systems and how it affects the system performance have been described. Moreover, a detailed review of current technologies to improve modulation efficiency has been given in this section. Also discussed are the differences between the ODSB and OSSB modulation schemes with the invulnerable to power fading advantage of OSSB modulation.

In Chapter 2, the principle of the considered modulation technique which can obtain OSSB with tunable OCSR simultaneously is presented. This section will discuss the principle of OSSB generation using two parallel MZMs and provide the mathematical formulations for it. In addition, the expressions of tunable OCSR, optimum OSCR, RF output power and IMDs are given out and theoretically analyzed in detail.

In Chapter 3, by using VPItransmission Maker software, the theoretical analyzed results of OCSR, RF output power and IMDs are verified by the simulations. Since this system is heavily depends on the bias voltage, therefore the impact of bias shift, coupler factor imbalance, modulator extinction ratio imbalance and phase imbalance are also considered in this part. Moreover, the impact of chromatic dispersion to this considered modulation technique is also presented by replacing the ideal connection with SMF.

In Chapter 4, this technique is experimentally investigated to verify the concept. Furthermore, the differences among the experimental, theoretical and simulated results are discussed.

Chapter 5 concludes the thesis with the amount of progress that was accomplished and potential implication to knowledge, theory and practice. Also discussed is future work that remains and over all insights.

Chapter 2

Theoretical Analysis of

Considered Modulation Technique

2.1 Introduction

As previously stated in Chapter 1, suppressing the optical carrier to sideband ratio has become a popular way to improve the modulation efficiency. And thus, many implementation approaches have been reported. However, all of these techniques have one common disadvantage, which increases the complexity and cost of the RoF systems considerably. Therefore, in this chapter, a new OSSB modulation technique with tunable OCSR to improve the performance of RoF systems is considered. In addition, the variable OCSR and optimum one to get maximum RF output power is presented. Furthermore, the mathematical formulations of RF output power and inter-modulation distortions are also given out.

This chapter is organized as follows, Section 2.2 will describe the considered modulation technique, and Section 2.3 will give the detail of how to obtain the OSSB. Moreover, theoretical analyses of OCSR, RF output power and IMDs are presented when only one RF signal applied and two RF signals applied respectively. In Section 2.4 some conclusions will be drawn.

2.2 Principle of the Considered Modulation Technique

Fig. 2.1 shows the schematic of the considered modulator. As shown in Fig. 2.1, the injected light is split into two branches A and B by an optical splitter. In each branch there is a DE-MZM, i.e. MZM-1 in branch A and MZM-2 in branch B. After optical modulation, the two branches are combined by another optical combiner. In each MZM, there are three ports, i.e. one RF port and two DC bias ports as shown in Fig. 2.1. Without loss of the generality, it is assumed that the two MZMs are identical. To obtain OSSB, it is required that the phase difference between the two RF ports of the MZM-1 and MZM-2 must be $\pi/2$ and thus the voltage difference between 1DC and 2DC ports must be $V_\pi/2$, where V_π is the π-shift voltage of the MZM. In other words, the phase difference of $\pi/2$ between path-2 and path-4 is required to be maintained. It can be assumed that the bias voltage at 1DC port is zero, and thus the bias voltage at 2DC port is $V_\pi/2$, i.e. V_{1DC}=0, and V_{2DC}= $V_\pi/2$.

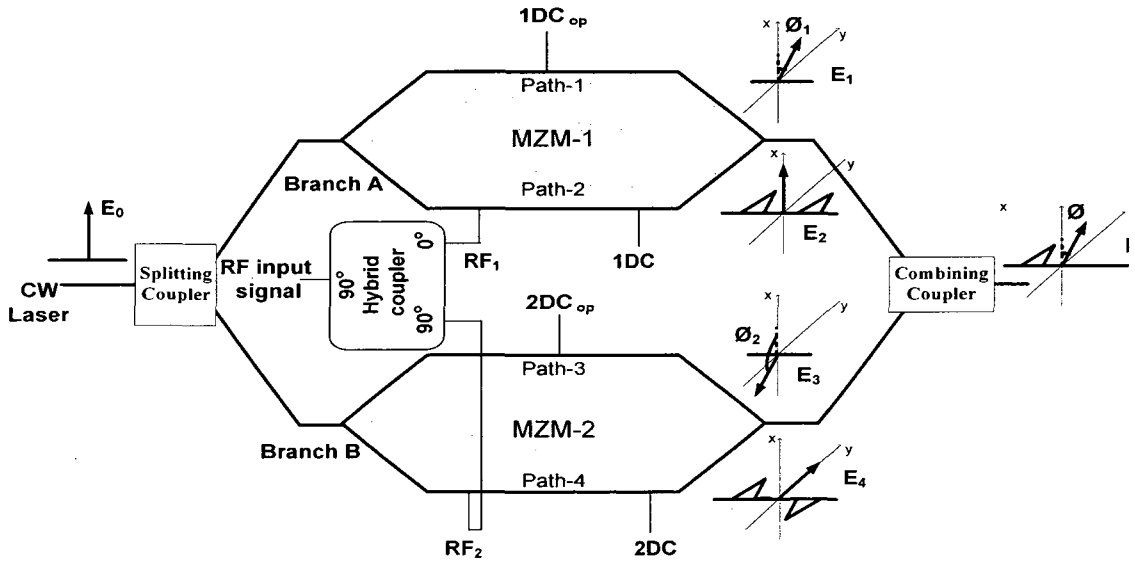

Figure 2.1 Considered optical OSSB modulator with tunable of optical carrier to sideband ratio

The operation mechanism of the considered modulator is given as follows. The biases $V_{1DC_{OP}}$ and $V_{2DC_{OP}}$ at port $1DC_{op}$ and $2DC_{op}$, respectively, are used to control the phase difference of the optical carrier between path-1 and path-3. Thus the power of the optical carrier can be altered by these two voltages. In path-2 and path-4, RF signals are phase modulated on the optical carrier to generate two first-order sidebands, and the upper sidebands (in frequency domain) for path-2 and path-4 are 180 degree out of phase. Thus a single sideband modulation is obtained because the two upper sidebands are cancelled when the double sidebands at output of MZM-1 and MZM-2 are combined as shown in Fig. 2.1.

2.3 Theoretical Analysis of the Considered Modulation Technique

2.3.1 Theoretical Analysis for the Modulator Driven by One RF Signal

It is assumed that the initial optical field is $E(t) = E_0 e^{i\omega_c t}$, where ω_c is the angular frequency of optical carrier, and E_0 is the amplitude of the optical field.

Consider one RF signal $\sqrt{2}V_{RF}\cos(\omega t + \theta)$, with a frequency of ω, arbitrary phase θ and amplitude of V_{RF} driving the modulator, and the splitting and combining coupler's factor both are 3 dB. After mathematical manipulations, the output electric field from the modulator is obtained (detailed derivation given in Appendix A)

$$E_{out}(t)=\frac{\sqrt{t_{ff}}}{2}E_0e^{i\omega_c t}\left\{ae^{i\xi_1\pi}+ae^{i\xi_2\pi}+r\sum_{n=-\infty}^{\infty}\left[J_n(\sigma\pi)e^{in(\omega t+\theta)}\left((-i)^n-i^{2n+1}\right)\right]\right\} \quad (2.1)$$

where t_{ff} represents the insertion loss of the MZM, a represents the power split ratio of upper branch of the MZM, $r=\sqrt{1-a^2}$ represents the power split ratio of lower branch, $\sigma=\frac{V_{RF}}{V_\pi}$ is defined modulation index, and $\xi_1=\frac{V_{1DC_{op}}}{V_\pi}$ and $\xi_2=\frac{V_{2DC_{op}}}{V_\pi}$ are normalized DC-voltages at $1DC_{op}$ and $2DC_{op}$ ports, respectively.

Note that when $n=0$ in Eq. (2.1), the electric field in Eq. (2.1) is simplified to $E_{out}=\frac{\sqrt{t_{ff}}}{2}E_0e^{i\omega_c t}\left[ae^{i\xi_1\pi}+ae^{i\xi_2\pi}+\sqrt{2}rJ_0(\sigma\pi)e^{-i\frac{\pi}{4}}\right]$, i.e. optical carrier. When $n=1$, the electric field in Eq. (2.1) become 0, i.e. the electric field of the upper sideband $E_{+\omega}=0$. When $n=-1$, the lower sideband electric field from Eq. (2.1) is given by $E_{-\omega}=\sqrt{t_{ff}}E_0e^{i\omega_c t}rJ_{-1}(\sigma\pi)e^{-i(\omega t+\theta-\frac{1}{2}\pi)}$. The above suggests that a single sideband modulation is obtained. However, if the bias voltages at 1DC and 2DC ports are exchanged, then the upper sideband will be obtained and the lower sideband will be eliminated.

OCSR is defined by the optical power of the optical carrier to the optical power of the optical subcarrier or sideband. With the help of Eq. (2.1), OCSR can be given by (detailed derivation see Appendix A),

$$OCSR=\frac{a^2+a^2\cos(\xi_1-\xi_2)\pi+r^2J_0^2(\sigma\pi)+arJ_0(\sigma\pi)\left[\cos\xi_1\pi+\cos\xi_2\pi-\sin\xi_1\pi-\sin\xi_2\pi\right]}{2r^2J_1^2(\sigma\pi)} \quad (2.2a)$$

For the imperfect situations that optical combining and splitting coupler's factors are mismatch and two parallel MZMs modulator extinction ratios (ER) are different, it is simply to define the splitting (front coupler) coupler's factor as k_{in}, combining (back coupler) coupler's factor as k_{out}, MZM-1 modulator ER as ER_1 and MZM-2 modulator ER as ER_2, then the OCSR can be re-written by (detailed derivation given in Appendix A),

$$OCSR = \frac{\left\{\begin{array}{l} c^2f^2k^2 + p^2g^2h^2 + 2pcfghk\cdot\cos(\xi_1-\xi_2)\pi \\ +2J_0(\sigma\pi)\left[pbg^2h^2\cdot\cos(\xi_1\pi) + ghbcfk\cdot\cos(\xi_2\pi) - pdfkgh\cdot\sin(\xi_1\pi) - f^2k^2cd\cdot\sin(\xi_2\pi)\right] \\ +(d^2f^2k^2 + b^2g^2h^2)J_0^2(\sigma\pi) \end{array}\right\}}{\left\{(dfk+bgh)^2\cdot J_1^2(\sigma\pi)\right\}} \quad (2.2b)$$

where $h = \sqrt{k_{in}}$, $k = \sqrt{1-k_{in}}$, $f = \sqrt{k_{out}}$, $g = \sqrt{1-k_{out}}$, $p = \frac{1+\sqrt{ER_1}}{\sqrt{2(ER_1+1)}}$, $b = \sqrt{1-p^2}$, $c = \frac{1+\sqrt{ER_2}}{\sqrt{2(ER_2+1)}}$, and $d = \sqrt{1-c^2}$. The parameters h and k represent the power split ratio of the splitting coupler, f and g represent the power split ratio of the combining coupler, p and b represent the power split ratio of upper and lower path of MZM-1 respectively, and c and d represent the power split ratio of upper and lower path of MZM-2 respectively. It is obvious that OCSR depends on the coupler's factor and MZMs ER. Moreover, it is noted that when the parameter h equals to f for any value, i.e. 0.1, 0.2 and 0.3 etc. the OCSR is independent of the coupler's factor, and only the ER impacts the OCSR.

Now consider the current of RF signal after the photodetector. It is assumed that the light is injected to a photodetector with responsivity of $\Re$, and then the optical carrier

component beats with the first order component of RF signal, which makes foremost contribution to the final desired electrical RF signal. Finally, the detected current at frequency of ω is given by (detailed derivation given in Appendix A),

$$I_{\omega} = \frac{\Re t_{ff} E_0^{\,2}}{2}\begin{bmatrix} -ar\left(J_1(\sigma\pi)\cos\left(\omega t+\theta+\xi_1\pi-\frac{\pi}{2}\right)+J_1(\sigma\pi)\cos\left(\omega t+\theta+\xi_2\pi-\frac{\pi}{2}\right)\right) \\ +\sqrt{2}r^2 J_0(\sigma\pi)J_1(\sigma\pi)\cos\left(\omega t+\theta+\frac{\pi}{4}\right) \end{bmatrix} \tag{2.3}$$

To obtain the optimum OCSR and maximum RF output power, it is assumed that all high-order harmonics and intermodulation distortions are ignored, then the optical power is given by $P_{oc}+P_{sub}=P_{out}$, where P_{oc} is the optical carrier power, P_{sub} is the optical sideband power and P_{out} is the total output power from the modulator, and alternatively it can be presented as $P_{out}=\left(1+OCSR\right)P_{sub}$. The detected RF power at ω can be given by,

$$P_{RF} \propto P_{oc}\cdot P_{sub} = \left(P_{sub}\right)^2 OCSR = \left(P_{out}\right)^2 \frac{OCSR}{\left(1+OCSR\right)^2} \tag{2.4}$$

It is obvious that P_{RF} depends on the OCSR and maximizes when $OCSR=1$, i.e. $OCSR=0$ dB. It will be verified in simulation and experimental work. In addition, when high MI is used, there must be the high order distortions. However, it is easy to filter them out because they are far from the desired RF signal, so even in high MI cases, and P_{RF} still only depends on the OCSR.

2.3.2 Theoretical Analysis for the Modulator Driven by Two RF Signals

In this section, one optical carrier carries two RF subcarriers case is investigated. Consider two RF signals: $RF_1=\sqrt{2}V_{RF}[\cos(\omega_1 t+\theta_1)]$, and $RF_2=\sqrt{2}V_{RF}[\cos(\omega_2 t+\theta_2)]$ with frequencies of ω_1 and ω_2, arbitrary phase θ_1 and θ_2, and amplitude of V_{RF} driving the modulator. As shown in Appendix B, the output electric field from the modulator is given by,

$$E_{out}(t)=\frac{\sqrt{t_{ff}}}{2}E_0 e^{i\omega_c t}\left\{\begin{array}{l} ae^{i\xi_1\pi}+ae^{i\xi_2\pi} \\ +r\sum_{m=-\infty}^{\infty}\sum_{n=-\infty}^{\infty} i^{m+n}J_m(\sigma\pi)J_n(\sigma\pi)e^{i[m(\omega_1 t+\theta_1+\pi)+n(\omega_2 t+\theta_2+\pi)]} \\ +r\sum_{m=-\infty}^{\infty}\sum_{n=-\infty}^{\infty} i^{m+n}J_m(\sigma\pi)J_n(\sigma\pi)e^{i\left[m(\omega_1 t+\theta_1+\frac{\pi}{2})+n(\omega_2 t+\theta_2+\frac{\pi}{2})-\frac{\pi}{2}\right]} \end{array}\right\} \quad (2.5)$$

where t_{ff} represents the insertion loss of the MZM, a represents the power split ratio of upper branch of the MZM, $r=\sqrt{1-a^2}$ represents the power split ratio of lower branch, $\sigma=\frac{V_{RF}}{V_\pi}$ is defined modulation index, and $\xi_1=\frac{V_{1DC_{op}}}{V_\pi}$ and $\xi_2=\frac{V_{2DC_{op}}}{V_\pi}$ are normalized DC-voltages at $1DC_{op}$ and $2DC_{op}$ ports, respectively.

Note that when *m=0, n=0* in Eq. (2.5), the electric field in Eq. (2.5) is simplified to $E_{\omega_c}=\frac{\sqrt{t_{ff}}}{2}E_0 e^{i\omega_c t}\left[ae^{i\xi_1\pi}+ae^{i\xi_2\pi}+\sqrt{2}rJ_0^{\,2}(\sigma\pi)e^{-i\frac{\pi}{4}}\right]$, i.e. optical carrier. When *m=1, n=0,* the electric field in Eq. (2.5) become 0, i.e. the electric field of the upper sideband fundamental component of RF_1 signal $E_{+\omega_1}=0$. When *m=-1, n=0* the electric field of lower sideband fundamental component of RF_1 signal from Eq. (2.5) is given by

$E_{-\omega_1} = -\sqrt{t_{ff}} E_0 e^{i\omega_c t} r J_0(\sigma\pi) J_1(\sigma\pi) e^{-i(\omega_1 t + \theta_1 - \frac{1}{2}\pi)}$. Similarly, when *m=0, n=1*, it can be obtained that $E_{+\omega_2} = 0$, and when *m=0, n=-1*, $E_{-\omega_2} = -\sqrt{t_{ff}} E_0 e^{i\omega_c t} r J_0(\sigma\pi) J_1(\sigma\pi) e^{-i(\omega_2 t + \theta_2 - \frac{1}{2}\pi)}$ is obtained. The above suggests that a two-tone single sideband modulation is obtained. Contrarily, if the bias voltages at 1DC and 2DC ports are switched, upper sideband is obtained and the lower sideband is eliminated.

Since the coefficients of $E_{-\omega_1}$ and $E_{-\omega_2}$ are totally the same, it is reasonable to define the OCSR of two RF signal by employing one mathematical expression which is given by (detailed derivation given in Appendix B),

$$OCSR = \frac{a^2 + a^2\cos(\xi_1 - \xi_2)\pi + r^2 J_0^4(\sigma\pi) + arJ_0^2(\sigma\pi)\left[\cos\xi_1\pi + \cos\xi_2\pi - \sin\xi_1\pi - \sin\xi_2\pi\right]}{2r^2 J_1^2(\sigma\pi) J_0^2(\sigma\pi)} \quad (2.6a)$$

Then the imperfect situations are considered. It is similar to the case of one RF signal. By defining the splitting (front coupler) coupler's factor as k_{in}, combining (back coupler) coupler's factor as k_{out}, MZM-1 modulator ER as ER_1 and MZM-2 modulator ER as ER_2 the OCSR is given by (detailed derivation given in Appendix B),

$$OCSR = \frac{\left\{\begin{array}{l} c^2 f^2 k^2 + p^2 g^2 h^2 + 2pcfghk \cdot \cos(\xi_1 - \xi_2)\pi \\ +2J_0^2(\sigma\pi)\left[pbg^2h^2 \cdot \cos(\xi_1\pi) + ghbcfk \cdot \cos(\xi_2\pi) - pdfkgh \cdot \sin(\xi_1\pi) - f^2k^2cd \cdot \sin(\xi_2\pi)\right] \\ +(d^2 f^2 k^2 + b^2 g^2 h^2) J_0^4(\sigma\pi) \end{array}\right\}}{\left\{(dfk + bgh)^2 \cdot J_0^2(\sigma\pi) J_1^2(\sigma\pi)\right\}} \quad (2.6b)$$

where $h=\sqrt{k_{in}}$, $k=\sqrt{1-k_{in}}$, $f=\sqrt{k_{out}}$, $g=\sqrt{1-k_{out}}$, $p=\frac{1+\sqrt{ER_1}}{\sqrt{2(ER_1+1)}}$, $b=\sqrt{1-p^2}$,

$c=\frac{1+\sqrt{ER_2}}{\sqrt{2(ER_2+1)}}$, and $d=\sqrt{1-c^2}$. It is obvious that OCSR depends on the coupler's factor and MZMs modulator ER. Moreover, when the parameter h is equal to f for any value, OCSR is independent of the coupler's factor, and only the ER impacts the OCSR.

In order to obtain the current of RF signal after the photodetection, it is assumed that the light is injected to a photodetector with responsivity of $\Re$, and the optical carrier component beats with the first order component of RF signal, which makes foremost contribution to the final desired electrical RF signal. Finally, assuming no noise contributions, the detected currents at frequency of ω_1 and ω_2 are given by (detailed derivation given in Appendix B),

$$I_{\omega_1}=\frac{\Re t_{ff}E_0^{\,2}}{2}\begin{bmatrix}-arJ_0(\sigma\pi)J_1(\sigma\pi)\cos(\omega_1 t+\theta_1+\xi_1\pi-\frac{\pi}{2})\\-arJ_0(\sigma\pi)J_1(\sigma\pi)\cos(\omega_1 t+\theta_1+\xi_2\pi-\frac{\pi}{2})\\+\sqrt{2}r^2J_0^{\,3}(\sigma\pi)J_1(\sigma\pi)\cos(\omega_1 t+\theta_1+\frac{\pi}{4})\end{bmatrix} \tag{2.7a}$$

and

$$I_{\omega_2}=\frac{\Re t_{ff}E_0^{\,2}}{2}\begin{bmatrix}-arJ_0(\sigma\pi)J_1(\sigma\pi)\cos(\omega_2 t+\theta_2+\xi_1\pi-\frac{\pi}{2})\\-arJ_0(\sigma\pi)J_1(\sigma\pi)\cos(\omega_2 t+\theta_2+\xi_2\pi-\frac{\pi}{2})\\+\sqrt{2}r^2J_0^{\,3}(\sigma\pi)J_1(\sigma\pi)\cos(\omega_2 t+\theta_2+\frac{\pi}{4})\end{bmatrix} \tag{2.7b}$$

However, when two RF signals drive the MZM, IMD will be induced inevitably due to nonlinearity of the MZM response. Assume that lower sideband is used for OSSB. To obtain the RF signal at frequency ω_1 by photodetection, the beats include the light at $-\omega_1$ beating with optical carrier, the light at $-\omega_2$ beating with the light at $-\omega_2+\omega_1$, and the light at $-2\omega_1+\omega_2$ beating with the light at $-\omega_1+\omega_2$, which are shown in Fig. 2.2. Unfortunately, the light at $-\omega_2$ beating with the light at $-\omega_2+\omega_1$, and the light at $-2\omega_1+\omega_2$ beating with the light at $-\omega_1+\omega_2$ are considered as noise, which overlap the RF signal and difficult to be filtered out. For the RF signal at frequency ω_2, it is similar. By summing the currents due to the light at $-\omega_2$ beating with the light at $-\omega_2+\omega_1$, and the light at $-2\omega_1+\omega_2$ beating with the light at $-\omega_1+\omega_2$ together, the noise current at frequency ω_1 is given by (detailed derivation given in Appendix B)

$$I_{IMD\omega_1}=\frac{\Re t_{ff}E_0^{\,2}}{2}\cos(\omega_1 t+\theta_1+\frac{\pi}{4})\left[-\sqrt{2}r^2J_1^{\,3}(\sigma\pi)J_0(\sigma\pi)+\sqrt{2}r^2J_1^{\,3}(\sigma\pi)J_2(\sigma\pi)\right] \tag{2.8a}$$

Similarly, the noise current at frequency ω_2 is given by

$$I_{IMD\omega_2}=\frac{\Re t_{ff}E_0^{\,2}}{2}\cos(\omega_2 t+\theta_2+\frac{\pi}{4})\left[-\sqrt{2}r^2J_1^{\,3}(\sigma\pi)J_0(\sigma\pi)+\sqrt{2}r^2J_1^{\,3}(\sigma\pi)J_2(\sigma\pi)\right] \tag{2.8b}$$

Based on Eq. (2.7) and Eq. (2.8), the effect of the nonlinear distortion IMD_{ω_1} is presented by the ratio $P_{RF_1\_ideal}/P_{IMD_{\omega_1}}=\dfrac{|I_{\omega_1}|^2}{|I_{IMD_{\omega_1}}|^2}$. Similarly, $P_{RF_2\_ideal}/P_{IMD_{\omega_2}}=\dfrac{|I_{\omega_2}|^2}{|I_{IMD_{\omega_2}}|^2}$ is also obtained. Because the expression of I_{ω_1} (Eq. 2.7a) is an equation of $\mathrm{MI}(\sigma)$, ξ_1 and

ξ_2 while $I_{IMD_{\omega_1}}$ is an equation of MI(σ). After analysis, it is noted that $P_{RF_1\_ideal} / P_{IMD_{\omega_1}}$ is equal to $P_{RF_2\_ideal} / P_{IMD_{\omega_2}}$, and both of them depend on the MI(σ) and OCSR which is determined by ξ_1 and ξ_2. For example, when MI=0.1 and OCSR=3 dB (optimum OCSR), the ratio of $P_{RF_1\_ideal} / P_{IMD_{\omega_1}}$ is 24 dB, whereas it is 28 dB when MI=0.1 and OCSR=10 dB. Also noted is when MI=0.5 and OCSR=3 dB, the ratio of $P_{RF_1\_ideal} / P_{IMD_{\omega_1}}$ is only 10 dB which indicates that ratio of $P_{RF_1\_ideal} / P_{IMD_{\omega_1}}$ is depending on the MI and OCSR. Meanwhile, $P_{IMD_{\omega_1}}$ can't be ignored when this considered modulation technique works with high MI. The same results are obtained when upper sideband is used.

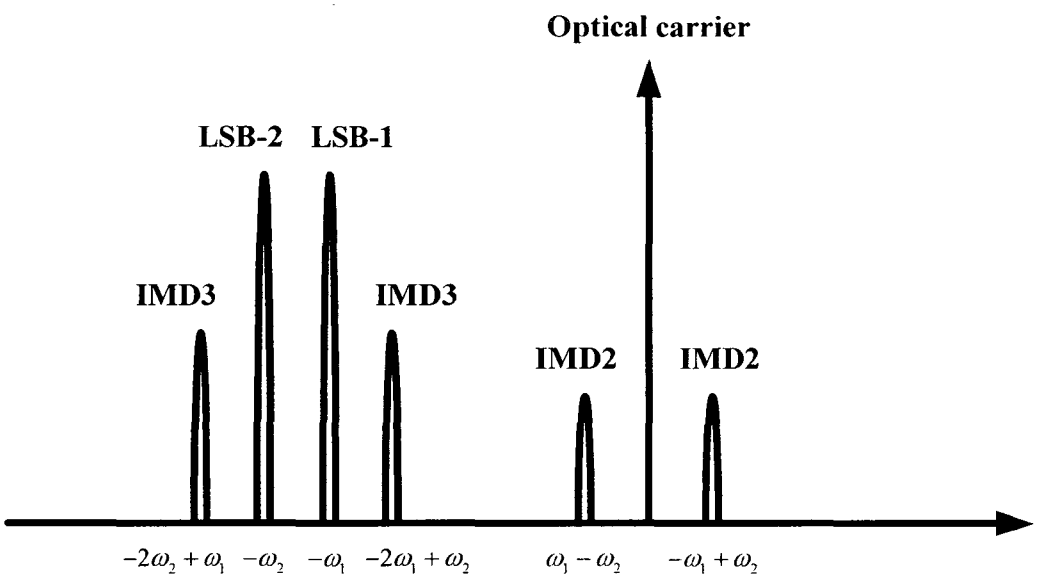

Figure 2.2 Optical spectra at the output of the modulator for two RF signals at ω_1 and ω_2. LSB: lower sideband, IMD3: third order intermodulation distortion, and IMD2: second order intermodulation distortion.

According to Fig. 2.2 it is also noted that two terms of IMDs at frequencies $(-2\omega_1+\omega_2)$ and $(-2\omega_2+\omega_1)$, i.e. IMD3 are most possibly close to the two RF subcarriers and hard to be suppressed or filtered out. As mentioned in Chapter 1, IMD3 will lead to the degradation of system performance heavily. Thus the theoretical analyses of IMD3 are required. For the IMD3 at frequency $-2\omega_1+\omega_2$, it includes the light at $-2\omega_1+\omega_2$ beating with optical carrier and the light at $-\omega_1$ beating with the light at $\omega_1-\omega_2$. The current is obtained by (detailed derivation given in Appendix B),

$$I_{-2\omega_1+\omega_2}=\frac{\Re t_{ff}E_0^{\,2}}{2}\left[\begin{array}{l} arJ_1(\sigma\pi)J_2(\sigma\pi)\cos(2\omega_1t-\omega_2t+2\theta_1-\theta_2+\xi_1\pi-\frac{\pi}{2}) \\ +arJ_1(\sigma\pi)J_2(\sigma\pi)\cos(2\omega_1t-\omega_2t+2\theta_1-\theta_2+\xi_2\pi-\frac{\pi}{2}) \\ -\sqrt{2}r^2J_1^{\,3}(\sigma\pi)J_0(\sigma\pi)\cos(2\omega_1t-\omega_2t+2\theta_1-\theta_2+\frac{\pi}{4}) \\ -\sqrt{2}r^2J_0^{\,2}(\sigma\pi)J_1(\sigma\pi)J_2(\sigma\pi)\cos(2\omega_1t-\omega_2t+2\theta_1-\theta_2+\frac{\pi}{4}) \end{array}\right] \tag{2.9a}$$

and using the same method, the IMD3 at frequency $-2\omega_2+\omega_1$ is given by,

$$I_{-2\omega_2+\omega_1}=\frac{\Re t_{ff}E_0^{\,2}}{2}\left[\begin{array}{l} arJ_1(\sigma\pi)J_2(\sigma\pi)\cos(2\omega_2t-\omega_1t+2\theta_2-\theta_1+\xi_1\pi-\frac{\pi}{2}) \\ +arJ_1(\sigma\pi)J_2(\sigma\pi)\cos(2\omega_2t-\omega_1t+2\theta_2-\theta_1+\xi_2\pi-\frac{\pi}{2}) \\ -\sqrt{2}r^2J_1^{\,3}(\sigma\pi)J_0(\sigma\pi)\cos(2\omega_2t-\omega_1t+2\theta_2-\theta_1+\frac{\pi}{4}) \\ -\sqrt{2}r^2J_0^{\,2}(\sigma\pi)J_1(\sigma\pi)J_2(\sigma\pi)\cos(2\omega_2t-\omega_1t+2\theta_2-\theta_1+\frac{\pi}{4}) \end{array}\right] \tag{2.9b}$$

According to Eq. (2.7a), Eq. (2.7b), Eq. (2.9a) and Eq. (2.9b), the ratio $P_{RF_1\_ideal}/P_{IMD3}=\dfrac{|I_{\omega_1}|^2}{|I_{-2\omega_1+\omega_2}|^2+|I_{-2\omega_2+\omega_1}|^2}=\dfrac{|I_{\omega_2}|^2}{|I_{-2\omega_1+\omega_2}|^2+|I_{-2\omega_2+\omega_1}|^2}=\dfrac{|I_{\omega_1}|^2}{2|I_{-2\omega_1+\omega_2}|^2}$ is obtained,

where assume $\left|I_{-2\omega_1+\omega_2}\right|^2 = \left|I_{-2\omega_2+\omega_1}\right|^2$. Similar to the ratio $P_{RF_1\_ideal} / P_{IMD_{\omega_1}}$, it is found that $P_{RF_1\_ideal} / P_{IMD3}$ also depends on the MI and OCSR. For example, when OCSR=3 dB and MI= 0.1, the ratio is 22 dB and when OCSR=3 dB and MI=0.5, the ratio is 9 dB which indicates the IMD3 will be sufficiently large and can't be neglected when high MIs are used. The above suggests that this considered technique better works with low MI.

To represent the impairment of the total IMDs to this considered technique, the ratio $P_{RF_1\_ideal} / P_{IMD_{total}}$ is given by

$$P_{RF_1\_ideal} / P_{IMD_{total}} = P_{RF_1\_ideal} / (P_{IMD_{-2\omega_1+\omega_2}} + P_{IMD_{\omega_1}} + P_{IMD_{-2\omega_2+\omega_1}} + P_{IMD_{\omega_2}}) = \frac{\left|I_{\omega_1}\right|^2}{2\left\{\left|I_{-2\omega_1+\omega_2}\right|^2 + \left|I_{IMD_{\omega_1}}\right|^2\right\}}$$

for the RF signal at frequency ω_1, where assume $\left|I_{-2\omega_1+\omega_2}\right|^2 = \left|I_{-2\omega_2+\omega_1}\right|^2$ and $\left|I_{IMD_{\omega_1}}\right|^2 = \left|I_{IMD_{\omega_2}}\right|^2$. Here only IMD_{ω_1} and $IMD3$ are considered because they are hard to be filtered out and mostly impact the system performance. Due to the totally same coefficient, ratio $P_{RF_2\_ideal} / P_{IMD_{total}}$ is equal to $P_{RF_1\_ideal} / P_{IMD_{total}}$. Furthermore, both of them depend on MI and OCSR, high MI will introduce large $P_{IMD_{total}}$. The simulation results will be shown in Chapter 3.

Now the optimum OCSR and maximum RF output power are considered. Suppose that no noise contributions, then the optical output power of MZMs are given by $P_{out} = P_{sub1} + P_{sub2} + P_{oc} = 2P_{sub} + P_{oc}$, where P_{out} is the total output power from the modulator, P_{sub1} and P_{sub2} are optical power of two sidebands and assumed the same i.e.

P_{sub}. So the RF output power at ω_1 and ω_2 is given by $P_{RF} \propto (P_{out})^2 \frac{OCSR}{(2+OCSR)^2}$. It is easily verified that P_{RF} is maximized when $OCSR$=2 or 3 dB, which suggests that the optical carrier power should be 3 dB higher than that of the optical sidebands to obtain the maximum RF power for an optical carrier carrying two optical sidebands. Similarly the optical carrier power should be 6 dB higher than that of optical sidebands for an optical carrier carrying four sidebands, and so on. However, when high MI like 0.5 is applied, the power of IMDs like IMD_{ω_1} and $IMD3$ will be fairly large and difficult to be filtered out. Meanwhile, since the total output power from the modulator P_{out} is fixed, it is reasonable to get a new expression $P_{out} = 2P_{sub} + P_{oc} + P_{IMDs}$. Obviously the RF output power $P_{RF} \propto P_{oc} \cdot P_{sub}$ will decrease, and the optimum OCSR will not be 3 dB anymore. Also compared to the one RF signal applied case, it is found that RF output power is not only depending on the OCSR, but also the MI for two RF signals applied case.

2.4 Summary

In this chapter, the considered modulation technique is theoretically analyzed and the details of OSSB realization are well showed. Moreover, the equations of OCSR for ideal and imperfect situations are given out. By calculating, it is noted that the OCSR can be highly suppressed which means the efficiency of modulation is considerably improved. Furthermore, it has been found that optimum OCSR is 0 dB when one RF signal applied. However, the optimum OCSR changes to 3 dB when two RF signals applied, and 6 dB when four RF signals applied, etc. Also noted is that when two RF signals and high MI like more than 0.5 are applied, the IMDs will be considerably large, and the RF output

power will decrease evidently, which means the RF output power not only depends on OCSR, but also the MI. Contrast to two RF signals applied case, if only one RF signal is modulated, RF output power will entirely depend on OCSR. It is suggested that this modulation technique is more suitable for low MI when multiple RF signals are employed.

Chapter 3

Analysis by Simulation and Comparison with Theory

3.1 Introduction

As previously stated in Chapter 2, by theoretical analysis, it is noted that the variable OCSR can be highly suppressed which means the efficiency of modulation is considerably improved. Furthermore, the optimum OCSR, maximum RF output power and impairments of modulation distortions are analyzed. In this chapter, the conclusions of theoretical analysis in Chapter 2 will be verified by computer simulations. By comparing the simulation with theoretical results, analyses and explanation are given out. All the simulations are based on the platform of VPI TransmissionMaker 7.0, a commercial software package.

The following chapter will be organized as follows, Section 3.2 will show the simulation results when only one RF signal applied. In this section, how to choose DC bias to obtain optimum OCSR, impact of bias shift and the method to compensate, mismatch of the coupler's factors, mismatch of the MZMs ER, and phase imbalance of the two parallel MZMs are showed. Section 3.3 will show the simulation results when two RF signals are applied. Analysis and explanation are also given out. Section 3.4 will draw some conclusions.

3.2 Considered Modulator Driven by One RF Signal

Table 3.1 indicates the parameters used in VPI model. Here it is needed to emphasize that this technique uses fixed output power of modulators: when one RF signal case, the output power is fixed to -5 dBm and when 2 RF signals case, the output power is fixed to -1 dBm. The reason is the optical power of incident optical signal on PD can never be larger than 0 dBm, which is the saturation value of PD.

Table 3.1 VPI simulation model parameters

CW laser parameters	
Emission frequency (Hz)	193.1×10^{12}
Average power (mw)	1
Line width (MHz)	10
Initial phase (°)	0
DE-MZM parameters	
$V_{\pi DC}$ (V)	5
$V_{\pi RF}$ (V)	5
Insertion loss (dB)	6
Extinction ratio (dB)	15
LowerArmPhaseSense	Negative
PD parameters	
Responsivity (A/W)	1
Dark current (A)	0.0
Thermal noise ($A/\sqrt{Hz}$)	10.0×10^{-12}
Shot noise	On
Responsivity (A/W)	1
Optical Filter parameters	
Filter Type	BandPass

Transfer Function	Gaussian
Center Frequency (Hz)	193.1×10^{12}
Gaussian Order	3
Bandwidth when one RF signal (GHz)	15
Bandwidth when two RF signals (GHz)	18
Electrical Filter parameters	
Filter Type	BandPass
Transfer Function	Bessel
Center Frequency (Hz)	5×10^{9}
Filter Order	4
Bandwidth when one and two RF signals (MHz)	2
EDFA fixed output power	
when one RF signal (mw)	0.316228
when two RF signals (mw)	0.794328

3.2.1 Optical Single Sideband Modulation with Adjustable Optical Carrier-to-Sideband Ratio

To verify the modulator that not only OSSB modulation but also tunability of OCSR can be obtained simultaneously, the simulation model is presented by VPI-TransmissionMaker software. In the simulation, it is assumed that a laser has a wavelength of 1553.6 nm, linewidth of 10 MHz and power of 1 mW. Each phase modulator has π-phase shifted voltage of 5 V, insertion loss of 6 dB and Y-junction has extinction ratio of 15 dB. Assumed that RF signal has a voltage of 0.25 V (V_{RF}) which corresponds to a modulation index of MI(σ)=0.05 and a frequency of 5 GHz. The bias V_{1DC} and V_{2DC} are set to 0 and $V_{\pi}/2$, respectively. Simulated optical spectra are shown

in Fig. 3.1. where $V_{2DC_{op}}$ is set to 5.3V and $V_{1DC_{op}}$ is set to 0, 2.1 and 3.5 V, respectively. It is seen that OSSB modulation is always obtained. It is clearly observed that OCSR is varied by change of bias voltage. This confirms that OSSB modulation and tunability of OCSR are obtained simultaneously.

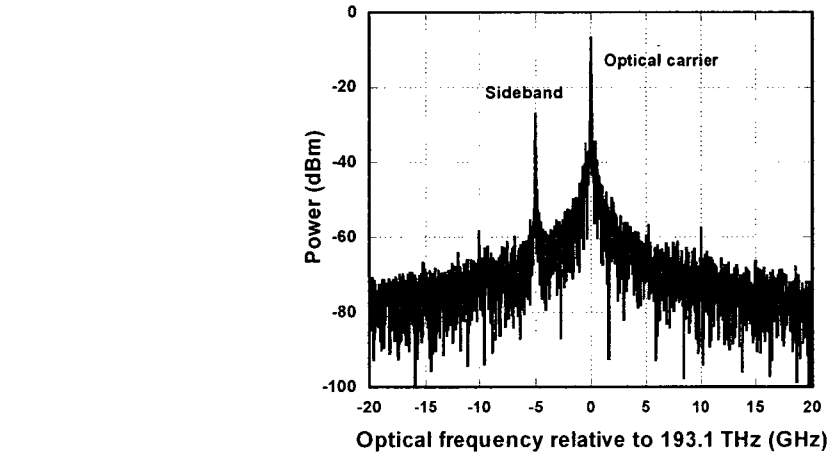

(a)

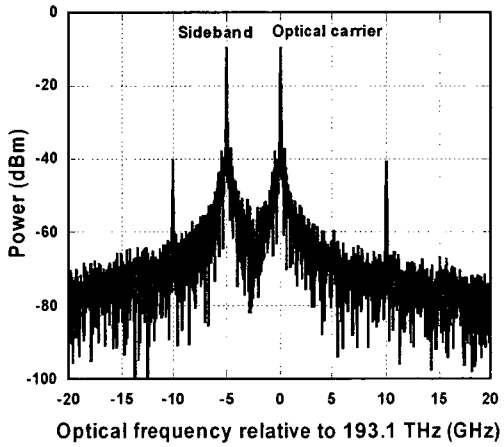

(b)

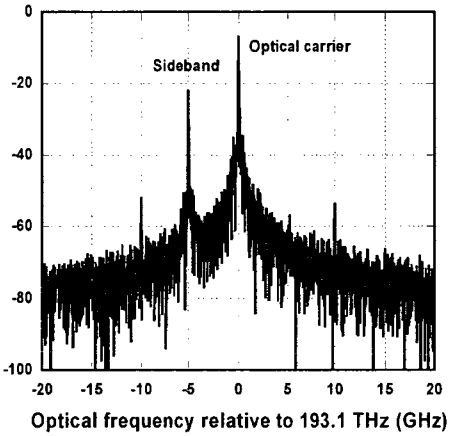

(c)

Figure 3.1 Simulated optical spectra using the modulator with $V_{2DC_{op}}$=5.3 V and (a) $V_{1DC_{op}}$=0, (b) $V_{1DC_{op}}$=2.1, and (c) $V_{1DC_{op}}$=3.5 V.

Note that when both $V_{1DC_{op}}$=0 and $V_{2DC_{op}}$=0, the modulator is equivalent to a single MZM for OSSB modulation.

Moreover, from Fig. 3.1 it is found that when the bias value is varying, not only the OCSR will change, but also the high order distortion will change. For example, second order distortion at frequency of 10 and -10 GHz relative to 193.1 GHz will change when different $V_{1DC_{op}}$ is used. Therefore, an optical filter is needed to eliminate the high order distortions. Because the high order distortions are far from the desired RF signal, they are easily to filter out.

How to choose the $V_{1DC_{op}}$ and $V_{2DC_{op}}$ to obtain the optimum OCSR which is 0dB? For given MI(σ), the normalized biased voltages ξ_1 ($V_{1DC_{op}}$) and ξ_2 ($V_{2DC_{op}}$) to obtain OCSR of 0 dB can be computed by solving Eq. (2.2)=0 and the results are shown in Fig 3.2. Note that ξ_1 and ξ_2 can be interchanged in Eq. (2.2). It is seen that when MI(σ) is small, the choices of bias voltage ξ_1 and ξ_2 are limited to a small range to obtain OCSR=0 dB. With the increase of MI(σ), more choices of bias voltage ξ_1 and ξ_2 can be used for obtaining OCSR=0 dB.

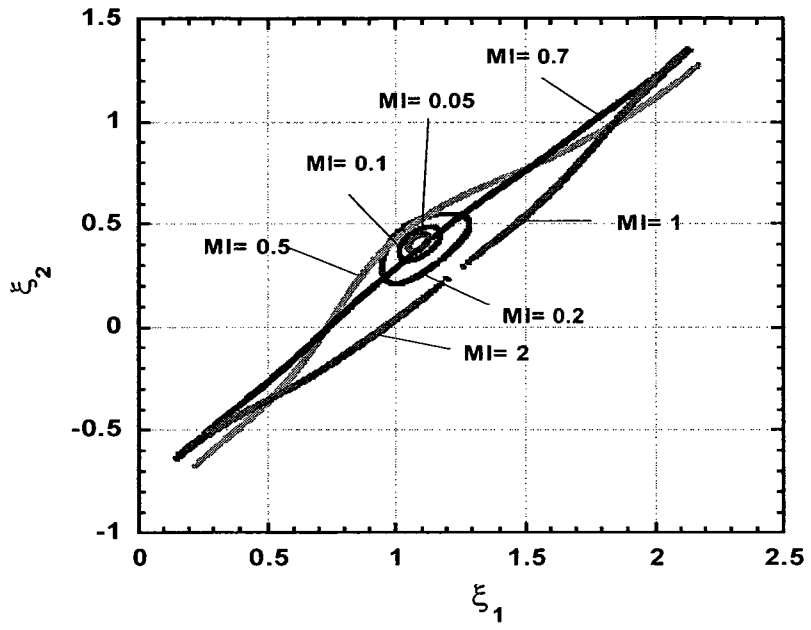

Figure 3.2 Normalized bias voltages ξ_1 and ξ_2 required for OCSR = 0 dB

Now consider the tunability of OCSR. We set V_{1DC}=0, V_{2DC}=2.5 V that is equal to $\pi/2$ phase-shifted voltage, and $V_{2DC_{op}}$ = 5.3 V. Assume RF frequency of f=5 GHz and the amplitude of RF signal V_{RF} at 0.25, 0.5, 1, 2.5, 3.5, 5, 7.5 and 10 V, i.e. MI(σ)=0.05, 0.1, 0.2, 0.5, 0.7, 1, 1.5 and 2. Fig. 3.3 shows calculated OCSR versus $V_{1DC_{op}}$ for the above MIs. It is seen that OCSR can be changed from 23 to ~-23 dB by varying the bias voltage of $1DC_{op}$ port, depending on modulation index. It is clearly observed that the optimum OCSR of 0 dB is always obtained by varying the bias voltage. Calculated OCSR and simulation results are well matched in Fig. 3.3.

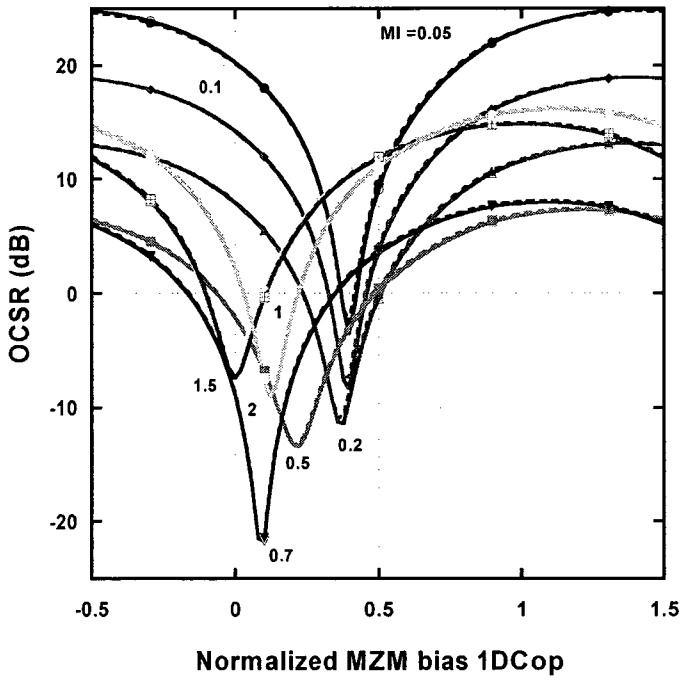

Figure 3.3 Calculated OCSR (dash) and Simulation OCSR (solid) with normalized bias voltage at $1DC_{op}$ port.

However, when MI is high, the high order distortion will increase definitely. Because this technique uses fixed output power, therefore it is better working in low modulation index. In addition, high order distortion can be cut off by the optical filter.

Fig. 3.4 shows calculated RF power (dash) and simulation result (solid) versus OCSR for MI= 0.05, 0.1, 0.2, and 0.5. In calculation the effect of high-order nonlinear distortion for the high MI is ignored. As shown in Fig. 3.4, the RF power is the same for any MI, and the maximum RF power is obtained when OCSR=0 dB, which is the same as predicted by theoretical analysis. Note that for this modulator the RF power is independent of modulation index, as shown by Eq. (2.4).

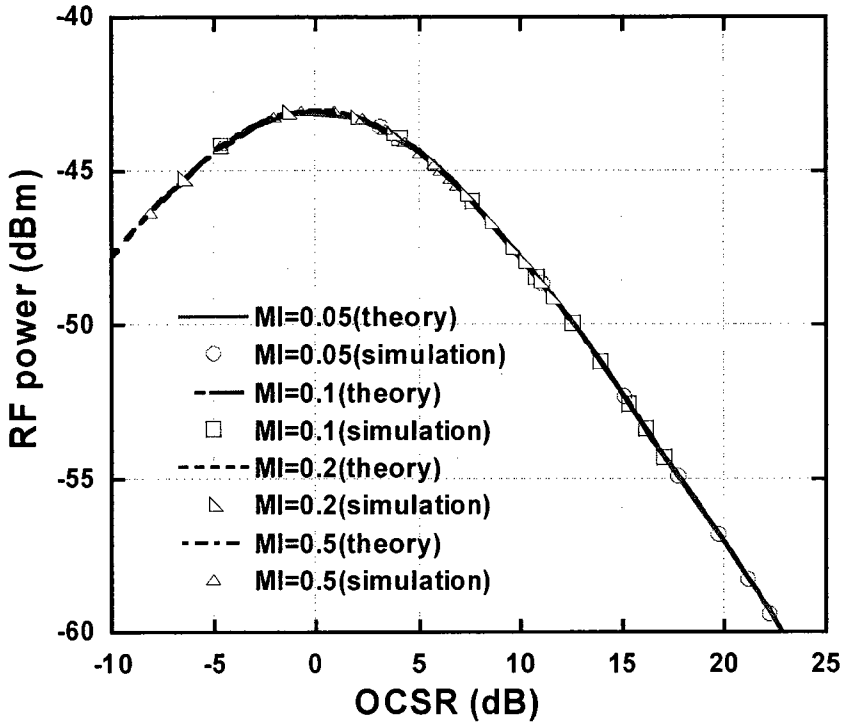

Figure 3.4 Impact of OCSR on RF power

3.2.2 Impact of Bias Drift

Because this technique heavily relies on the value of the bias voltage on the two parallel MZM modulators, therefore it is necessary to find out how sensitive of the bias drift. Bias drift due to wavelength dependence can be solved using wavelength insensitive bias technique [26], where thermal drift can be reduced to less than 0.1deg/°C at 90° (quadrature bias) [27]. Therefore, the performance degradation due to thermal bias drift is investigated in this work. In the simulation, assumed that a thermal bias drift of 0.1deg/°C at quadrature bias, which corresponds to 0.02778 V/ °C for V_π = 5V, and MI=0.1 are applied. We set the biases for OSSB and maximum RF power (OCSR = 0 dB) at the reference temperature of 25 °C, and vary the operating temperature T_a from 0 to 70°C.

The OCSR and RF power degradation due to temperature change are shown in Fig. 3.5(a). Furthermore, the optical power ratio of the desired sideband to undesired sideband (S/U-R) is used to measure the efficiency of OSSB modulation. For example, if the desired sideband is the upper sideband, the undesired sideband is the lower sideband, and vice versa. Fig. 3.5(b) shows the S/U-R versus temperature change. It is seen that with the change of temperature, the ratio decreases significantly. This means that the optical modulation becomes ODSB, but not OSSB anymore. This suggests that the bias voltage control has to be used to compensate for thermal bias drift given by $0.02778(T_a - 25)$.

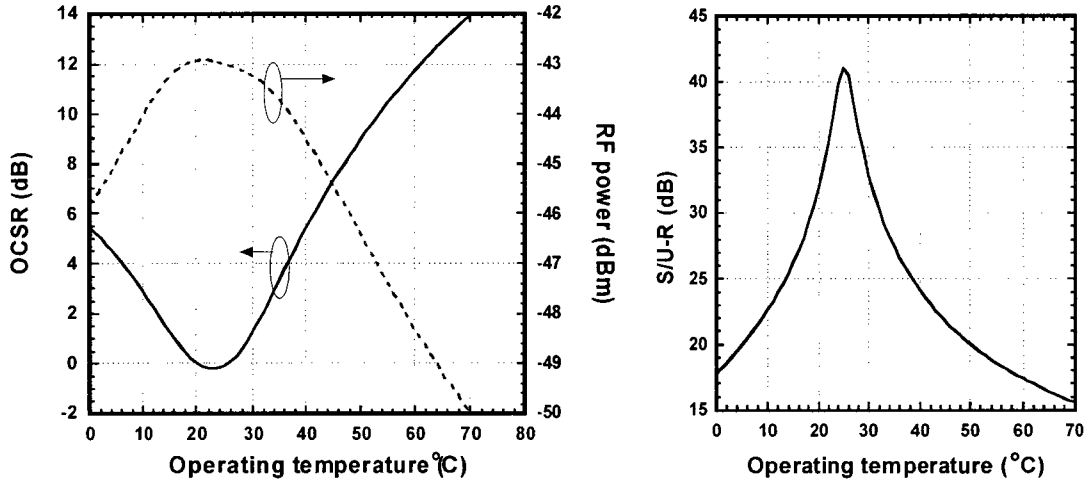

(a) (b)

Figure 3.5 (a) OCSR and RF power versus operating temperature, and (b) corresponding sideband to undesired sideband optical power ratio versus operating temperature.

By adjusting DC biases due to the thermally shifted switching voltage, i.e. $V_{\pi,new} = V_{\pi,25°C} + 0.02778(T_a - 25)$, it still can obtain OSSB modulation and OCSR tunability. Consider an RF tone voltage of V_{RF}=0.5 V. Fig. 3.6(a) shows the change of

OCSR tunability and RF power versus temperature after using bias control (i.e. adjusting two biases ξ_1 and ξ_2 corresponding to the new V_π). When the operating temperature is changed, the modulation index will change due to the V_π change. Thus OCSR is changed. It is seen that OCSR is varied from -1 to 1.5 dB over the range of 0 ~ 70°C even using the bias control. But it is clear that RF power varies by less than 0.1 dB. Also, OSSB can still be obtained as shown from Fig. 3.6(b) where the undesired sideband is suppressed by more than 39 dB over the operating temperature range of 0~70 °C with respect to the desired sideband.

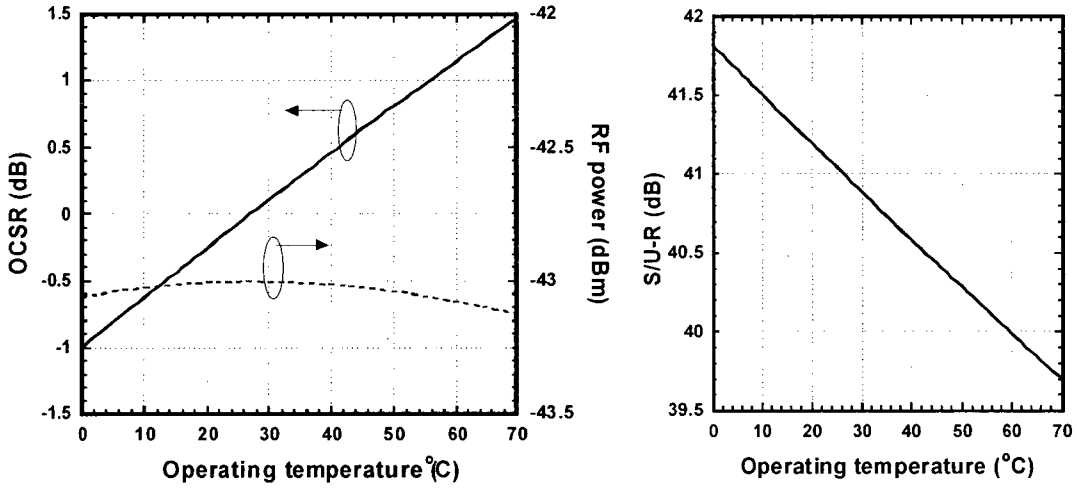

(a) (b)

Figure 3.6 (a) OCSR and RF power versus operating temperature, and (b) corresponding sideband to undesired sideband optical power ratio versus operating temperature after using bias control.

3.2.3 Mismatch between Splitting and Combining Ratios

Due to imperfections in manufacturing process, it is difficult to get 50/50 optical splitting k_{in} and combining k_{out} ratio at the input and output of the device. In order to evaluate the sensitivity of the performance to k_{in} and k_{out}, we set $\xi_2 = 1.06$ and tune ξ_1 to maximize RF power for different mismatch Δk between k_{in} and k_{out}. Assume that $k_{in} = 0.5(1-\Delta k)$ and $k_{out} = 0.5(1+\Delta k)$, where Δk is varied from -0.2 to 0.2. Fig. 3.7(a) shows the maximum RF power versus Δk and corresponding OCSR versus Δk. It is clear that RF power and OCSR are sensitive to mismatch between k_{in} and k_{out}, however the RF power varies by less than 0.5 dBm while OCSR changes by 3.5 dB for a mismatch of less than 0.1 which can be achieved practically. Fig. 3.7(b) shows the normalized bias voltage ξ_1 to achieve maximum RF power versus the mismatch Δk.

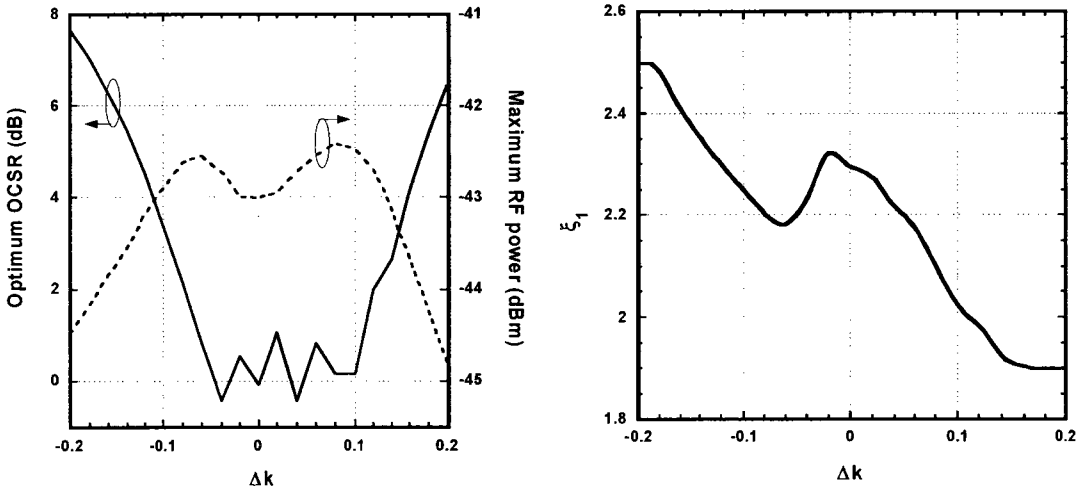

(a) (b)

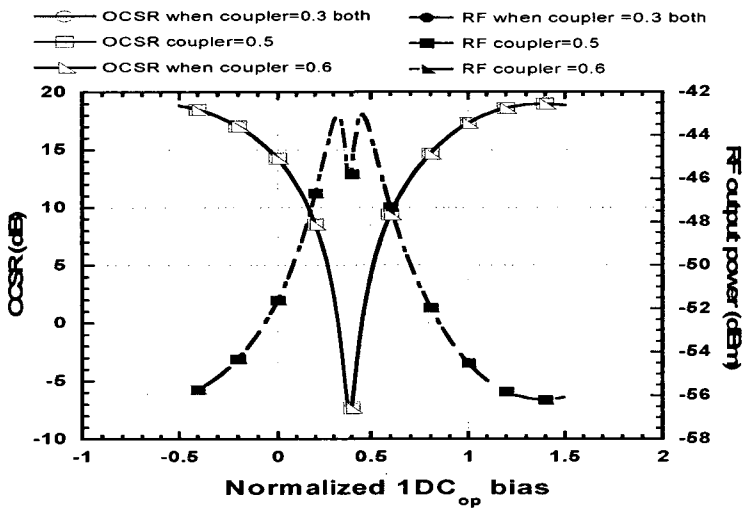

(c)

Figure 3.7 (a) Optimum OCSR and maximum RF power versus mismatch Δk, (b) corresponding ξ_1 versus mismatch Δk between splitting and combining ratio. ξ_2 = 1.06 and MI = 0.1 are used, and (c) when $k_{in} = k_{out}$ =0.3, 0.5 and 0.6 the OCSR and RF power versus Normalized 1DC$_{op}$.

Now consider another situation. If the splitting and combining ratios are the same and are set to be $k_{in} = k_{out}$ =0.3, 0.5 and 0.6, then it is noted that the coupler ratios do not impact the system performance because of the exactly the same curves in Fig. 3.7(c).

3.2.4 Mismatch between MZMs Extinction Ratios

Practically, it is difficult to match ER of the top and bottom MZMs, then investigating the impact of ER mismatch *ΔER* between the two integrated MZMs is needed. Here MI= 0.1 is used, and we set ξ_2 = 1.06 and tune ξ_1 to obtain maximum RF power for each mismatch *ΔER*. Fig. 3.8(a) shows the variation of OCSR and RF power versus *ΔER* when the ER of the top MZM is fixed to 15 dB, i.e. ER$_1$=15 dB. It is clear that RF power varies by less

than 1 dBm while OCSR changes by 1dB for an ER mismatch of less than 4 dB which can be achieved practically. Similar results are obtained when the ER of the bottom MZM is fixed to 15 dB, i.e. ER_2=15 dB. Corresponding to Fig. 3.8(a), Fig. 3.8(b) shows the related normalized bias ξ_1 to achieve the maximum RF power. It is seen that due to this mismatch, the bias ξ_1 has to be significantly changed in order to optimize the performance.

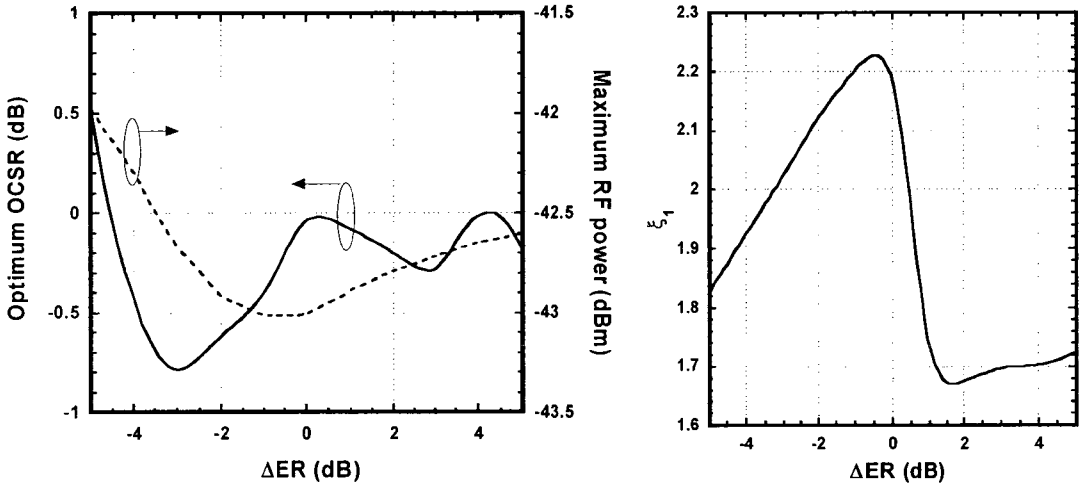

(a) (b)

Figure 3.8 (a) Optimum OCSR and maximum RF power versus ER mismatch, and (b) corresponding normalized bias ξ_1 versus ER mismatch. Top MZM has a fixed ER of 15 dB, ξ_2 = 1.06 and MI = 0.1 are used.

3.2.5 Phase Imbalance between Branch-A and Branch-B.

Now consider the impact of phase imbalance between branch-A and branch-B. It is simply to insert an optical phase modulator in branch-A after MZM-1 which will alter the phase imbalance. As an example, when MI= 0.1 is used, we set the DC biases for OSSB

and maximum RF power (ξ_1 = 0.454, ξ_2 = 1.06, and V_{2DC} = 2.5 V), and vary the phase imbalance from -180° to 180°.

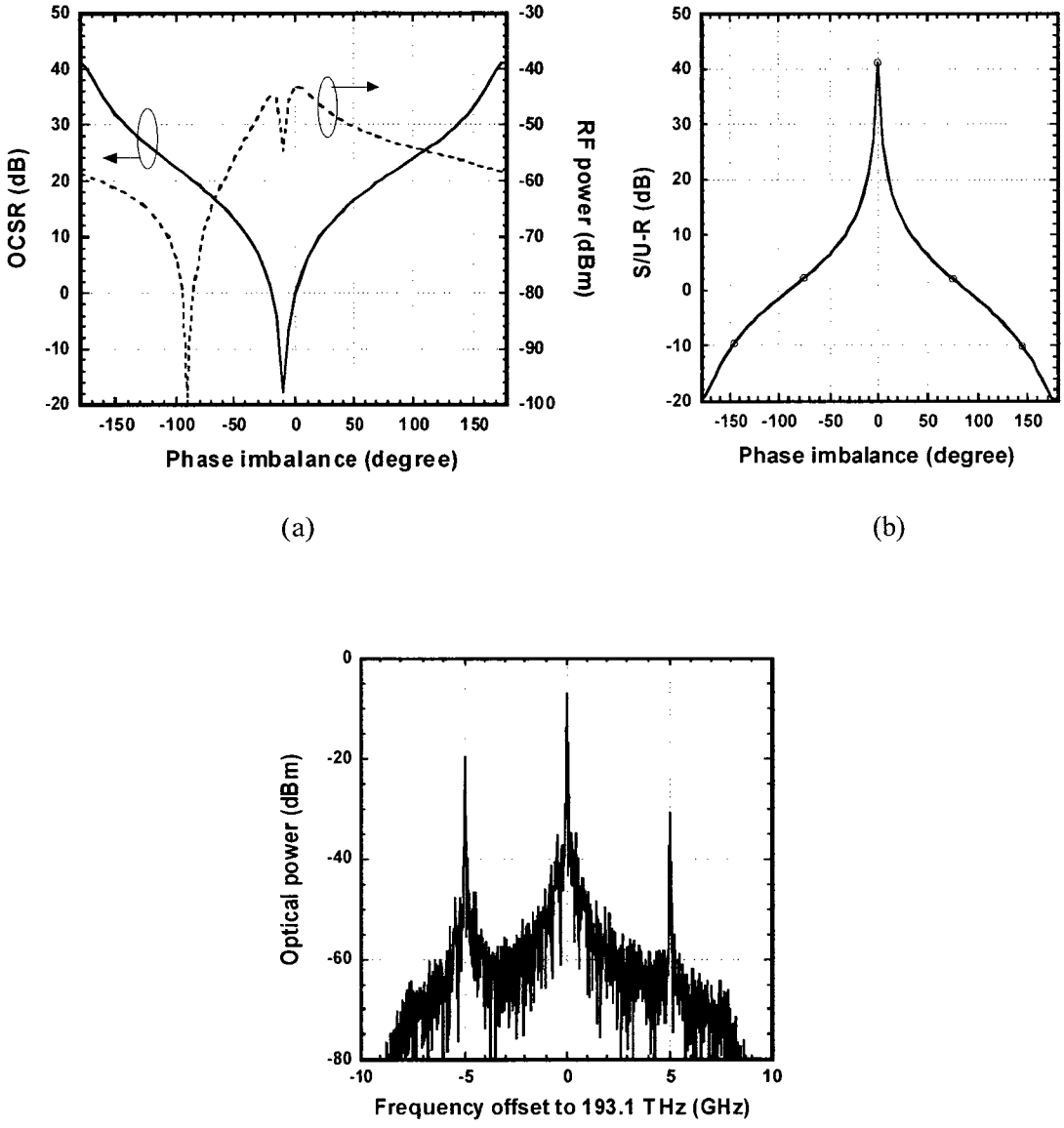

Figure 3.9 (a) OCSR and RF power versus phase imbalance, (b) corresponding S/U-R versus phase imbalance, and (c) optical spectrum for 30^0 phase imbalance. We choose MI=0.1.

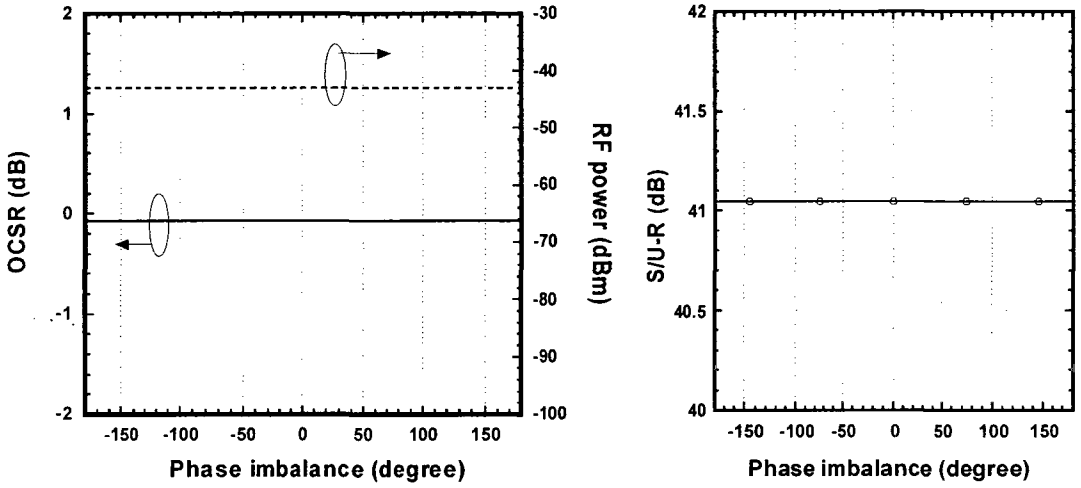

(a) (b)

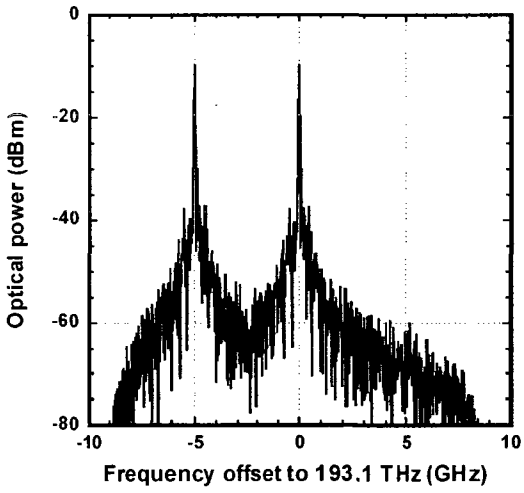

(c)

Figure 3.10 (a) OCSR and RF power versus phase imbalance, (b) corresponding S/U-R versus phase imbalance, and (c) optical spectrum for 30^0 phase imbalance after tuning the bias V_{1DC} and $V_{1DC_{0^0}}$ to compensate for phase imbalance. We choose MI=0.1.

Fig. 3.9(a) depicts simulated OCSR and corresponding RF power versus phase imbalance. It is clear that for high phase imbalance, OCSR increases and RF power decreases. This is because OSSB no longer exists as predicted by the low S/U-R shown in

Fig. 3.9(b) and confirmed by the optical spectrum for 30^{o} phase imbalance shown in Fig. 3.9(c). For high phase imbalance, it is difficult to get OSSB and OCSR tunability simultaneously. Fortunately, the biases can be tuned to compensate for this phase imbalance. For example, if the phase imbalance between branches A and B is $\Delta\varphi$ then it can be compensated by subtracting the voltage $V_{\pi}\,\Delta\varphi/180^{0}$ from the biases $V_{1DC_{op}}$ and V_{1DC}. Corresponding to Fig. 3.9, Fig. 3.10(a) shows OCSR and RF power versus phase imbalance after tuning $V_{1DC_{op}}$ and V_{1DC}. It is observed that OCSR of ~0 dB and maximum RF power are achieved for any phase imbalance. Also OSSB modulation is obtained as shown in Fig. 3.10(b), where S/U-R is maintained to 40 dB. As an example, optical spectrum at phase imbalance of 30^{0} is shown in Fig. 3.10(c) where phase imbalance compensation by tuning biases of $V_{1DC_{op}}$ and V_{1DC} is used. It is seen that an OSSB modulation is still obtained in contrary to Fig. 3.9(c). Similar results can be obtained for other modulation indexes like 0.05, 0.2, 0.5, 1 and 2 (higher RF modulation index).

3.3 Considered Modulator Driven by Two RF Signals

In the previous section, how to optimize the OCSR and how OCSR impacts the performance of system when only one RF signal applied is investigated. Now for the case of two RF signals, it is important to observe whether this modulation technique is still effective to improve the performance of system, and whether the optimum OCSR is 3 dB. Moreover, because high order distortions are easily to be filtered out, thus only the IMD_{ω_1} and $IMD3$ are discussed in detail.

3.3.1 Optical Single Sideband Modulation with Adjustable Optical Carrier-to-Sideband Ratio

It is the same as one RF signal case that the simulation model is still presented by VPI-TransmissionMaker software. In this simulation, assumed that the frequencies of RF signals are 5 GHz and 6 GHz; a laser has a wavelength of 1553.6 nm, linewidth of 10 MHz and power of 1 mW. Each phase modulator has π-phase shifted voltage of 5 V, insertion loss of 6 dB and Y-junction has extinction ratio of 15 dB. The RF signal at frequency of 5 GHz is chosen to simulate and analyze, and the same result can be obtained for the RF signal at frequency of 6 GHz. Suppose that the RF signal has a voltage of 0.25 V (V_{RF}) which corresponds to a modulation index of MI(σ)=0.05, and the bias V_{1DC} and V_{2DC} are set to 0 and $V_{\pi}/2$, respectively. Simulated optical spectra are shown in Fig. 3.11, where $V_{2DC_{op}}$ is set to 5.3V and $V_{1DC_{op}}$ is set to 0, 2.2 and 4.0V, respectively. It is seen that OSSB modulation is always obtained. It is clearly observed

that OCSR is varied by changing the bias voltage. This confirms that OSSB modulation and tunability of OCSR are obtained simultaneously.

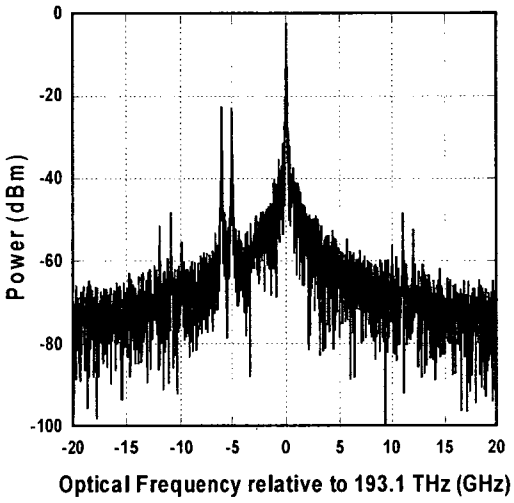

(a)

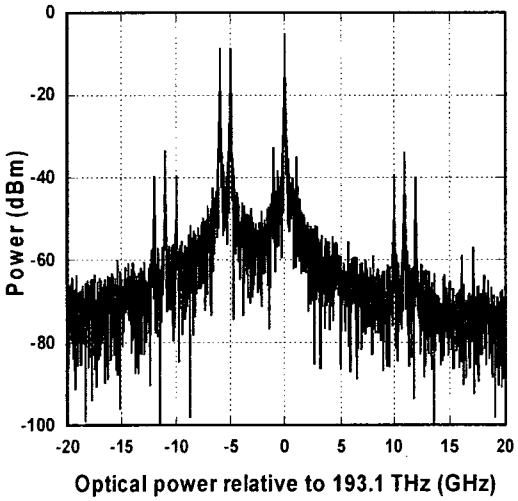

(b)

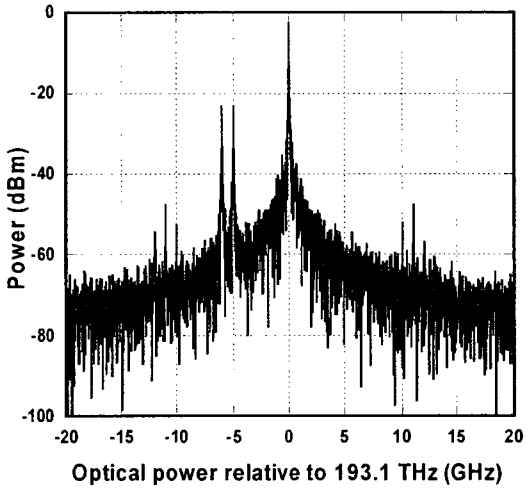

(c)

Figure 3.11 Simulated optical spectra for the proposed modulator, where $V_{2DC_{op}}$=5.3V and (a) $V_{1DC_{op}}$=0, (b) $V_{1DC_{op}}$=2.2 V, and (d) $V_{1DC_{op}}$=4.0 V for the case of two RF signals.

From Fig. 3.11 it is seen when the bias value is varying, not only the OCSR will change, the high order distortions and IMDs will change also. For example, second order distortion at frequency 10 and -10 GHz relative to 193.1 GHz will change when using different $V_{1DC_{op}}$, and IMD2 at frequency 11 and -11 GHz relative to 193.1 GHz also changes with different $V_{1DC_{op}}$, the same to IMD3. Therefore, an optical filter is implemented to eliminate the high order distortions. Moreover, when we analyze the output power of RF signals, these factors have to be considered.

To show the tunability of OCSR, we set V_{1DC}=0, V_{2DC}=2.5 V which is equal to $\pi/2$ phase-shifted voltage, and $V_{2DC_{op}}$ = 5.3 V. It is assumed that RF signal has the frequency of f=5 GHz and the amplitude V_{RF} = 0.25, 0.5, 1, and 2.5 V, i.e. MI(σ)=0.05, 0.1, 0.2, and 0.5. Fig. 3.12 shows the calculated OCSR versus $V_{1DC_{op}}$ for the above MIs. Obviously, the OCSR can be changed from 23 to ~-13 dB by varying the bias voltage of $1DC_{op}$ port, depending on MI. Also observed is that the optimum OCSR of 0 dB is always obtained by varying the bias voltage. Calculated OCSR and simulation results are well matched in Fig. 3.3.

For MI more than 0.5 cases, the optimum OCSR=3 dB is still can be obtained which are not plotted in the Fig. 3.12. Since when high MIs are applied, the high order distortions and IMDs will increase considerably and degrade the system performance heavily, thus only the MIs less and equal to 0.5 are shown in this simulation.

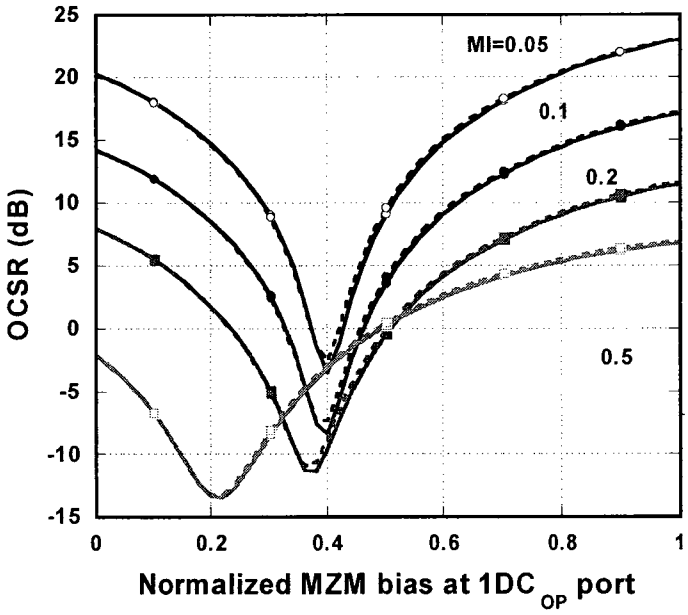

Figure 3.12 Calculated and simulated OCSR versus $1DC_{op}$

Fig. 3.13 shows simulated (dashed) and calculated (solid) RF power versus OCSR for MI= 0.05, 0.1, 0.2 and 0.5. As shown in Fig. 3.13, simulation results well match the theoretical values. It is seen that the RF output power is the same and the optimum OCSR is always 3 dB up to MI= 0.2. However, when MI =0.5 the maximum RF output power is about 5 dB lower than other MI cases, and the optimum OCSR is not 3 dB anymore. As stated in Chapter 2, when high MI is used, IMDs will be sufficiently large to impact the system performance and hardly to be filtered out. Contrarily, RF output power will decrease due to the fixed output power from modulators and optimum OCSR ceases to be 3 dB, which are proved in Fig. 3.13. Moreover, from Fig. 3.13 it is obtained that RF output power depends on OCSR and MI. This is different from one RF signal case which RF output power only depends on OCSR. The reason is when one RF signal employed,

there almost no IMDs and only high order distortions which are far from the desired RF signal and easily to be filtered out. Therefore, the RF output power is independent on MI.

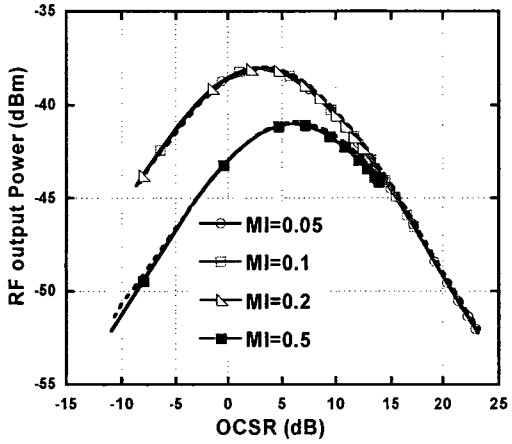

Figure 3.13 Impact of OCSR on RF power. Simulation: dot line and Theory: solid line.

3.3.2 Impact of IMDs

Since the IMD3 is so close to the RF signal that is hard to filter out, it will impact the system performance mostly. Based on Eq. (2.7a), Eq. (2.7b), Eq. (2.9a) and Eq. (2.9b), the theoretical and simulation results of $P_{RF_{1\_ideal}} / P_{IMD3}$ are ahown in Fig. 3.14.

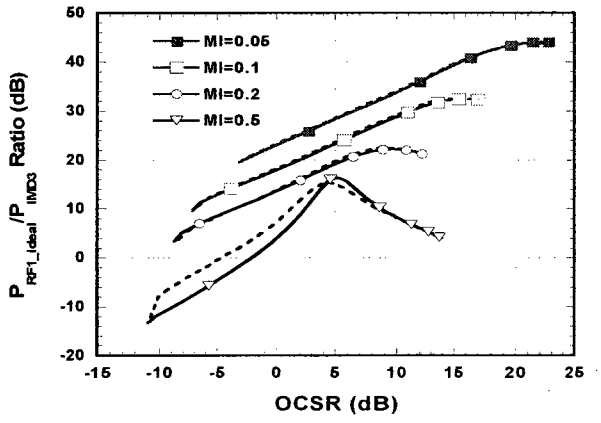

Figure 3.14 Ratio of $P_{RF_{1\_ideal}} / P_{IMD3}$. Simulated: dot line and Theory: solid line.

It is noted from Fig. 3.14 that when MI=0.05, 0.1 and 0.2, the ratios are nearly linearly increasing, and only for MI=0.5 case, there is a peak when OCSR is about 5 dB, then it decreases. According to Fig. 3.13, RF output power is increasing until OCSR equal to 3 dB where the maximum RF output power is obtained for low MIs cases, and OCSR equal to 5 dB for high MI like 0.5 case, then RF output power decreases. However, watching the four curves in Fig. 3.14, only when MI=0.5 there is a peak, other 3 curves are almost linear. The above shows that for low MIs, the power of IMD3 decreases faster than the power of RF signals after the optimum OCSR, so the ratios still are increasing. On the contrary, for high MI cases, the power of RF signals decrease faster than the IMD3 after the optimum OCSR.

Furthermore, it is obvious that when MI=0.05, with the increase of OCSR, the ratios are increasing too, and the curve is higher than other three MIs cases. Nevertheless, the average level of $P_{RF_{1\_ideal}} / P_{IMD3}$ goes down while MIs increase, like when MI=0.5 the curve is lowest. The above prove that the ratios depend on MI and OCSR stated in Chapter 2. In addition, it is seen that when OCSR=3 dB (optimum OCSR), ratios $P_{RF_{1\_ideal}} / P_{IMD3}$ are equal to 26 dB, 22 dB and 16 dB for MI= 0.05, 0.1 and 0.2 respectively, which indicate that impairment of IMD3 can be ignored. However, when Mi=0.5 and OCSR=3 dB, the ratio is only 9 dB, thus impairments of IMD3 have to be considered. It proves the analysis in Chapter 2 that this considered technique is more suitable for low MI again.

Comparing the simulation curve (dashed) with theoretical (solid) one when MI=0.5, it is noted that simulation values are larger than theoretical one. As mention in Chapter 2,

the reason is some IMDs will also contribute to RF_1 signal, like $-\omega_2$ beat with $-\omega_2+\omega_1$, and $-2\omega_1+\omega_2$ beat with $-\omega_1+\omega_2$. Therefore, according to Eq. (2.7a), Eq. (2.7b), Eq. (2.8a) and Eq. (2.8b) the ratio $P_{RF_{1\_ideal}} / P_{IMD_{\omega_1}}$ is plotted in Fig. 3.15.

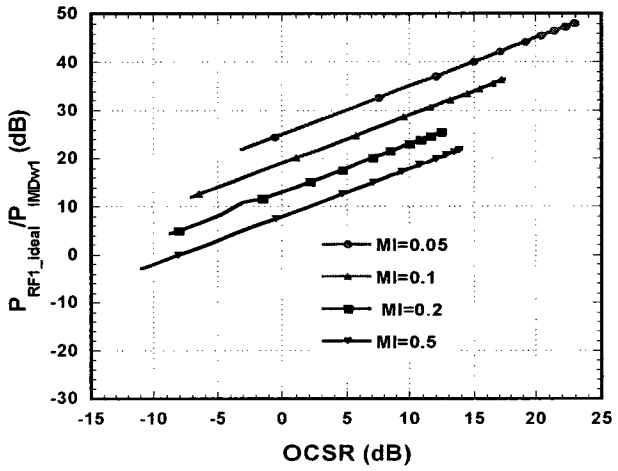

Figure 3.15 Ratio of $P_{RF_{1\_ideal}} / P_{IMD_{\omega_1}}$

Fig. 3.15 shows the ratios $P_{RF_{1\_ideal}} / P_{IMD_{\omega_1}}$ for different MIs cases. All four curves are nearly parallel and linearly go up while OCSR is increasing. Furthermore, the average level of the ratios is decreasing while the MI is increasing. For example, when MI=0.05 the curve is higher than other three MIs cases, but when MI=0.5 the curve is lowest. The above proves that ratios depend on MI and OCSR. In addition, in Fig. 3.15 it is seen that the ratios are equal to 28 dB, 24 dB and 16 dB when OCSR=3 dB and MI=0.05, 0.1 and 0.2 respectively, which indicate the impairment of IMD_{ω_1} can be disregarded when MI is low. However, when OCSR = 3 and MI=0.5 the ratio is 10 dB which means that the

contribution of IMD_{ω_1} to the desired signal RF_1 can't be ignored. This is the reason why simulation result is different from the theoretical result when MI =0.5 in Fig. 3.14.

According to Eq. (2.7a), Eq. (2.7b), Eq. (2.8a) , Eq. (2.8b), Eq. (2.9a) and Eq. (2.9b), ratio $P_{RF_1\_ideal} / P_{IMD_{total}}$ is obtained and plotted in Fig. 3.16

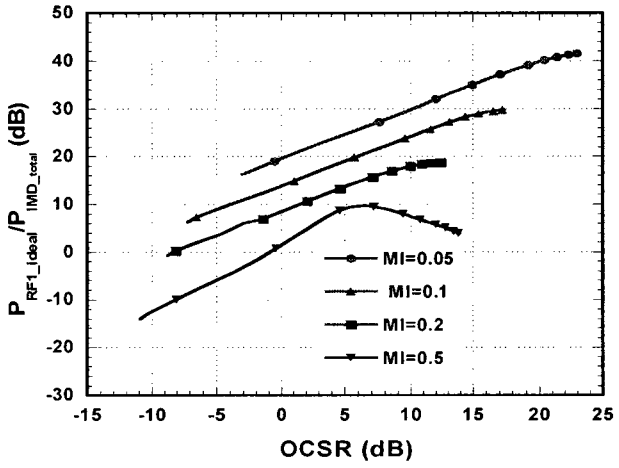

Figure 3.16 Ratio of $P_{RF_1\_ideal} / P_{IMD_{total}}$

Fig. 3.16 shows the effect of the nonlinear distortions IMD_{total}. It is seen that when OCSR= 3 dB and MI=0.05, 0.1, 0.2 and 0.5, the ratio are equal to 22 dB, 17 dB, 12 dB and 6 dB respectively, which indicates high MI like 0.5 will cause large $P_{IMD_{total}}$. Since $P_{IMD_{total}}$ is the summation of $P_{IMD_{\omega_1}}$ and P_{IMD3}, the ratio $P_{RF_1\_ideal} / P_{IMD_{total}}$ depends on the MI and OCSR as well. Fig. 3.16 repeatedly proves that when MI is low, IMDs can be neglected. On the contrary, when MI is high like 0.5, the power of IMDs will be significantly large even more than the desired RF signal, which will impact the

performance of the system severely. For this reason, this considered technique is better working with low MI.

Since IMD3 is highly detrimental to system performance, is it possible to suppress or even avoid it? It is found when the frequency differences between two RF signals are enlarged properly that IMD3 can be filtered out more easily. For instance, when the frequencies of RF_1 and RF_2 are 7 GHz and 10 GHz, the IMD3 will be far from the RF signals and more easily to be filtered out by electrical filters.

3.3.3 Phase Imbalance between Branch-A and Branch-B.

For the impact of phase imbalance between branch-A and branch-B, it is simply to insert an optical phase modulator in branch-B after MZM-2 to alter the phase imbalance. As an example, when MI is 0.2 and phase imbalance of 0^o, 15^o, and 30^o, respectively. Fig. 3.17 depicts OCSR versus ξ_I with a parameter of phase imbalance. It is seen that with the increase of phase imbalance the magnitude of OCSR tunability is reduced. However, with adjustment of bias voltage the optimum OCSR can be still obtained. For example, at the phase imbalance of 30^o the optimum OCSR of 3 dB can be obtained with $\xi_I = 0$, as shown in Fig. 3.17. In addition, similar to one RF signal case, the biases can be tuned to compensate for this phase imbalance, e.g. when the phase imbalance between branches A and B is $\Delta\varphi$, then it can be compensated by subtracting the voltage $V_\pi \Delta\varphi/180^0$ from the biases $V_{1DC_{op}}$ and V_{1DC}.

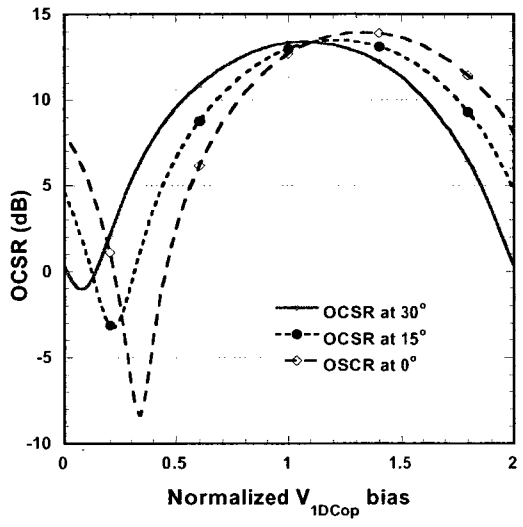

Figure 3.17 Impact of phase imbalance on OCSR with MI=0.2.

3.3.4 Mismatch between Splitting and Combining Ratios

By choosing MI=0.05, ER_1=ER_2=15 dB, and coupler's factor k_{in}=k_{out}= 0.3, 0.4 and 0.6, which means the two couplers' factors are synchronically changed, the curves of OCSR and RF_1output power versus V_{1DCop} are obtained simultaneously based on Eq. (2.6b), which are plotted in Fig. 3.18.

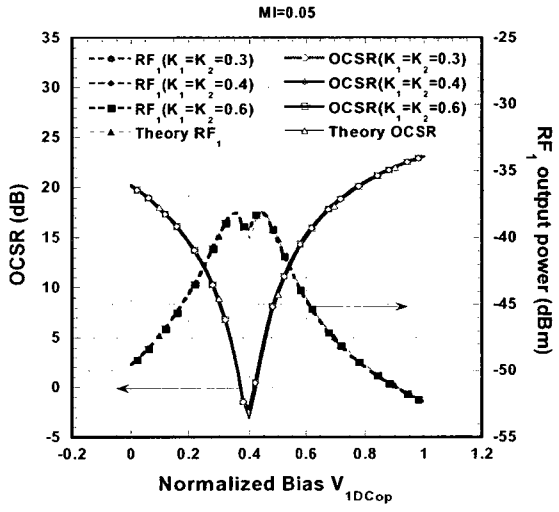

Figure 3.18 OCSR and RF power with same factor of couplers

In Fig. 3.18, it is seen that when k_{in}=k_{out}= 0.3, 0.4 and 0.6, the OCSR and RF output power curves always well match the theoretical results, which proves the theoretical analysis in Chapter 2 that OCSR and RF_1 output power are independent on the coupler's factor as long as two couplers' factors are the same.

Next, it is assumed that ER_1=ER_2=15 dB and k_{in} =0.4, by adjusting the k_{out} from 0.3 to 0.6, the maximum RF output power, relative optimum OCSR and bias voltage V_{1DCop} are investigated, and results are plotted in Fig. (3.19) and Fig. (3.20).

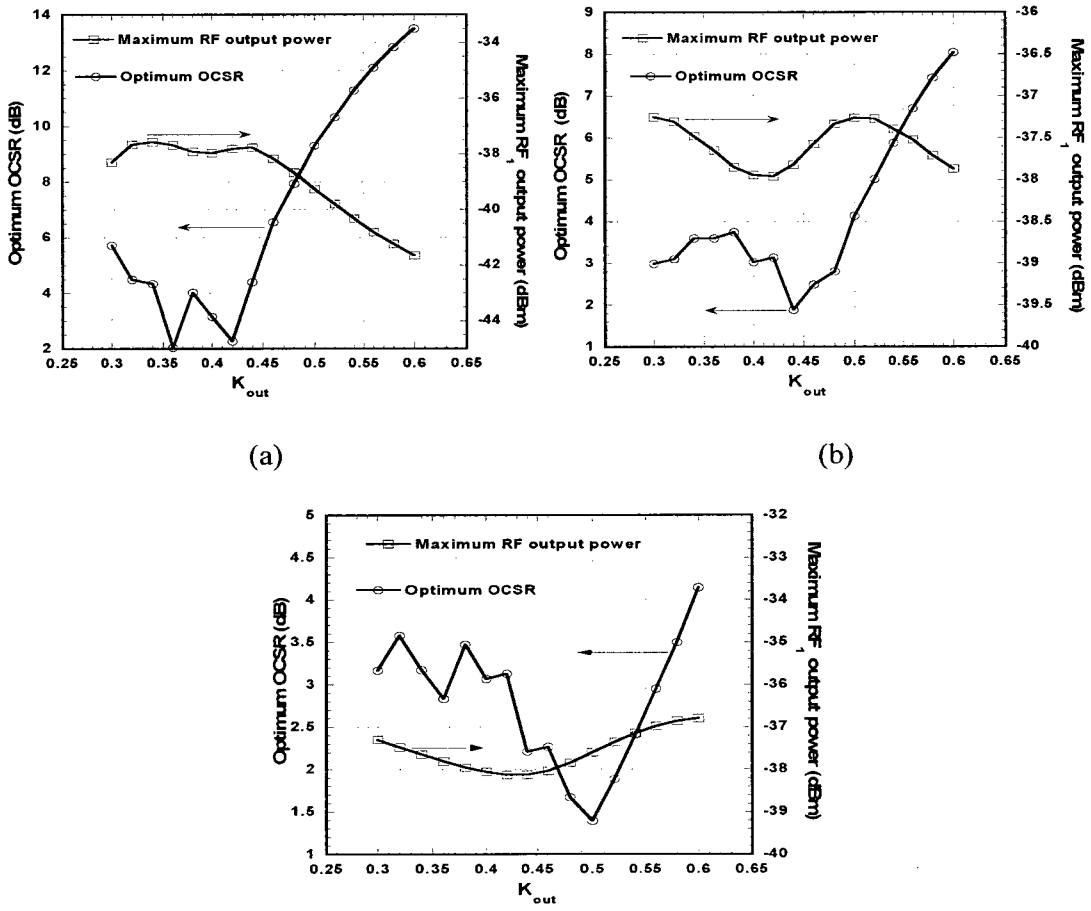

Figure 3.19 Optimum OCSR and Maximum RF_1 vs k_{out} when (a) MI=0.05, (b) MI=0.1, (c) MI=0.2

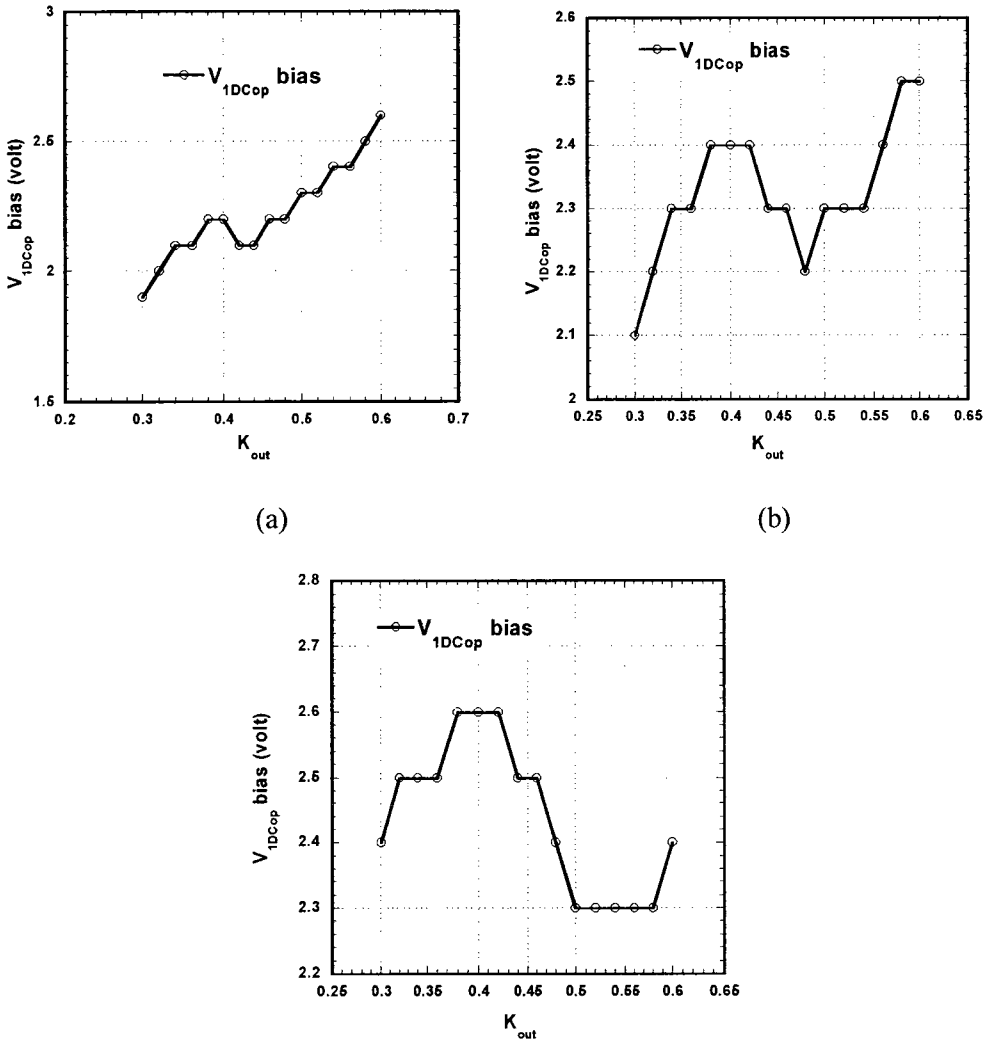

Figure 3.20 Optimum V_{1DCop} vs k_{out} when (a) MI=0.05, (b) MI=0.1, (c) MI=0.2

In Fig. 3.19(a), it is seen that when MI=0.05, the optimum OCSR varies between 2 and 13 dB, and the maximum RF_1 output power varies between -41.5 and -37.5 dBm, which suggests this considered technique is sensitive to imbalance of coupler's factors. However, when $k_{in} - k_{out}$ is kept within ±0.05, i.e. k_{in} is 0.4 and k_{out} varies between 0.35 and 0.45, the RF power varies by less than 1 dBm while OCSR changes by 2 dB for a

mismatch of less than 0.1, which can be achieved practically. In Fig. 3.19(b), when MI is 0.1, the optimum OCSR varies between 2 and 8 dB, and the maximum RF_1 output power varies between -38 and -37.2 dBm, which suggests this considered technique is sensitive to imbalance of coupler's factors. However, when $k_{in} - k_{out}$ is kept within ±0.05, the RF power varies by less than 0.6 dBm while OCSR changes by 1 dB for a mismatch of less than 0.1 which can be achieved practically. In Fig. 3.19(c), when MI is 0.2, the optimum OCSR varies between 1.4 and 4.2 dB, and the maximum RF_1 output power varies between -38.2 dBm and -36.8 dBm, which suggests this considered technique is sensitive to imbalance of coupler's factors. However, when $k_{in} - k_{out}$ is kept within ±0.05, the RF power varies by less than 0.4 dBm while OCSR changes by 1 dB for a mismatch of less than 0.1 which can be achieved practically.

Fig. 3.20 shows that the optimum V_{1DCop} corresponding to maximum RF output power is changing also. However, when the difference between splitting and combining factor is kept within ±0.05, the optimum V_{1DCop} doesn't change a lot.

In addition, the similar results of the optimum OCSR and maximum RF output power are obtained when choosing any other values of k_{in}. Therefore, it is obtained that this technique is sensitive to the mismatch of coupler's factors. Nevertheless, the optimum OCSR and the maximum RF output power will not hugely change when the mismatch between k_{in} and k_{out} is less than 0.1, and the corresponding optimum V_{1DCop} will only shift in a small range.

3.3.5 Mismatch between MZMs Extinction Ratios

Assume k_{in} and k_{out} both are 0.5 which means the coupler's factors not interfere the system performance, and then set the MZM-2 extinction ratio to 15dB, i.e. ER_2=15 dB, and tune the MZM-1 extinction ratio ER_1 from 10 to 20 dB. The results of the optimum OCSR and maximum RF output power are shown in Fig. 3.21 to investigate the impact of ER mismatch between two parallel MZMs.

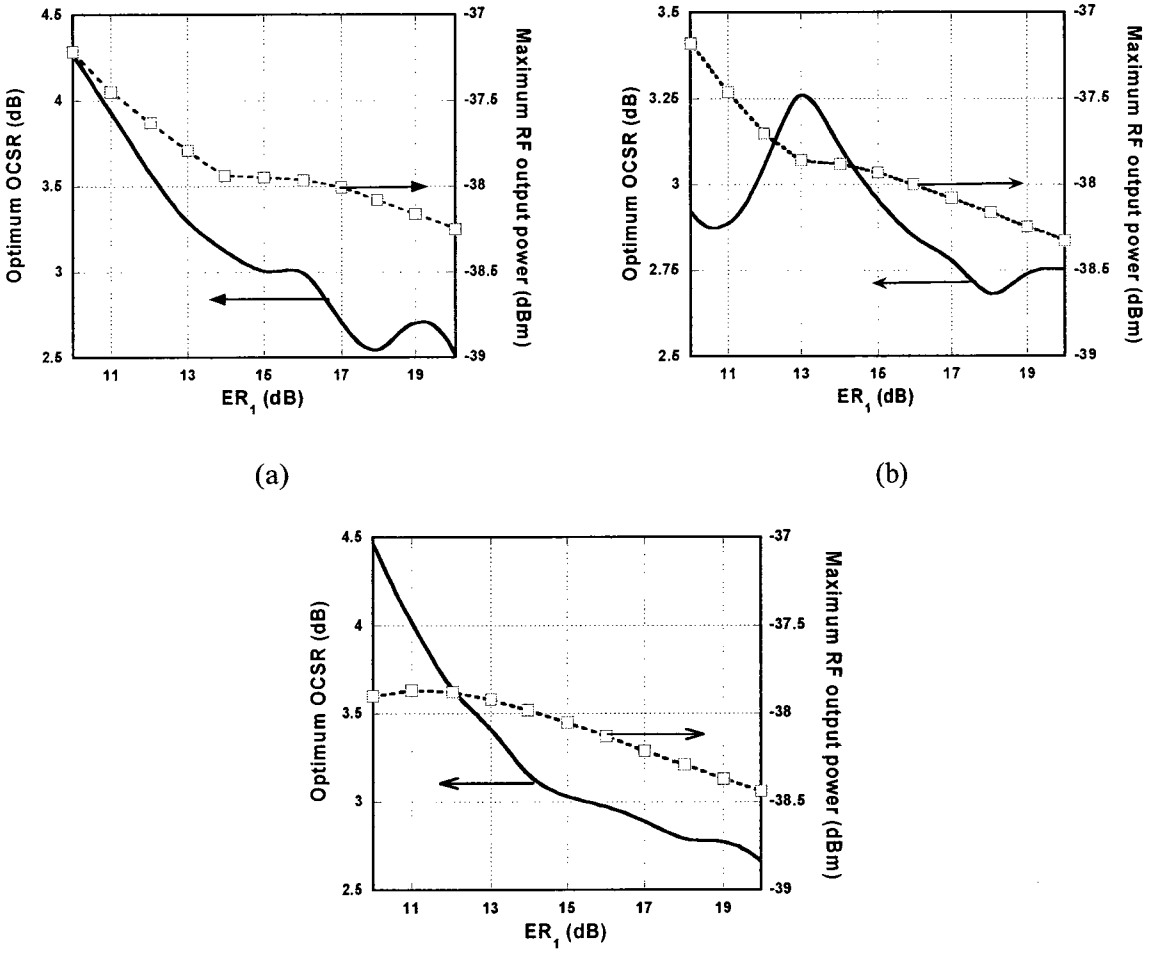

Figure 3.21 Optimum OCSR and Maximum RF_1 vs ER_1 when (a) MI=0.05, (b) MI=0.1, (c) MI=0.2

In Fig. 3.21(a), it is seen that when MI is 0.05, the optimum OCSR varies between 2.5 and 4.25 dB, and the maximum RF_1 output power varies between -37.3 and -38.3 dBm, which suggests this considered technique is sensitive to imbalance of modulator ERs. However, it is clearly when $ER_2 - ER_1$ is kept within ±2 dB, i.e. ER_2 = 15 dB and ER_1 varies between 13 and 17 dB, the RF power varies by less than 0.4 dBm while OCSR changes by 0.3 dB for a mismatch of less than 4 dB which can be achieved practically. In Fig. 3.21(b), when MI is 0.1, the optimum OCSR changed from 2.65 to 3.4 dB, the maximum RF_1 output power changed from -38.3 dBm to -37.2 dBm, which suggests this considered technique is sensitive to imbalance of modulator ERs. However, similar to Fig. 3.21 (a), the RF power varies by less than 0.3 dBm while OCSR changes by 0.5 dB for a mismatch less than 4 dB which can be achieved practically. In Fig. 3.21(c), when MI is 0.2, the optimum OCSR varies between 2.7 and 4.5 dB, and the maximum RF_1 output power varies between -37.8 and -38.4 dBm, which suggests this considered technique is sensitive to imbalance of modulator ERs. However, it is noted that the RF power varies by less than 0.4 dBm while OCSR changes by 0.4 dB for a mismatch of less than 4 dB which can be achieved practically. Similar results are obtained when ER_1 is fixed to 15 dB, and tune the ER_2. Therefore it is obtained that although this technique is sensitive to the mismatch of ERs, so long as the mismatch between ER_1 and ER_2 is less than 4 dB, the optimum OCSR and maximum output power will not change enormously. In addition, compared to the mismatch of coupler's factor, imbalance of modulator's ER doesn't impact the system's performance considerably.

3.3.6 Impact of Fiber Dispersion

By replacing the ideal back-to-back connection with SMF which has dispersion parameter of 16 ps/nm/km, dispersion slope of 0.08 ps/nm^2/km and attenuation of 0 dB/m, the impact of fiber dispersion is measured. In this simulation, it is assumed that MI equal to 0.05 and fiber lengths are 10, 30 and 50 km respectively, the simulation results of RF output power versus OCSR are plotted in Fig. 3.22.

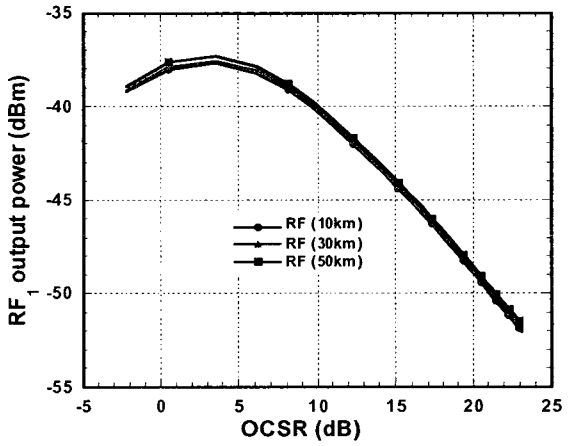

Figure 3.22 RF_1 output power vs OCSR with different fiber length

It is seen in Fig. 3.22 that three curves nearly overlap which means there is no notable power fading, i.e. this technique is robust to the fiber dispersion.

3.4 Summary

The simulation results have been presented in this chapter, which prove that this considered technique using two parallel MZMs to obtain the OSSB with tunable OCSR simultaneously is realizable. Comparing with the theoretical analyses in chapter 2, it is found that two OCSR are well matched and can be suppressed considerably which means

the efficiency of the modulation is highly improved. In addition, the simulation results show that the optimum OCSR are 0 dB and 3 dB when one RF signal and two RF signals are applied respectively, which are identical to theoretical results. Also it is found that RF output power only depends on OCSR for one RF signal case but depends on MI and OCSR for two RF signals case, which verifies the theoretical analyses.

According to the simulation results, it is noted that thermal bias shift will impact this considered modulation technique. However, by using bias voltage control method, OSSB with tunable OCSR and nearly stable RF output power are always achieved. Then some imperfect situations are considered as well, like mismatch of coupler's factors and mismatch of two parallel MZMs ERs. It is found that the optimum OCSR and maximum RF output power only change a little for the mismatch of coupler's factors are less than 0.1 and the mismatch of MZMs ERs are less than 4 dB, which can be achieved practically. In addition, the impacts of phase imbalance between branch-A and branch-B are also measured, and the simulation results indicate that this technique is sensitive to the phase imbalance. Nevertheless, by tuning the bias to compensate for the phase imbalance, OSSB modulation with tunable OCSR is always achieved.

Furthermore, the impacts of IMDs like IMD3 and IMD_{ω_1} are investigated as well. According to Fig. 3.14, Fig. 3.15 and Fig. 3.16, it is noted that the ratios are depending on OCSR and MI which means the IMDs will be considerably large and degrade the system performance heavily when high MIs are applied. This suggests that the considered technique is better working in small MI conditions which matches the theoretical analyses in Chapter 2 too.

Chapter 4

Experimental Results and Analysis

4.1 Experiment Verification

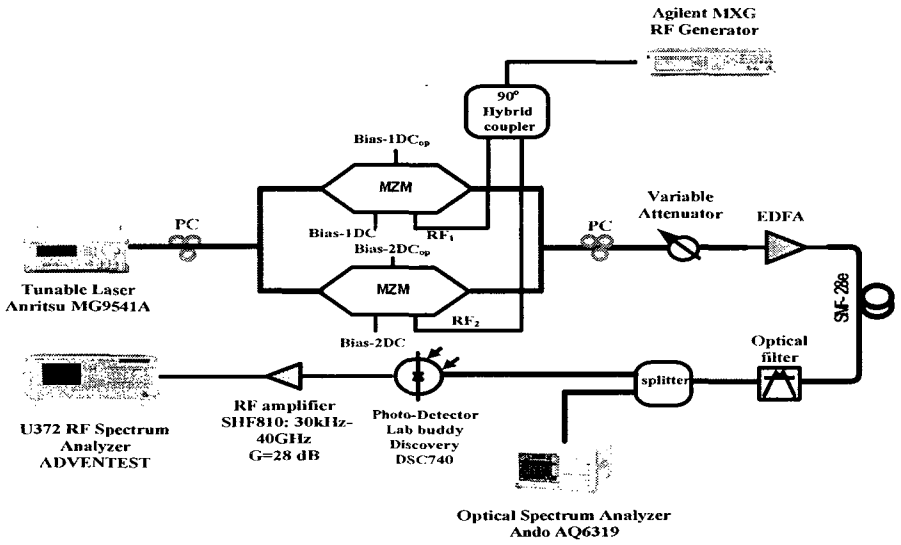

Figure 4.1 Experimental setup for an OSSB modulation with tunable OCSR. Dual-parallel MZM modulator is used. PC: Polarization controller.

The experimental setup is shown in Fig. 4.1. A continuous wave (CW) tunable laser source (Anritsu MG9541A) is used, which can offer a wavelength of 1550.5nm, line-width of 10 MHz, and output power of 0 dBm laser. A local oscillator sinusoidal signal from an RF generator (Agilent MXG) with frequency of 5.0 GHz and power of 5 dBm is injected into the 90° hybrid coupler, and then it is applied on the port RF_1 and RF_2 of the COVEGA dual-parallel modulator, which has half wave switching voltage V_π of 6.5-7.5 V, optical insertion loss of 5.5 dB, and an extinction ratio of 20 dB. By tuning the voltage

of port $1DC_{op}$ i.e. V_{1DCop} and $2DC_{op}$ i.e. V_{2DCop}, OSSB modulation and tunable OCSR can be achieved. The modulated optical signal is then transmitted through an SMF fiber, here, an EDFA is used to compensate for all optical loses and maintains power of 1 dBm to the optical filter. In addition, a variable attenuator (VA) is also used to adjust the power. Using an optical spectrum analyzer (AQ6319 from ANDO) that follows the EDFA, the output optical spectrum (jumped) is clearly investigated. Then the signal passes through an amplifier of 28 dB gain. At the end, the output RF spectrum can be measured by a spectrum analyzer (ADVANTEST U372). Table 4.1 shows the parameter settings for the setup in Fig. 4.1.

Table 4.1 Physical parameters for the experiment

Optical wavelength	1550.5 nm
Optical power	0 dBm
Optical line-width	10 MHz
RF signal frequency	5 GHz
RF input power	5 dBm
Mach-Zehnder V_π	7 V
Mach-Zehnder insertion loss	5.5 dB
Mach-Zehnder extinction ratio	20 dB
EDFA output power	1 dBm
RF amplifier gain	28 dB
Elec. Spectrum analyzer's resolution	100 Hz

To show the realization of OSSB modulation and the tunability of OCSR, optical signal's spectrum following the EDFA are shown in Fig. 4.2(a), 4.2(b) and 4.2(c).

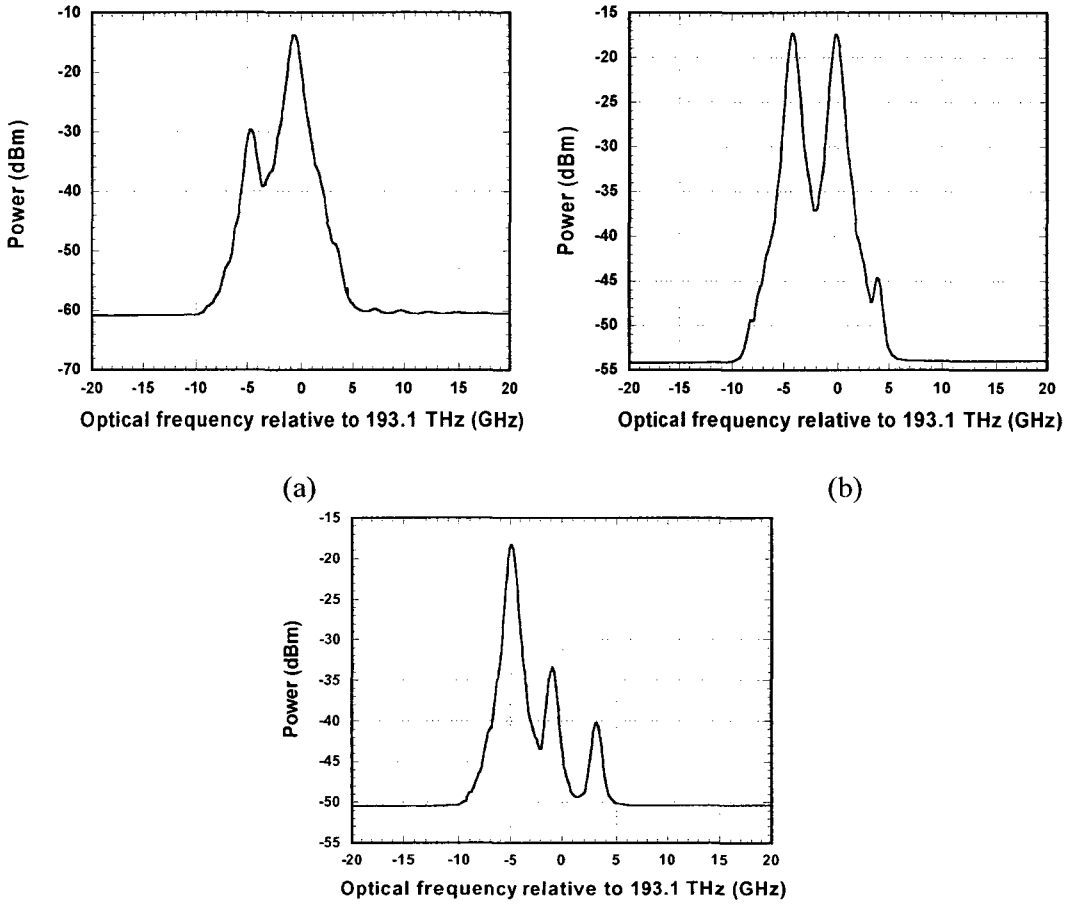

Figure 4.2 Optical Spectrum when V_{2DCop}=1.041 V and (a) V_{1DCop}=1.5V, (b) V_{1DCop}=1.04V, and (c) V_{1DCop}=0.623 V

First, the voltage of port 1DC and 2DC used to realize OSSB modulation are fixed when the single-side band is achieved. Then we keep V_{2DCop} =1.041V and tune V_{1DCop} continuously. By observing Fig. 4.2(a), it is found that OCSR is 16 dB when V_{1DCop} =1.5V, then after tuning OCSR is equal to 0 when V_{1DCop}=1.04V, which is shown is Fig.

4.2(b). Furthermore, even minus OCSR=-15.2 dB can be achieved when V_{1DCop}=0.623 V, which is shown in Fig. 4.2(c). It is also seen in Fig. 4.2(c) that the distortion is considerably large, which will impact the system performance. According to Fig. 4.2, it is clear that OCSR can be hugely improved by tuning the bias of port $1DC_{op}$ and $2DC_{op}$, which proves that theoretical analyses of the considered technique and simulation results are correct.

Next, the measured OCSR and RF output power versus normalized bias $\xi_1 (V_{1DCop}/V_\pi)$ are showed in Fig. 4.3 to validate theoretical and simulation results(offset bias are concerned here). Considering the system loss, it is found that RF signal with 5 dBm input power is approximately equal to MI=0.05. Moreover, in order to compare with the theoretical and simulation results, an 8 dBm input RF signal (about MI=0.1) is also considered. It is seen in Fig. 4.3 that the measured OCSR varies from -19 to 27 dB when MI=0.05, and changes from -8 to 26 dB when MI=0.1, which indicate that huge improvement of OCSR is obtained and the optimum OCSR=0 always can be achieved. Moreover, the experiment results have similar trend to theory and simulation, even though not totally matched. The reason is that OCSR depends on many parameters like mismatch of the coupler's factors, finite modulator ER imbalance, bias shift, and experiment errors, etc.

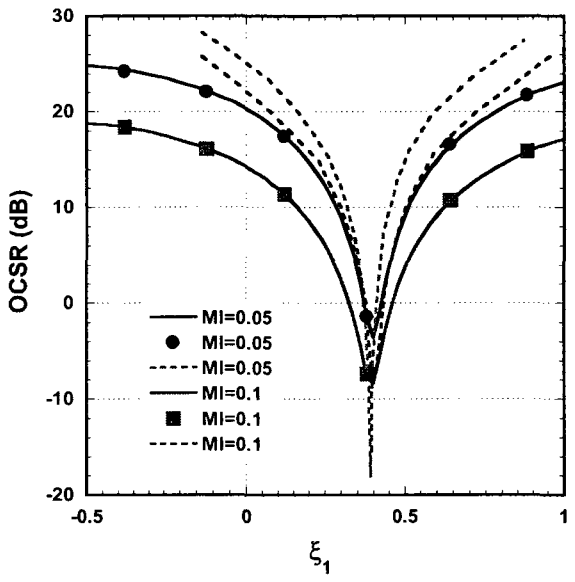

Figure 4.3 Measured OCSR vs $\xi 1$ with comparison to simulated and theoretical results. Theory: solid line, Simulation: dot line and Experiment: dash line.

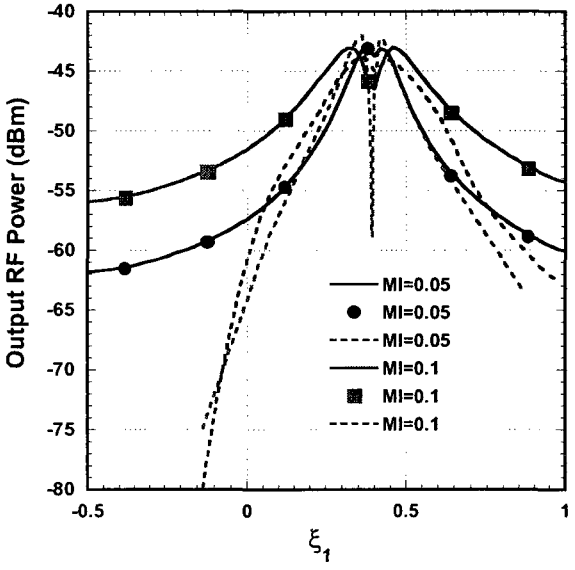

Figure 4.4 Measured RF vs ξ_1 with comparison to simulated and theoretical results. Theory: solid line, Simulation: dot line and Experiment: dash line.

Correspondingly, Fig. 4.4 shows the RF output power versus ξ_1. It is found that measured RF power has similar trend to the theoretical and simulation results and the maximum values of them are almost the same. In addition, comparing Fig. 4.3 with Fig. 4.4, it is obvious that the measured RF output power well matches the experiment OCSR.

To further show the relation between the OCSR and RF output power, OCSR versus RF output power is plotted in Fig. 4.5, which states that the experiment has the same trend to the theory and simulation. This proves the theoretical analysis that RF output power depends on the OCSR for one RF signal case. In addition, it is noted that experimental results are not totally matched the theoretical and simulation ones, especially when the OCSR is minus. The main reason is the distortion which is shown in Fig. 4.2(c). It is seen that when OCSR is minus, the distortion is not ignorable. The cause of formation is the imperfect situations and system noise which are inevitable.

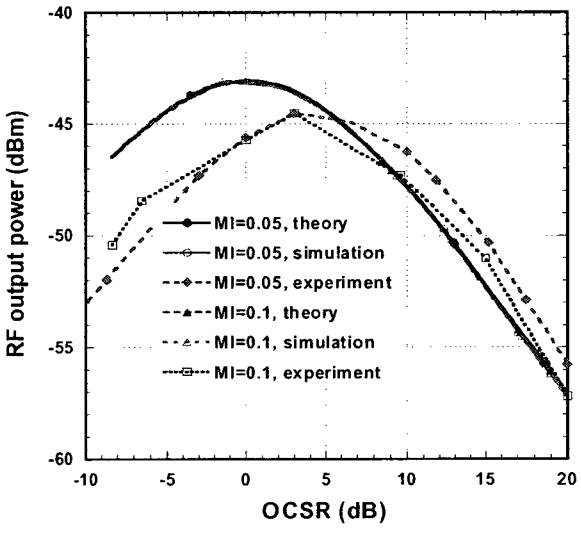

Figure 4.5 OCSR versus RF output power

4.2 Summary

In this chapter, the considered modulation technique is experimentally verified. It is well shown that the OSSB with tunable OCSR is achieved and good agreement with theory and simulation is obtained. Due to the imperfect situations like mismatch of coupler's factor, mismatch of MZM ERs, bias shift and system noise, a small difference is observed. In addition, the application of UWB signal will be considered as future work.

Chapter 5

Conclusion and Future Work

5.1 Concluding Remarks

In this thesis, a simple and convenient modulation technique using two parallel MZMs for RoF systems is considered and the theoretical analyses are presented. With such a modulator, the OSSB modulation with tunable OCSR can be realized only by adjusting the DC bias of MZMs. Two cases are concerned: one RF signal and two RF signals driving the considered modulator, respectively. The theoretical analysis is finally verified by computer simulations and experiments.

Moreover, the impacts of the non-ideal situations on the tunability of OCSR, RF output power and OSSB modulation are investigated, such as voltage drifting due to temperature, mismatch of the two integrated MZMs extinction ratios, mismatch of the optical splitting and combining coupler's ratios at input and output of the device, and phase imbalance between the two MZMs. It is found that the optimum setting of DC biases for OSSB modulation and the maximum RF power are sensitive to those imperfections. However, we have shown that DC bias control can be applied to compensate the drift of thermal voltage drift. After the compensation, OSSB modulation is obtained over an operating temperature range of 0 ~ 70°C with the maximum RF power change of less than 0.1 dB due to bias drift.

For the case of one tone signal, it is found that the optimum OCSR is 0 dB. For imperfect situations, in certain range, mismatch of the coupler's factors, mismatch of

MZMs ER and phase imbalance will not be the major causes to vary the OCSR. It is observed that OCSR changes less than 0.5 dB when a mismatch of coupler's factor is less than 0.1, and varies less than 1 dB when a mismatch of MZMs ER is less than 4 dB, which can be achieved practically. Furthermore, it is noted that RF output power only depends on the OCSR, and almost constant maximum RF power can be achieved for any phase imbalance between the two MZMs.

For the two tone signals case, it is found that the optimum OCSR is 3 dB, and similar to one tone situation, mismatch of the coupler's factors, mismatch of the MZMs ER and phase imbalance will influence the OCSR. However, it only varies less than 2 dB when a mismatch of coupler's factor is less than 0.1, and changes less than 0.5 dB when a mismatch of MZMs ER is less than 4 dB, which can be achieved practically. Furthermore, it is noted that RF output power depends on OCSR and MI which is different from one RF signal case. The main reason is when high MI is applied, the IMDs will increase, and as a result, the RF output power will decrease. Moreover, almost constant maximum RF power can be achieved for any phase imbalance between the two branches of the device.

Furthermore, with the theoretical analyses and simulation results, it is noted that IMDs will be considerable large when high MI applied. For example, when MI=0.5, the ratio $P_{RF_1\_ideal} / P_{IMD_{total}}$ is only 6 dB, i.e. IMDs can't be ignored. Therefore, this considered modulation technology is more suitable for working in low MI condition. In addition, by replacing the ideal back-to-back connection with SMF, the advantage of this considered technique that is robust to chromatic dispersion has been proved.

At the end, the performance of the considered technique is verified by experiment. The results are in good agreements with the theoretical analyses and simulation results. The deviations are discussed and considered to be acceptable.

5.2 Future Work and Direction

The research contributions presented in this thesis may be extended in several ways. First, we will focus on the transmission of different kinds of modulation formats e.g. DPSK, QPSK and QAM, which are commonly utilized to transmit in RoF systems.

Second, it would be beneficial to simulate and experimentally demonstrate when UWB signal is applied on this modulation scheme, which is considered as future telecommunication development direction. By investigating the error vector magnitude (EVM), we can find out whether this modulation technology suits to UWB signal transporting.

Third, because this technique is sensitive to the mismatch between two coupler's factors and MZMs ER, it is necessary to figure out the compensation method to obtain the best system performance in the future work.

At last, as previously mentioned in chapter 1, this modulation technique is for RoF system, so it would be interesting to experimentally measure the system performance when it is applied in the real RoF communication system with various kinds of multiplexing and up/downlink duplexing.

APPENDIX-A

Detailed Derivation for the modulator driven by One RF Signal

1.1 Derivation of Eq. (2.1)

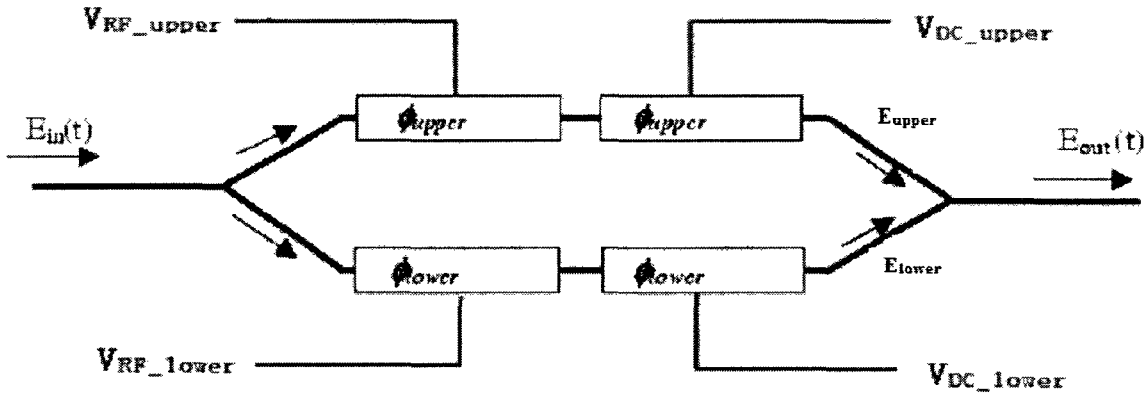

Figure A.1 Schematic of the Mach-Zehnder modulator

Fig. A.1 shows us the schematic of the dual-electrode MZM. The output optical field from a dual-electrode MZM can be written as

$$E_{out}(t) = E_{upper} + E_{lower} = \frac{E_{in}\sqrt{t_{ff}}}{\sqrt{2}}(ae^{i\varphi_{upper}} + re^{i\varphi_{lower}}) \quad \text{(A.1)}$$

where E_{upper} and E_{lower} are the density of optical field of upper and lower branches respectively, a represents the power split ratio of upper branch, $r = \sqrt{1-a^2}$ represents the power split ratio of lower branch, E_{in} is the density of the input optical power, we use the convention of the optical field by $E_{in}(t) = E_0 e^{i\omega_c t}$ where the ω_c is the angular frequency of the optical carrier, E_0 is the amplitude of the optical field, and t_{ff} represents the optical insertion loss of the dual-electrode MZM.

The upper and lower phase applied to the two branches of the dual-electrode MZM are

$$\varphi_{upper} = \frac{\pi}{V_\pi} V_{DC\_upper} + \frac{\pi}{V_\pi} V_{RF\_upper}(t) \tag{A.2}$$

$$\varphi_{lower} = \frac{\pi}{V_\pi} V_{DC\_lower} + \frac{\pi}{V_\pi} V_{RF\_lower}(t) \tag{A.3}$$

where V_{DC_upper} and V_{DC_lower} are the DC voltage applied to the dual-electrode MZM. $V_{RF\_upper}(t)$ and $V_{RF\_lower}(t)$ are the RF voltage applied to the upper and lower branches of the MZM, respectively. V_π is the required voltage for the phase shift of π.

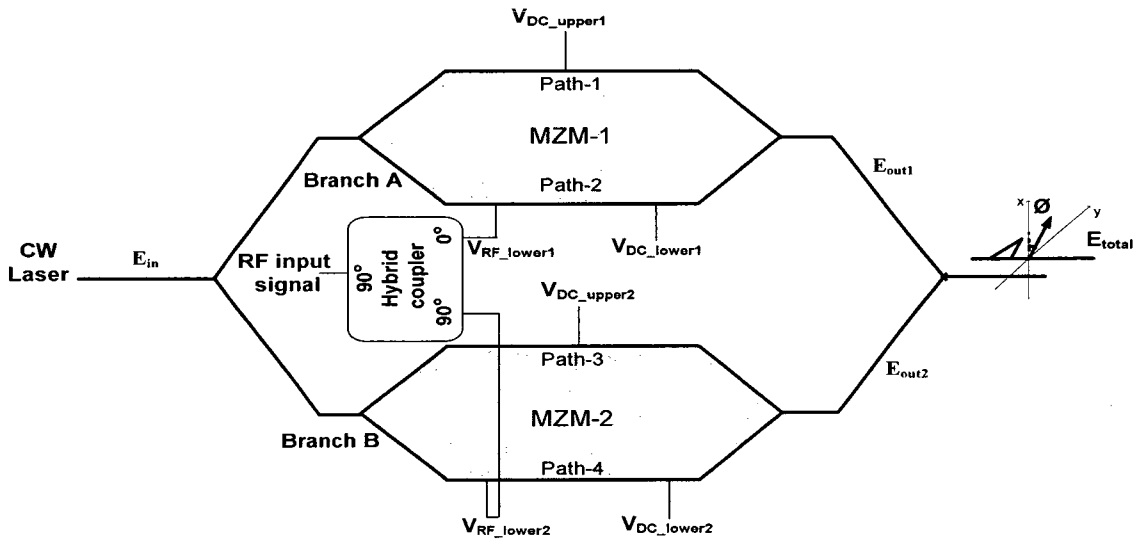

Figure A.2 Considered optical OSSB modulator with tunability of optical carrier to sideband ratio

Figure A.2 shows the principle of the considered modulation technology used two parallel dual-electrode MZMs, and the injected light is split into two branches A and B by an 3-dB optical splitter. In each branch there is a DE-MZM, i.e. MZM-1 in branch A and MZM-2 in branch B, and the initial optical field of them change to $\frac{E_{in}}{\sqrt{2}}$. After optical modulation, the two branches are combined by another optical combiner. The total output optical field can be written as $E_{total} = E_{out1} + E_{out2}$.

Consider one RF signal RF=$\sqrt{2}V_{RF}[\cos(\omega t + \theta)]$ applied on the modulator, where V_{RF}, ω, and θ are modulation voltage, frequency, and phase of the RF input signal. From the Fig. A.2 we can find that for the first MZM, the RF signal is applied on the lower branch of the MZM-1, i.e.V_{RF_lower1}, and no signal applied on upper branch, i.e. $V_{RF\_upper1} = 0$. The RF applied voltage applied to lower branch of the dual-electrode MZM is given by

$$V_{RF\_lower1}(t) = V_{RF}\cos(\omega t + \theta) \tag{A.4}$$

We set V_{DC_lower1} and V_{DC_lower2} to the quadrature point, i.e. $V_{DC\_lower1} = 0$ and $V_{DC\_lower2} = \frac{V_\pi}{2}$, and tune the V_{DC_upper1}.

The output optical field from the first dual-electrode MZM becomes

$$E_{out1}(t) = \frac{E_{in}\sqrt{t_{ff}}}{2}(ae^{i\varphi_{upper1}} + re^{-i\varphi_{lower1}}) \tag{A.5}$$

$$\varphi_{upper1} = \frac{\pi}{V_\pi}V_{DC\_upper1} + \frac{\pi}{V_\pi}V_{RF\_upper1} = \frac{\pi}{V_\pi}V_{DC\_upper1} \tag{A.6}$$

$$\varphi_{lower1} = \frac{\pi}{V_\pi}V_{DC\_lower1} + \frac{\pi}{V_\pi}V_{RF\_lower1} = \frac{V_{RF}\pi}{V_\pi}\cos(\omega t + \theta) \tag{A.7}$$

Substituting Eq. (A.7) and Eq. (A.6) into Eq. (A.5), we get

$$E_{out1}(t) = \frac{\sqrt{t_{ff}}}{2}E_0 e^{i\omega_c t}\left\{ae^{i\frac{V_{DC\_upper1}}{V_\pi}\pi} + re^{-i\frac{V_{RF}}{V_\pi}\pi\cos(\omega t+\theta)}\right\} \tag{A.8}$$

For the second MZM, the RF signals are applied on the lower branch of the MZM-2 i.e. V_{RF_lower2} and no signal applied on upper branch, i.e. $V_{RF\_upper2} = 0$. The RF applied voltage applied to lower branch of the second dual-electrode MZM is given by

$$V_{RF\_lower2}(t) = V_{RF}\cos(\omega t + \theta - \frac{\pi}{2}) \tag{A.9}$$

As we mentioned before, we set V_{DC_lower1} and V_{DC_lower2} to the quadrature point, i.e. $V_{DC\_lower1} = 0$ and $V_{DC\_lower2} = \frac{V_\pi}{2}$, and tune the V_{DC_upper2}.

The output optical field from the second dual-electrode MZM-2 becomes

$$E_{out2}(t) = \frac{E_{in}\sqrt{t_{ff}}}{2}(ae^{i\varphi_{upper2}} + re^{-i\varphi_{lower2}}) \tag{A.10}$$

$$\varphi_{upper2} = \frac{\pi}{V_\pi}V_{DC\_upper2} + \frac{\pi}{V_\pi}V_{RF\_upper2} = \frac{\pi}{V_\pi}V_{DC\_upper2} \tag{A.11}$$

$$\varphi_{lower2} = \frac{\pi}{V_\pi}V_{DC\_lower2} + \frac{\pi}{V_\pi}V_{RF\_lower2} = \pi\left[\frac{V_{RF}}{V_\pi}\cos(\omega t + \theta - \frac{\pi}{2}) + \frac{1}{2}\right] \tag{A.12}$$

Substituting Eq. (A.11) and Eq. (A.12) into Eq. (A.10), we get

$$E_{out2}(t) = \frac{\sqrt{t_{ff}}}{2}E_0 e^{i\omega_c t}\left\{ae^{i\frac{V_{DC\_upper2}}{V_\pi}\pi} + re^{-i\frac{\pi}{2}}e^{-i\frac{V_{RF}}{V_\pi}\pi\cos(\omega t+\theta-\frac{\pi}{2})}\right\} \tag{A.13}$$

After combining E_{out1} and E_{out2} together, we obtain the density of optical field for our considered technology as

$$E_{total} = E_{out1} + E_{out2} = \frac{\sqrt{t_{ff}}}{2}E_0 e^{i\omega_c t}\left\{ae^{i\xi_1\pi} + ae^{i\xi_2\pi} + re^{-i\sigma\pi\cos(\omega t+\theta)} + re^{-i\frac{\pi}{2}}e^{-i\sigma\pi\cos(\omega t+\theta-\frac{\pi}{2})}\right\} \tag{A.14}$$

where $\sigma = \frac{V_{RF}}{V_\pi}$, $\xi_1 = \frac{V_{DC\_upper1}}{V_\pi}$, and $\xi_2 = \frac{V_{DC\_upper2}}{V_\pi}$.

By applying the Jacobi-Anger expansion $e^{iz\cos\varphi} = \sum_{n=-\infty}^{\infty} i^n J_n(z)e^{in\varphi}$ to Eq. (A.14), we get

$$E_{total}(t)=\frac{\sqrt{t_{ff}}}{2}E_0e^{i\omega_c t}\left\{ae^{i\xi_1\pi}+ae^{i\xi_2\pi}+r\sum_{n=-\infty}^{\infty}\left[i^nJ_n(\sigma\pi)e^{in(\omega t+\theta+\pi)}-i^{n+1}J_n(\sigma\pi)e^{in(\omega t+\theta+\frac{\pi}{2})}\right]\right\}$$
$$=\frac{\sqrt{t_{ff}}}{2}E_0e^{i\omega_c t}\left\{a\left(e^{i\xi_1\pi}+e^{i\xi_2\pi}\right)+r\sum_{n=-\infty}^{\infty}\left[J_n(\sigma\pi)e^{in(\omega t+\theta)}\left((-i)^n-i^{2n+1}\right)\right]\right\} \quad \text{(A.15)}$$

Equation (A.15) is Eq. (2.1).

1.2 Derivation of Eq. (2.2a)

According to the Eq. (A.15), when n=0, the term corresponding to optical carrier E_{oc} is obtained:

$$E_{oc}=\frac{\sqrt{t_{ff}}}{2}E_0e^{i\omega_c t}\left\{a\left(e^{i\xi_1\pi}+e^{i\xi_2\pi}\right)+rJ_0(\sigma\pi)(1-i)\right\}$$
$$=\frac{\sqrt{t_{ff}}}{2}E_0e^{i\omega_c t}\left\{a\left(e^{i\xi_1\pi}+e^{i\xi_2\pi}\right)+\sqrt{2}rJ_0(\sigma\pi)e^{-i\frac{\pi}{4}}\right\} \quad \text{(A.16)}$$

When n=1, the upper RF fundamental component $E_{+\omega}$ is obtained

$$E_{+\omega}=\frac{\sqrt{t_{ff}}}{2}E_0e^{i\omega_c t}\left\{r\sum_{n=-\infty}^{\infty}\left[J_n(\sigma\pi)e^{in(\omega t+\theta)}\left((-i)^n-i^{2n+1}\right)\right]\right\}$$
$$=\frac{\sqrt{t_{ff}}}{2}E_0e^{i\omega_c t}\left\{r\left[J_1(\sigma\pi)e^{i(\omega t+\theta)}\left((-i)^1-i^{2+1}\right)\right]\right\}=0 \quad \text{(A.17)}$$

it means the upper RF sideband is eliminated and OSSB is obtained.

When n=-1, we also can obtain the lower sideband $E_{-\omega}$

$$
\begin{aligned}
E_{-\omega} &= \frac{\sqrt{t_{ff}}}{2} E_0 e^{i\omega_c t} \left\{ r \sum_{n=-\infty}^{\infty} \left[J_n(\sigma\pi) e^{in(\omega t+\theta)} \left((-i)^n - i^{2n+1} \right) \right] \right\} \\
&= \frac{\sqrt{t_{ff}}}{2} E_0 e^{i\omega_c t} \left[r J_{-1}(\sigma\pi) e^{-i(\omega t+\theta)} \left((-i)^{-1} - i^{-2+1} \right) \right] \\
&= \sqrt{t_{ff}} E_0 e^{i\omega_c t} \cdot r \cdot \left[J_{-1}(\sigma\pi) e^{-i(\omega t+\theta-\frac{1}{2}\pi)} \right]
\end{aligned}
\tag{A.18}
$$

Applying $J_{-n}(z) = (-1)^n J_n(z)$ to Eq. (A.18) we obtain

$$
E_{-\omega} = -\sqrt{t_{ff}} E_0 e^{i\omega_c t} r J_1(\sigma\pi) e^{-i(\omega t+\theta-\frac{1}{2}\pi)} . \tag{A.19}
$$

Based on Eq. (A.16) and Eq. (A.19), the optical carrier-to-sideband ratio in power is obtained

$$
\begin{aligned}
OCSR &= \frac{|E_{oc}|^2}{|E_{-\omega}|^2} = \frac{E_{oc} \cdot E_{oc}^*}{E_{-\omega} \cdot E_{-\omega}^*} = \frac{\frac{\sqrt{t_{ff}}}{2} E_0 e^{j\omega t} \left\{ a e^{j\xi_1\pi} + a e^{j\xi_2\pi} + \sqrt{2} r J_0(\sigma\pi) e^{-i\frac{\pi}{4}} \right\} \cdot \frac{\sqrt{t_{ff}}}{2} E_0 e^{j\omega t} \left\{ a e^{-i\xi_1\pi} + a e^{-i\xi_2\pi} + \sqrt{2} r J_0(\sigma\pi) e^{i\frac{\pi}{4}} \right\}}{\left\{ -\sqrt{t_{ff}} E_0 e^{j\omega t} \cdot r \cdot \left[J_1(\sigma\pi) e^{-i(\omega t+\theta-\frac{1}{2}\pi)} \right] \right\} \cdot \left\{ -\sqrt{t_{ff}} E_0 e^{j\omega t} \cdot r \cdot \left[J_1(\sigma\pi) e^{i(\omega t+\theta-\frac{1}{2}\pi)} \right] \right\}} \\
&= \frac{2a^2 + a^2 (e^{j(\xi_1-\xi_2)\pi} + e^{j(\xi_2-\xi_1)\pi}) + 2r^2 J_0(\sigma\pi)^2 + \sqrt{2} a r J_0(\sigma\pi) \cdot e^{i\frac{1}{4}\pi} \cdot \left[e^{j\xi_1\pi} + e^{j\xi_2\pi} + e^{-i(\xi_1+\frac{1}{2})\pi} + e^{-i(\xi_2+\frac{1}{2})\pi} \right]}{4r^2 J_1^2(\sigma\pi)}
\end{aligned}
\tag{A.20}
$$

According to the exponential function $e^{i\theta} = \cos\theta + i\sin\theta$ we can transfer the Eq. (A.20) to

$$
OCSR = \frac{a^2 + a^2 \cos(\xi_1 - \xi_2)\pi + r^2 J_0^2(\sigma\pi) + a r J_0(\sigma\pi) \left[\cos\xi_1\pi + \cos\xi_2\pi - \sin\xi_1\pi - \sin\xi_2\pi \right]}{2r^2 J_1^2(\sigma\pi)} \tag{A.21}
$$

Equation (A.21) is Eq. (2.2a).

1.3 Derivation of Eq. (2.2b)

Because it is needed to measure the impacts of combiner-splitter imbalance and ER imbalance between the MZMs in simulation part, therefore we consider these parameters and define them by: splitter coupling factor k_{in}, combiner coupling factor k_{out}. ER_1 and ER_2 are the ER of the first and second dual-electrode MZM, respectively. For calculating reason, it is simply to define $h=\sqrt{k_{in}}$, $k=\sqrt{1-k_{in}}$, $f=\sqrt{k_{out}}$, $g=\sqrt{1-k_{out}}$, $p=\frac{1+\sqrt{ER_1}}{\sqrt{2(ER_1+1)}}$, $b=\sqrt{1-p^2}$, $c=\frac{1+\sqrt{ER_2}}{\sqrt{2(ER_2+1)}}$ and $d=\sqrt{1-c^2}$. Consequently, they can be grouped into 4 pairs: splitter pair, i.e. h and k; combiner pair, i.e. f and g; upper branch and lower branch power split ratio for the first dual-electrode MZM, i.e. p and b; upper branch and lower branch power split ratio for the second dual-electrode MZM, i.e. c and d.

For the first dual-electrode MZM, we use the same RF bias and DC bias as ideal situation, thus we can get Eq. (A.5), Eq. (A.6) and Eq. (A.7). However, the amplitude of the E_{in} signal will change. For example, consider MZM-1, at first, the E_{in} pass the splitting coupler upper line ($h\cdot E_{in}$), then it goes through the upper branch of the first dual-electrode MZM ($p\cdot h\cdot E_{in}$), finally, it pass the combining coupler ($p\cdot h\cdot g\cdot E_{in}$). Therefore, we get

$$\mathrm{E}_{\mathrm{upper1}} = p \cdot h \cdot g \cdot E_{in} = \frac{phg\sqrt{t_{ff}}}{\sqrt{2}} E_0 e^{i\omega_c t} e^{i\frac{V_{DC\_upper1}}{V_\pi}\pi} \tag{A.22a}$$

Using the same scenario we get

$$\mathrm{E}_{\mathrm{lower1}} = \frac{bhg\sqrt{t_{ff}}}{\sqrt{2}} E_0 e^{i\omega_c t} e^{-i\frac{V_{DC\_lower1}}{V_\pi}\pi} \tag{A.22b}$$

Using Eq. (A.22a) and Eq. (A.22b) we get

$$E_{out1}(t) = E_{upper1} + E_{lower1} = \frac{\sqrt{t_{ff}}}{\sqrt{2}} E_0 e^{i\omega_c t} \left\{ phge^{i\xi_1\pi} + bhge^{-i\sigma\pi\cos(\omega t+\theta)} \right\} \tag{A.23}$$

where $\sigma = \frac{V_{RF}}{V_\pi}$ and $\xi_1 = \frac{V_{DC\_upper1}}{V_\pi}$.

For the second dual-electrode MZM, we use the same RF bias and DC bias as ideal situation, thus we can get Eq. (A.10), Eq. (A.11) and Eq. (A.12). However, the amplitude of the E_{in} signal will change. For example, at first, the E_{in} pass the splitting coupler ($k \cdot E_{in}$), then it goes through the upper branch of the first dual-electrode MZM ($c \cdot k \cdot E_{in}$), finally, it pass the combining coupler ($c \cdot k \cdot f \cdot E_{in}$). Therefore, we get

$$\mathrm{E}_{\mathrm{upper2}} = \frac{c \cdot k \cdot f \cdot \sqrt{t_{ff}}}{\sqrt{2}} \cdot E_0 e^{i\omega_c t} e^{i\frac{V_{DC\_upper2}}{V_\pi}\pi} \tag{A.24a}$$

Using the same scenario we get

$$\mathrm{E}_{\mathrm{lower2}} = \frac{d \cdot k \cdot f \cdot \sqrt{t_{ff}}}{\sqrt{2}} \cdot E_0 e^{i\omega_c t} e^{-i(\frac{V_{DC\_lower2}}{V_\pi}+\frac{1}{2})\pi} \tag{A.24b}$$

Using Eq. (B.19a) and Eq. (B.19b) we get

$$E_{out2}(t) = E_{upper2} + E_{lower2} = \frac{\sqrt{t_{ff}}}{\sqrt{2}} E_0 e^{i\omega_c t} \left\{ ckfe^{i\xi_2 \pi} + dkfe^{-i\frac{\pi}{2}} e^{-i\sigma\pi\cos(\omega t+\theta-\frac{\pi}{2})} \right\} \tag{A.25}$$

where $\sigma = \frac{V_{RF}}{V_\pi}$ and $\xi_2 = \frac{V_{DC\_upper2}}{V_\pi}$.

According to Eq. (A.23) and Eq. (A.25) we can get

$$E_{total}(t) = E_{out1} + E_{out2} = \frac{\sqrt{t_{ff}}}{\sqrt{2}} E_0 e^{i\omega_c t} \left\{ phge^{i\xi_1 \pi} + ckfe^{i\xi_2 \pi} + bhge^{-i\sigma\pi\cos(\omega t+\theta)} + dkfe^{-i\frac{\pi}{2}} e^{-i\sigma\pi\cos(\omega t+\theta-\frac{\pi}{2})} \right\} \tag{A.26}$$

By applying the Jacobi-Anger expansion $e^{iz\cos\varphi} = \sum_{n=-\infty}^{\infty} i^n J_n(z) e^{in\varphi}$ to Eq. (A.26), we can get

$$E_{total}(t) = \frac{\sqrt{t_{ff}}}{\sqrt{2}} E_0 e^{i\omega_c t} \left\{ \begin{array}{l} phge^{i\xi_1 \pi} + ckfe^{i\xi_2 \pi} \\ +bhg \sum_{n=-\infty}^{\infty} i^n J_n(\sigma\pi) e^{in(\omega t+\theta+\pi)} \\ -dkf \sum_{n=-\infty}^{\infty} i^{n+1} J_n(\sigma\pi) e^{in(\omega t+\theta+\frac{\pi}{2})} \end{array} \right\} \tag{A.27}$$

When n=0 the optical carrier is obtained

$$E_{oc} = \frac{\sqrt{t_{ff}}}{\sqrt{2}} E_0 e^{i\omega_c t} \left\{ \begin{array}{l} phge^{i\xi_1 \pi} + ckfe^{i\xi_2 \pi} \\ +bhgJ_0(\sigma\pi) + dkfJ_0(\sigma\pi) e^{-i\frac{\pi}{2}} \end{array} \right\} \tag{A.28}$$

When n=-1, the lower sideband fundamental component of RF_1 signal is as follow

$$E_{-\omega_1} = \frac{\sqrt{t_{ff}}}{\sqrt{2}} E_0 e^{i\omega_c t} \begin{Bmatrix} bhg \cdot i^{-1} J_{-1}(\sigma\pi) e^{i[-1(\omega t+\theta+\pi)]} \\ -dkf \cdot J_{-1}(\sigma\pi) e^{i\left[-1(\omega t+\theta+\frac{\pi}{2})-\frac{\pi}{2}\right]} \end{Bmatrix}$$
$$= \frac{\sqrt{t_{ff}}}{\sqrt{2}} E_0 e^{i\omega_c t} \left\{ (bhg + dkf) \cdot J_1(\sigma\pi) e^{-i(\omega t+\theta+\frac{\pi}{2})} \right\} \tag{A.29}$$

According to Eq. (A.28) and Eq. (A.29) we can calculate the OCSR by

$$OCSR = \frac{|E_{oc}|^2}{|E_{-\omega_1}|^2} = \frac{\begin{pmatrix} phge^{i\xi_1\pi} + ckfe^{i\xi_2\pi} \\ +bhgJ_0(\sigma\pi) + dkfJ_0(\sigma\pi)e^{-i\frac{\pi}{2}} \end{pmatrix} \cdot \begin{pmatrix} phge^{-i\xi_1\pi} + ckfe^{-i\xi_2\pi} \\ +bhgJ_0(\sigma\pi) + dkfJ_0(\sigma\pi)e^{i\frac{\pi}{2}} \end{pmatrix}}{\left\{ (bhg + dkf) \cdot J_1(\sigma\pi) e^{-i(\omega t+\theta+\frac{\pi}{2})} \right\} \cdot \left\{ (bhg + dkf) \cdot J_1(\sigma\pi) e^{i(\omega t+\theta+\frac{\pi}{2})} \right\}} \tag{A.30}$$

Based on the function $e^{i\theta} = \cos\theta + i\sin\theta$, after simplification we get

$$OCSR = \frac{\begin{Bmatrix} c^2f^2k^2 + p^2g^2h^2 + 2pcfghk \cdot \cos(\xi_1 - \xi_2)\pi \\ +2J_0(\sigma\pi)\left[pbg^2h^2 \cdot \cos(\xi_1\pi) + ghbcfk \cdot \cos(\xi_2\pi) - pdfkgh \cdot \sin(\xi_1\pi) - f^2k^2cd \cdot \sin(\xi_2\pi) \right] \\ +(d^2f^2k^2 + b^2g^2h^2)J_0^2(\sigma\pi) \end{Bmatrix}}{\left\{ (dfk + bgh)^2 \cdot J_1^2(\sigma\pi) \right\}} \tag{A.31}$$

Equation (A.31) is the Eq. (2.2b).

1.4 Derivation of Eq. (2.3)

The optical carrier component beats with the first order component of RF signal will makes foremost contribution to the final desired electrical signal. Therefore the I_ω can be represented as

$$\begin{aligned} I_\omega &= \frac{\Re}{2}\cdot \mathrm{Re}(E_{oc}\cdot E_{-\omega}^{*} + E_{oc}^{*}\cdot E_{-\omega}) \\ &= \frac{\Re\cdot t_{ff}\cdot E_0^{\,2}\,\mathrm{Re}\left\{\left[ae^{i\xi_1\pi} + ae^{i\xi_2\pi} + \sqrt{2}rJ_0(\sigma\pi)e^{-i\frac{\pi}{4}}\right]\cdot\left[-rJ_1(\sigma\pi)e^{i(\omega t+\theta-\frac{1}{2}\pi)}\right]\right\}}{2} \\ &= \frac{\Re\cdot t_{ff}\cdot E_0^{\,2}}{2}\mathrm{Re}\left\{\begin{bmatrix} a\cos(\xi_1\pi)+i\cdot a\sin(\xi_1\pi)+ \\ a\cos(\xi_2\pi)+i\cdot a\sin(\xi_2\pi)+ \\ (1-i)rJ_0(\sigma\pi)\end{bmatrix}\cdot\left[i\cdot rJ_1(\sigma\pi)\cdot\left(\cos(\omega t+\theta)+i\sin(\omega t+\theta)\right)\right]\right\} \end{aligned} \tag{A.32}$$

where $\Re$ is the responsivity of the photodetector.

After simplification we get

$$I_\omega = \frac{\Re t_{ff} E_0^{\,2}}{2}\begin{bmatrix} -ar\left(J_1(\sigma\pi)\cos\left(\omega t+\theta+\xi_1\pi-\frac{\pi}{2}\right)+J_1(\sigma\pi)\cos\left(\omega t+\theta+\xi_2\pi-\frac{\pi}{2}\right)\right) \\ +\sqrt{2}r^2J_0(\sigma\pi)J_1(\sigma\pi)\cos\left(\omega t+\theta+\frac{\pi}{4}\right)\end{bmatrix} \tag{A.33}$$

Equation (A.33) is Eq. (2.3).

APPENDIX-B

Detailed Derivation for the modulator driven by Two RF Signals

2.1 Derivation of Eq. (2.5)

Now we consider the situation when two RF signals $RF_1=\sqrt{2}V_{RF}[\cos(\omega_1 t+\theta_1)]$ and $RF_2=\sqrt{2}V_{RF}[\cos(\omega_2 t+\theta_2)]$ are applied to the two parallel dual-electrode MZMs, where V_{RF}, ω_1, ω_2, θ_1 and θ_2 are modulation voltage, frequency, and phase of the RF input signal.

For the first MZM, RF signals are applied on the lower branch of the MZM-1, i.e. V_{RF_lower1}, and no signal applied on upper branch, i.e. $V_{RF\_upper1}=0$. The RF applied voltage applied to lower branch of the dual-electrode MZM is given by

$$V_{RF\_lower1}=V_{RF}\left[\cos(\omega_1 t+\theta_1)+\cos(\omega_2 t+\theta_2)\right] \tag{B.1}$$

Because we use same voltage of the DC bias as one RF signal, which means we set $V_{DC\_lower1}=0$ and tune the V_{DC_upper1}; and only the voltage of RF bias V_{RF_lower1} change, therefore, based on Eqs. (A.1)-(A.3) and (B.1), and notice that we choose negative mode of MZM which means the phase of lower branch will be negative, we can obtain

$$E_{out1}(t) = \frac{E_{in}\sqrt{t_{ff}}}{2}(ae^{i\varphi_{upper1}} + re^{-i\varphi_{lower1}}) \tag{B.2}$$

$$\varphi_{upper1} = \frac{\pi}{V_\pi}V_{DC\_upper1} + \frac{\pi}{V_\pi}V_{RF\_upper1} = \frac{\pi}{V_\pi}V_{DC\_upper1} \tag{B.3}$$

$$\varphi_{lower1} = \frac{\pi}{V_\pi}V_{DC\_lower1} + \frac{\pi}{V_\pi}V_{RF\_lower1} = \frac{V_{RF}\pi}{V_\pi}\left[\cos(\omega_1 t + \theta_1) + \cos(\omega_2 t + \theta_2)\right] \tag{B.4}$$

Substituting Eq. (B.3) and Eq. (B.4) into Eq. (B.2) we can obtain,

$$E_{out1}(t) = \frac{\sqrt{t_{ff}}}{2}E_0 e^{i\omega_c t}\left\{ae^{i\frac{V_{DC\_upper1}}{V_\pi}\pi} + re^{-i\frac{V_{RF}}{V_\pi}\pi\left[\cos(\omega_1 t+\theta_1)+\cos(\omega_2 t+\theta_2)\right]}\right\} \tag{B.5}$$

For the second MZM, RF signals are applied on the lower branch of the MZM-2, i.e. V_{RF_lower2} and no signal applied on upper branch, i.e. $V_{RF\_upper2} = 0$. The RF applied voltage applied to lower branch of the second dual-electrode MZM is given by

$$V_{RF\_lower2} = V_{RF}\left[\cos(\omega_1 t + \theta_1 - \frac{\pi}{2}) + \cos(\omega_2 t + \theta_2 - \frac{\pi}{2})\right] \tag{B.6}$$

Because we use same voltage of the DC bias as one RF signal, which means we set $V_{DC\_lower2} = \frac{V_\pi}{2}$ and tune the V_{DC_upper2}; and only the voltage of RF bias V_{RF_lower2} change, therefore, based on Eq. (A.1), Eq. (A.2), Eq. (A.3), and Eq. (B.6) we can obtain

$$E_{out2}(t) = \frac{E_{in}\sqrt{t_{ff}}}{2}(ae^{i\varphi_{upper2}} + re^{-i\varphi_{lower2}}) \tag{B.7}$$

$$\varphi_{upper2} = \frac{\pi}{V_\pi} V_{DC\_upper2} + \frac{\pi}{V_\pi} V_{RF\_upper2} = \frac{\pi}{V_\pi} V_{DC\_upper2} \tag{B.8}$$

$$\varphi_{lower2} = \frac{\pi}{V_\pi} V_{DC\_lower2} + \frac{\pi}{V_\pi} V_{RF\_lower2} = \pi \left\{ \frac{V_{RF}}{V_\pi} \left[\cos(\omega_1 t + \theta_1 - \frac{\pi}{2}) + \cos(\omega_2 t + \theta_2 - \frac{\pi}{2}) \right] + \frac{1}{2} \right\} \tag{B.9}$$

Substituting Eq. (B.8) and Eq. (B.9) into Eq. (B.7) we can obtain,

$$E_{out2}(t) = \frac{\sqrt{t_{ff}}}{2} E_0 e^{i\omega_c t} \left\{ a e^{i\frac{V_{DC\_upper2}}{V_\pi}\pi} + r e^{-i\frac{\pi}{2}} e^{-i\frac{V_{RF}}{V_\pi}\pi\left[\cos(\omega_1 t+\theta_1-\frac{\pi}{2})+\cos(\omega_2 t+\theta_2-\frac{\pi}{2})\right]} \right\} \tag{B.10}$$

After combining E_{out1} and E_{out2} together, the density of optical field for our considered technology is given by

$$E_{total}(t) = \frac{\sqrt{t_{ff}}}{2} E_0 e^{i\omega_c t} \left\{ a e^{i\xi_1\pi} + a e^{i\xi_2\pi} + r e^{-i\sigma\pi[\cos(\omega_1 t+\theta_1)+\cos(\omega_2 t+\theta_2)]} + r e^{-i\frac{\pi}{2}} e^{-i\sigma\pi\left[\cos(\omega_1 t+\theta_1-\frac{\pi}{2})+\cos(\omega_2 t+\theta_2-\frac{\pi}{2})\right]} \right\} \tag{B.11}$$

where $\sigma = \frac{V_{RF}}{V_\pi}$, $\xi_1 = \frac{V_{DC\_upper1}}{V_\pi}$, and $\xi_2 = \frac{V_{DC\_upper2}}{V_\pi}$.

By applying the Jacobi-Anger expansion $e^{iz\cos\varphi} = \sum_{n=-\infty}^{\infty} i^n J_n(z) e^{in\varphi}$ to Eq. (B.11), we can get

$$E_{total}(t) = \frac{\sqrt{t_{ff}}}{2} E_0 e^{i\omega_c t} \left\{ \begin{array}{l} a e^{i\xi_1\pi} + a e^{i\xi_2\pi} \\ + r \sum_{m=-\infty}^{\infty} \sum_{n=-\infty}^{\infty} i^{m+n} J_m(\sigma\pi) J_n(\sigma\pi) e^{i[m(\omega_1 t+\theta_1+\pi)+n(\omega_2 t+\theta_2+\pi)]} \\ + r \sum_{m=-\infty}^{\infty} \sum_{n=-\infty}^{\infty} i^{m+n} J_m(\sigma\pi) J_n(\sigma\pi) e^{i\left[m(\omega_1 t+\theta_1+\frac{\pi}{2})+n(\omega_2 t+\theta_2+\frac{\pi}{2})-\frac{\pi}{2}\right]} \end{array} \right\} \tag{B.12}$$

Equation (B.12) is the Eq. (2.5).

2.2 Derivation of Eq. (2.6a)

From Eq. (B.12) we can get

$$E_{-\omega_1} = \frac{\sqrt{t_{ff}}}{2} E_0 e^{i\omega_c t} \begin{Bmatrix} ri^{-1} J_0(\sigma\pi) J_{-1}(\sigma\pi) e^{i[-1(\omega_1 t+\theta_1+\pi)]} \\ +ri^{-1} J_0(\sigma\pi) J_{-1}(\sigma\pi) e^{i\left[-1(\omega_1 t+\theta_1+\frac{\pi}{2})-\frac{\pi}{2}\right]} \end{Bmatrix} (when\ m=-1,\ n=0)$$
$$= \sqrt{t_{ff}} E_0 e^{i\omega_c t} \left\{ irJ_0(\sigma\pi) J_1(\sigma\pi) e^{-i(\omega_1 t+\theta_1+\pi)} \right\} \quad \text{(B.13)}$$

$$E_{-\omega_2} = \frac{\sqrt{t_{ff}}}{2} E_0 e^{i\omega_c t} \begin{Bmatrix} ri^{-1} J_0(\sigma\pi) J_{-1}(\sigma\pi) e^{i[-1(\omega_2 t+\theta_2+\pi)]} \\ +ri^{-1} J_0(\sigma\pi) J_{-1}(\sigma\pi) e^{i\left[-1(\omega_2 t+\theta_2+\frac{\pi}{2})-\frac{\pi}{2}\right]} \end{Bmatrix} (when\ m=0,\ n=-1)$$
$$= \sqrt{t_{ff}} E_0 e^{i\omega_c t} \left\{ irJ_0(\sigma\pi) J_1(\sigma\pi) e^{-i(\omega_2 t+\theta_2+\pi)} \right\} \quad \text{(B.14)}$$

$$E_{oc} = \frac{\sqrt{t_{ff}}}{2} E_0 e^{i\omega_c t} \left\{ e^{i\xi_1\pi} + e^{i\xi_2\pi} + \sqrt{2} rJ_0^{\,2}(\sigma\pi) e^{-i\frac{\pi}{4}} \right\} (when\ m=0,\ n=0) \quad \text{(B.15)}$$

Because $E_{-\omega_1}$ and $E_{-\omega_2}$ have the totally same coefficients, we still can define the OCSR of the two RF signals by one mathematical expression. For signal RF_1, the optical carrier-to-sideband ratio in power is obtained

$$OCSR = \frac{|E_{oc}|^2}{|E_{-\omega_1}|^2} = \frac{a^2 + a^2\cos(\xi_1 - \xi_2)\pi + r^2 J_0^4(\sigma\pi) + arJ_0^2(\sigma\pi)\left[\cos\xi_1\pi + \cos\xi_2\pi - \sin\xi_1\pi - \sin\xi_2\pi\right]}{2r^2 J_1^2(\sigma\pi) J_0^2(\sigma\pi)} \quad \text{(B.16)}$$

We can obtain the totally same OCSR for the RF_2.

2.3 Derivation of Eq. (2.6b)

Because we need to measure the impact of combiner-splitter imbalance and extinction ratio imbalance of the first MZM and second MZM in simulation part, therefore we consider these parameters and define them by: splitter coupling factor k_{in}, combiner coupling factor k_{out}. ER_1 and ER_2 are the extinction ration of the first and second dual-electrode MZM, respectively. For calculating reason, we define $h=\sqrt{k_{in}}$, $k=\sqrt{1-k_{in}}$, $f=\sqrt{k_{out}}$, $g=\sqrt{1-k_{out}}$, $p=\frac{1+\sqrt{ER_1}}{\sqrt{2(ER_1+1)}}$, $b=\sqrt{1-p^2}$, $c=\frac{1+\sqrt{ER_2}}{\sqrt{2(ER_2+1)}}$ and $d=\sqrt{1-c^2}$. Consequently, they can be grouped into 4 pairs: splitter pair, i.e. h and k; combiner pair, i.e. f and g; upper branch and lower branch power split ratio for the first dual-electrode MZM, i.e. a and b; upper branch and lower branch power split ratio for the second dual-electrode MZM, i.e. c and d.

For the first dual-electrode MZM, we use the same RF bias and DC bias as ideal situation, thus we can get Eq. (B.2), Eq. (B.3) and Eq. (B.4). However, the amplitude of the E_{in} signal will change. For example, consider MZM-1, at first, the E_{in} pass the splitting coupler upper ($h\cdot E_{in}$), then it goes through the upper branch of the first dual-electrode MZM ($p\cdot h\cdot E_{in}$), finally, it pass the combining coupler ($p\cdot h\cdot g\cdot E_{in}$). Therefore, we get

$$\mathrm{E}_{\mathrm{upper1}} = p \cdot h \cdot g \cdot E_{in} = \frac{phg\sqrt{t_{ff}}}{\sqrt{2}} E_0 e^{i\omega_c t} e^{i\frac{V_{DC\_upper1}}{V_\pi}\pi} \tag{B.17a}$$

Using the same scenario we get

$$\mathrm{E}_{\mathrm{lower1}} = \frac{bhg\sqrt{t_{ff}}}{\sqrt{2}} E_0 e^{i\omega_c t} e^{-i\frac{V_{DC\_lower1}}{V_\pi}\pi} \tag{B.17b}$$

Using Eq. (B.17a) and Eq. (B.17b) we get

$$E_{out1}(t) = E_{upper1} + E_{lower1} = \frac{\sqrt{t_{ff}}}{\sqrt{2}} E_0 e^{i\omega_c t} \left\{ phge^{i\xi_1\pi} + bhge^{-i\sigma\pi[\cos(\omega_1 t+\theta_1)+\cos(\omega_2 t+\theta_2)]} \right\} \tag{B.18}$$

where $\sigma = \frac{V_{RF}}{V_\pi}$ and $\xi_1 = \frac{V_{DC\_upper1}}{V_\pi}$.

For the second dual-electrode MZM, we use the same RF bias and DC bias as ideal situation, thus we can get Eq. (B.7), Eq. (B.8) and Eq. (B.9). However, the amplitude of the E_{in} signal will change. For example, at first, the E_{in} pass the splitting coupler ($k \cdot E_{in}$), then it goes through the upper branch of the first dual-electrode MZM ($c \cdot k \cdot E_{in}$), finally, it pass the combining coupler ($c \cdot k \cdot f \cdot E_{in}$). Therefore, we get

$$\mathrm{E}_{\mathrm{upper2}} = \frac{c \cdot k \cdot f \cdot \sqrt{t_{ff}}}{\sqrt{2}} \cdot E_0 e^{i\omega_c t} e^{i\frac{V_{DC\_upper2}}{V_\pi}\pi} \tag{B.19a}$$

Using the same scenario we get

$$\mathrm{E}_{\mathrm{lower2}} = \frac{d \cdot k \cdot f \cdot \sqrt{t_{ff}}}{\sqrt{2}} \cdot E_0 e^{i\omega_c t} e^{-i(\frac{V_{DC\_lower2}}{V_\pi}+\frac{1}{2})\pi} \tag{B.19b}$$

Using Eq. (B.19a) and Eq. (B.19b) we get

$$E_{out2}(t) = E_{upper2} + E_{lower2} = \frac{\sqrt{t_{ff}}}{\sqrt{2}} E_0 e^{i\omega_c t} \left\{ ckfe^{i\xi_2 \pi} + dkfe^{-i\frac{\pi}{2}} e^{-i\sigma\pi\left[\cos(\omega_1 t+\theta_1-\frac{\pi}{2})+\cos(\omega_2 t+\theta_2-\frac{\pi}{2})\right]} \right\}$$

(B.20)

Where $\sigma = \frac{V_{RF}}{V_\pi}$ and $\xi_2 = \frac{V_{DC\_upper2}}{V_\pi}$.

According to Eq. (B.18) and Eq. (B.20) we can get

$$\begin{aligned} E_{total}(t) &= E_{out1} + E_{out2} \\ &= \frac{\sqrt{t_{ff}}}{\sqrt{2}} E_0 e^{i\omega_c t} \left\{ phge^{i\xi_1 \pi} + ckfe^{i\xi_2 \pi} + bhge^{-i\sigma\pi\left[\cos(\omega_1 t+\theta_1)+\cos(\omega_2 t+\theta_2)\right]} + dkfe^{-i\frac{\pi}{2}} e^{-i\sigma\pi\left[\cos(\omega_1 t+\theta_1-\frac{\pi}{2})+\cos(\omega_2 t+\theta_2-\frac{\pi}{2})\right]} \right\} \end{aligned}$$

(B.21)

By applying the Jacobi-Anger expansion $e^{iz\cos\varphi} = \sum_{n=-\infty}^{\infty} i^n J_n(z) e^{in\varphi}$ to Eq. (B.21), we can get

$$E_{total}(t) = \frac{\sqrt{t_{ff}}}{\sqrt{2}} E_0 e^{i\omega_c t} \left\{ \begin{array}{l} phge^{i\xi_1 \pi} + ckfe^{i\xi_2 \pi} \\ +bhg \sum_{m=-\infty}^{\infty} \sum_{n=-\infty}^{\infty} i^{m+n} J_m(\sigma\pi) J_n(\sigma\pi) e^{i\left[m(\omega_1 t+\theta_1+\pi)+n(\omega_2 t+\theta_2+\pi)\right]} \\ +dkf \sum_{m=-\infty}^{\infty} \sum_{n=-\infty}^{\infty} i^{m+n} J_m(\sigma\pi) J_n(\sigma\pi) e^{i\left[m(\omega_1 t+\theta_1+\frac{\pi}{2})+n(\omega_2 t+\theta_2+\frac{\pi}{2})-\frac{\pi}{2}\right]} \end{array} \right\}$$

(B.22)

When m=0 and n=0 the optical carrier is obtained

$$E_{oc}=\frac{\sqrt{t_{ff}}}{\sqrt{2}}E_0e^{i\omega_c t}\begin{Bmatrix} phge^{i\xi_1\pi}+ckfe^{i\xi_2\pi} \\ +bhgJ_0{}^2(\sigma\pi)+dkfJ_0{}^2(\sigma\pi)e^{-i\frac{\pi}{2}} \end{Bmatrix} \tag{B.23}$$

When m=-1 and n=0, the lower sideband fundamental component of RF_1 signal is as follow

$$\begin{aligned} E_{-\omega_1}&=\frac{\sqrt{t_{ff}}}{\sqrt{2}}E_0e^{i\omega_c t}\begin{Bmatrix} bhg\cdot i^{-1}J_0(\sigma\pi)J_{-1}(\sigma\pi)e^{i[-1(\omega_1 t+\theta_1+\pi)]} \\ +dkf\cdot i^{-1}J_0(\sigma\pi)J_{-1}(\sigma\pi)e^{i\left[-1(\omega_1 t+\theta_1+\frac{\pi}{2})-\frac{\pi}{2}\right]} \end{Bmatrix} \\ &=\frac{\sqrt{t_{ff}}}{\sqrt{2}}E_0e^{i\omega_c t}\left\{i\cdot(bhg+dkf)\cdot J_0(\sigma\pi)J_1(\sigma\pi)e^{-i(\omega_1 t+\theta_1+\pi)}\right\} \end{aligned} \tag{B.24}$$

According to Eq. (B.23) and Eq. (B.24) we can calculate the OCSR by

$$OCSR=\frac{|E_{oc}|^2}{|E_{-\omega_1}|^2}=\frac{\begin{pmatrix} ahge^{i\xi_1\pi}+ckfe^{i\xi_2\pi} \\ +bhgJ_0{}^2(\sigma\pi)+dkfJ_0{}^2(\sigma\pi)e^{-i\frac{\pi}{2}} \end{pmatrix}\cdot\begin{pmatrix} ahge^{-i\xi_1\pi}+ckfe^{-i\xi_2\pi} \\ +bhgJ_0{}^2(\sigma\pi)+dkfJ_0{}^2(\sigma\pi)e^{i\frac{\pi}{2}} \end{pmatrix}}{\left\{i\cdot(bhg+dkf)\cdot J_0(\sigma\pi)J_1(\sigma\pi)e^{-i(\omega_1 t+\theta_1+\pi)}\right\}\cdot\left\{-i\cdot(bhg+dkf)\cdot J_0(\sigma\pi)J_1(\sigma\pi)e^{i(\omega_1 t+\theta_1+\pi)}\right\}} \tag{B.25}$$

Based on the function $e^{i\theta}=\cos\theta+i\sin\theta$, after simplification we get

$$OCSR = \frac{\left\{\begin{array}{l} c^2f^2k^2 + a^2g^2h^2 + 2acfghk \cdot \cos(\xi_1 - \xi_2)\pi \\ +2J_0^{\,2}(\sigma\pi)\left[abg^2h^2 \cdot \cos(\xi_1\pi) + ghbcfk \cdot \cos(\xi_2\pi) - adfkgh \cdot \sin(\xi_1\pi) - f^2k^2cd \cdot \sin(\xi_2\pi)\right] \\ +(d^2f^2k^2 + b^2g^2h^2)J_0^{\,4}(\sigma\pi) \end{array}\right\}}{\left\{(dfk + bgh)^2 \cdot J_0^{\,2}(\sigma\pi)J_1^{\,2}(\sigma\pi)\right\}} \tag{B.26}$$

Equation (B.26) is the Eq. (2.6b).

2.4 Derivation of Eq. (2.7)

The optical carrier component beats with the first order component of RF_1 signal will make foremost contribution to the final desired electrical signal. According to Eq. (B.13) and Eq. (B.15), the I_{ω_1} can be represented as

$$\begin{aligned} I_{\omega_1} &= \frac{\Re}{2} \cdot \mathrm{Re}(E_{oc} \cdot E_{-\omega_1}{}^{*} + E_{oc}{}^{*} \cdot E_{-\omega_1}) \\ &= \frac{\Re \cdot t_{ff'} \cdot E_0^{\,2}}{2} \mathrm{Re}\left\{\left[ae^{i\xi_1\pi} + ae^{i\xi_2\pi} + \sqrt{2}rJ_0^{\,2}(\sigma\pi)e^{-i\frac{\pi}{4}}\right] \cdot \left[-rJ_0(\sigma\pi)J_1(\sigma\pi)e^{i(\omega_1 t + \theta_1 - \frac{1}{2}\pi)}\right]\right\} \\ &= \frac{\Re \cdot t_{ff'} \cdot E_0^{\,2}}{2} \mathrm{Re}\left\{\left[\begin{array}{l} a\cos(\xi_1\pi) + i \cdot a\sin(\xi_1\pi) + \\ a\cos(\xi_2\pi) + i \cdot a\sin(\xi_2\pi) + \\ (1-i)rJ_0^{\,2}(\sigma\pi) \end{array}\right] \cdot \left[i \cdot rJ_0(\sigma\pi)J_1(\sigma\pi) \cdot \left(\cos(\omega_1 t + \theta_1) + i\sin(\omega_1 t + \theta_1)\right)\right]\right\} \end{aligned} \tag{B.27}$$

After simplification we get

$$I_{\omega_1}=\frac{\Re t_{ff}E_0^{\,2}}{2}\left[\begin{array}{l}-arJ_0(\sigma\pi)J_1(\sigma\pi)\cos(\omega_1 t+\theta_1+\xi_1\pi-\frac{\pi}{2})-arJ_0(\sigma\pi)J_1(\sigma\pi)\cos(\omega_1 t+\theta_1+\xi_2\pi-\frac{\pi}{2})\\+\sqrt{2}r^2J_0^{\,3}(\sigma\pi)J_1(\sigma\pi)\cos(\omega_1 t+\theta_1+\frac{\pi}{4})\end{array}\right]$$

(B.28)

Equation (B.28) is Eq. (2.7a).

Using same method we can get

$$I_{\omega_2}=\frac{\Re t_{ff}E_0^{\,2}}{2}\left[\begin{array}{l}-arJ_0(\sigma\pi)J_1(\sigma\pi)\cos(\omega_2 t+\theta_2+\xi_1\pi-\frac{\pi}{2})-arJ_0(\sigma\pi)J_1(\sigma\pi)\cos(\omega_2 t+\theta_2+\xi_2\pi-\frac{\pi}{2})\\+\sqrt{2}r^2J_0^{\,3}(\sigma\pi)J_1(\sigma\pi)\cos(\omega_2 t+\theta_2+\frac{\pi}{4})\end{array}\right]$$

(B.29)

Equation (B.29) is Eq. (2.7b).

2.5 Derivation of Eq. (2.8)

To obtain the RF signals at frequency ω_1 by photo-detection, the beats include the light at $-\omega_1$ beating with optical carrier, the light at $-\omega_2$ beating with the light at $-\omega_2+\omega_1$, and the light at $-2\omega_1+\omega_2$ beating with the light at $-\omega_1+\omega_2$. Other distortion terms like high order distortions can be removed by filter; therefore we consider the last 2 beats as noise and use $I_{IMD\omega_1}$ to express

$$I_{IMD\omega_1} = \frac{\Re}{2} \cdot \mathrm{Re}\left\{ E_{-\omega_2} \cdot E_{-\omega_2+\omega_1}{}^{*} + E_{-\omega_2}{}^{*} \cdot E_{-\omega_2+\omega_1} + E_{-2\omega_1+\omega_2} \cdot E_{-\omega_1+\omega_2}{}^{*} + E_{-2\omega_1+\omega_2}{}^{*} \cdot E_{-\omega_1+\omega_2} \right\} \quad \text{(B.30)}$$

Based on Eq. (B.12), we can calculate the $E_{-\omega_2}$ when m=0 and n=-1,

$$\begin{aligned} E_{-\omega_2} &= \frac{\sqrt{t_{ff}}}{2} E_0 e^{i\omega_c t} \begin{Bmatrix} r \cdot i^{-1} J_0(\sigma\pi) J_{-1}(\sigma\pi) e^{i[-1(\omega_2 t+\theta_2+\pi)]} \\ + r \cdot i^{-1} J_0(\sigma\pi) J_{-1}(\sigma\pi) e^{i\left[-1(\omega_2 t+\theta_2+\frac{\pi}{2})-\frac{\pi}{2}\right]} \end{Bmatrix} \\ &= \sqrt{t_{ff}} E_0 e^{i\omega_c t} \left\{ i \cdot r \cdot J_0(\sigma\pi) J_1(\sigma\pi) e^{-i(\omega_2 t+\theta_2+\pi)} \right\} \end{aligned} \quad \text{(B.31)}$$

Using same method we can get

$$E_{-\omega_2+\omega_1}{}^{*} = \frac{\sqrt{t_{ff}}}{2} E_0 e^{-i\omega_c t} \left\{ -r \cdot J_1{}^2(\sigma\pi) \cdot e^{i(\omega_2 t+\theta_2-\omega_1 t-\theta_1)} - r \cdot J_1{}^2(\sigma\pi) \cdot e^{i(\omega_2 t+\theta_2-\omega_1 t-\theta_1+\frac{\pi}{2})} \right\} \quad \text{(B.32)}$$

$$E_{-2\omega_1+\omega_2} = \sqrt{t_{ff}} E_0 e^{i\omega_c t} \left\{ -i \cdot r \cdot J_1(\sigma\pi) \cdot J_2(\sigma\pi) e^{i(\omega_2 t+\theta_2-2\omega_1 t-2\theta_1-\pi)} \right\} \quad \text{(B.33)}$$

$$E_{-\omega_1+\omega_2}{}^{*} = \frac{\sqrt{t_{ff}}}{2} E_0 e^{-i\omega_c t} \left\{ -r \cdot J_1{}^2(\sigma\pi) \cdot e^{i(\omega_1 t+\theta_1-\omega_2 t-\theta_2)} - r \cdot J_1{}^2(\sigma\pi) \cdot e^{i(\omega_1 t+\theta_1-\omega_2 t-\theta_2+\frac{\pi}{2})} \right\} \quad \text{(B.34)}$$

Based on Eqs. (B.30) ~ (B.34) we get

$$\begin{aligned} I_{IMD\omega_1} &= \frac{\Re}{2} \cdot \mathrm{Re}\left\{ E_{-\omega_2} \cdot E_{-\omega_2+\omega_1}{}^{*} + E_{-\omega_2}{}^{*} \cdot E_{-\omega_2+\omega_1} + E_{-2\omega_1+\omega_2} \cdot E_{-\omega_1+\omega_2}{}^{*} + E_{-2\omega_1+\omega_2}{}^{*} \cdot E_{-\omega_1+\omega_2} \right\} \\ &= \frac{\Re_{ff} E_0^2}{2} \mathrm{Re}\left\{ \begin{aligned} &\left[i \cdot r \cdot J_0(\sigma\pi) J_1(\sigma\pi) e^{-i(\omega_2 t+\theta_2+\pi)} \right] \cdot \left[-r \cdot J_1{}^2(\sigma\pi) \cdot e^{i(\omega_2 t+\theta_2-\omega_1 t-\theta_1)} - r \cdot J_1{}^2(\sigma\pi) \cdot e^{i(\omega_2 t+\theta_2-\omega_1 t-\theta_1+\frac{\pi}{2})} \right] \\ &+ \left[-i \cdot r \cdot J_1(\sigma\pi) \cdot J_2(\sigma\pi) e^{i(\omega_2 t+\theta_2-2\omega_1 t-2\theta_1-\pi)} \right] \cdot \left[-r \cdot J_1{}^2(\sigma\pi) \cdot e^{i(\omega_1 t+\theta_1-\omega_2 t-\theta_2)} - r \cdot J_1{}^2(\sigma\pi) \cdot e^{i(\omega_1 t+\theta_1-\omega_2 t-\theta_2+\frac{\pi}{2})} \right] \end{aligned} \right\} \end{aligned} \quad \text{(B.35)}$$

Transferring it to triangle form and simplifying, we get

$$I_{IMD\omega_1} = \frac{\Re t_{ff} E_0^{\ 2}}{2} \cos(\omega_1 t + \theta_1 + \frac{\pi}{4}) \left[-\sqrt{2} r^2 J_1^{\ 3}(\sigma\pi) J_0(\sigma\pi) + \sqrt{2} r^2 J_1^{\ 3}(\sigma\pi) J_2(\sigma\pi) \right] \quad \text{(B.36)}$$

Equation (B.36) is Eq. (2.8a).

Using same method we can get

$$I_{IMD\omega_2} = \frac{\Re t_{ff} E_0^{\ 2}}{2} \cos(\omega_2 t + \theta_2 + \frac{\pi}{4}) \left[-\sqrt{2} r^2 J_1^{\ 3}(\sigma\pi) J_0(\sigma\pi) + \sqrt{2} r^2 J_1^{\ 3}(\sigma\pi) J_2(\sigma\pi) \right] \quad \text{(B.37)}$$

for the RF signals at frequency ω_2. Equation (B.37) is Eq. (2.8b).

2.6 Derivation of Eq. (2.9)

The IMD3 current like $I_{-2\omega_1+\omega_2}$ is mainly contributed by the light at $-2\omega_1+\omega_2$ beating with optical carrier and the light at $-\omega_1$ beating with the light at $\omega_1-\omega_2$. Therefore we can obtain

$$I_{-2\omega_1+\omega_2} = \frac{\Re}{2} \cdot \mathrm{Re}\left\{ E_{-2\omega_1+\omega_2} \cdot E_{oc}^{\ *} + E_{-2\omega_1+\omega_2}^{\ *} \cdot E_{oc} + E_{-\omega_1} \cdot E_{\omega_1-\omega_2}^{\ *} + E_{-\omega_1}^{\ *} \cdot E_{\omega_1-\omega_2} \right\} \quad \text{(B.38)}$$

Based on equation (B.12), when m=-2 and n=1 we can get

$$E_{-2\omega_1+\omega_2} = \sqrt{t_{ff}} E_0 e^{i\omega_c t} \left\{ -i \cdot r \cdot J_1(\sigma\pi) \cdot J_2(\sigma\pi) e^{i(\omega_2 t + \theta_2 - 2\omega_1 t - 2\theta_1 - \pi)} \right\} \quad \text{(B.39)}$$

Using same method we obtain

$$E_{oc}^{\ *} = \frac{\sqrt{t_{ff}}}{2} E_0 e^{-i\omega_c t} \left\{ e^{-i\xi_1 \pi} + e^{-i\xi_2 \pi} + \sqrt{2} r J_0^{\ 2}(\sigma\pi) e^{i\frac{\pi}{4}} \right\} \quad \text{(B.40)}$$

$$E_{-\omega_1} = \sqrt{t_{ff}} E_0 e^{i\omega_c t} \left\{ i \cdot r \cdot J_0(\sigma\pi) J_1(\sigma\pi) e^{-i(\omega_1 t + \theta_1 + \pi)} \right\} \tag{B.41}$$

$$E_{-\omega_2+\omega_1}{}^{*} = \frac{\sqrt{t_{ff}}}{2} E_0 e^{-i\omega_c t} \left\{ -r \cdot J_1{}^2(\sigma\pi) \cdot e^{i(\omega_2 t + \theta_2 - \omega_1 t - \theta_1)} - r \cdot J_1{}^2(\sigma\pi) \cdot e^{i(\omega_2 t + \theta_2 - \omega_1 t - \theta_1 + \frac{\pi}{2})} \right\} \tag{B.42}$$

Based on Eqs. (B.38) ~ Eq. (B.42) we get

$$\begin{aligned}
I_{-2\omega_1+\omega_2} &= \frac{\Re}{2} \cdot \mathrm{Re}\left\{ E_{-2\omega_1+\omega_2} \cdot E_{oc}{}^{*} + E_{-2\omega_1+\omega_2}{}^{*} \cdot E_{oc} + E_{-\omega_1} \cdot E_{\omega_1-\omega_2}{}^{*} + E_{-\omega_1}{}^{*} \cdot E_{\omega_1-\omega_2} \right\} \\
&= \frac{\Re t_{ff} E_0{}^2}{2} \mathrm{Re} \left\{ \begin{array}{l} \left[-i \cdot r \cdot J_1(\sigma\pi) \cdot J_2(\sigma\pi) e^{i(\omega_2 t + \theta_2 - 2\omega_1 t - 2\theta_1 - \pi)} \right] \cdot \left[e^{-i\xi_1\pi} + e^{-i\xi_2\pi} + \sqrt{2} r J_0{}^2(\sigma\pi) e^{i\frac{\pi}{4}} \right] \\ + \left[i \cdot r \cdot J_0(\sigma\pi) J_1(\sigma\pi) e^{-i(\omega_1 t + \theta_1 + \pi)} \right] \cdot \left[-r \cdot J_1{}^2(\sigma\pi) \cdot e^{i(\omega_2 t + \theta_2 - \omega_1 t - \theta_1)} - r \cdot J_1{}^2(\sigma\pi) \cdot e^{i(\omega_2 t + \theta_2 - \omega_1 t - \theta_1 + \frac{\pi}{2})} \right] \end{array} \right. \\
&= \frac{\Re t_{ff} E_0{}^2}{2} \mathrm{Re} \left\{ \begin{array}{l} \left(-i \cdot r \cdot J_1(\sigma\pi) \cdot J_2(\sigma\pi) \left[\cos(\omega_2 t + \theta_2 - 2\omega_1 t - 2\theta_1 - \pi) + i \sin(\omega_2 t + \theta_2 - 2\omega_1 t - 2\theta_1 - \pi) \right] \right) \\ \cdot \left[\left(\cos(\xi_1\pi) - i \sin(\xi_1\pi) \right) + \left(\cos(\xi_2\pi) - i \sin(\xi_2\pi) \right) + (1+i) r J_0{}^2(\sigma\pi) \right] \\ + \left(i \cdot r \cdot J_0(\sigma\pi) J_1(\sigma\pi) \left[\cos(\omega_1 t + \theta_1 + \pi) - i \sin(\omega_1 t + \theta_1 + \pi) \right] \right) \\ \cdot \left(\begin{array}{l} -r \cdot J_1{}^2(\sigma\pi) \cdot \left[\cos(\omega_2 t + \theta_2 - \omega_1 t - \theta_1) + i \sin(\omega_2 t + \theta_2 - \omega_1 t - \theta_1) \right] \\ -r \cdot J_1{}^2(\sigma\pi) \cdot \left[\cos(\omega_2 t + \theta_2 - \omega_1 t - \theta_1 + \frac{\pi}{2}) + i \sin(\omega_2 t + \theta_2 - \omega_1 t - \theta_1 + \frac{\pi}{2}) \right] \end{array} \right) \end{array} \right.
\end{aligned} \tag{B.43}$$

After simplification, we get

$$I_{-2\omega_1+\omega_2} = \frac{\Re t_{ff} E_0{}^2}{2} \left[\begin{array}{l} arJ_1(\sigma\pi) J_2(\sigma\pi) \cos(2\omega_1 t - \omega_2 t + 2\theta_1 - \theta_2 + \xi_1\pi - \frac{\pi}{2}) \\ + arJ_1(\sigma\pi) J_2(\sigma\pi) \cos(2\omega_1 t - \omega_2 t + 2\theta_1 - \theta_2 + \xi_2\pi - \frac{\pi}{2}) \\ - \sqrt{2} r^2 J_1{}^3(\sigma\pi) J_0(\sigma\pi) \cos(2\omega_1 t - \omega_2 t + 2\theta_1 - \theta_2 + \frac{\pi}{4}) \\ - \sqrt{2} r^2 J_0{}^2(\sigma\pi) J_1(\sigma\pi) J_2(\sigma\pi) \cos(2\omega_1 t - \omega_2 t + 2\theta_1 - \theta_2 + \frac{\pi}{4}) \end{array} \right] \tag{B.44}$$

Using same method we can get

$$I_{-2\omega_2+\omega_1} = \frac{\Re t_{ff} E_0^{\,2}}{2} \left[\begin{array}{l} arJ_1(\sigma\pi)J_2(\sigma\pi)\cos(2\omega_2 t - \omega_1 t + 2\theta_2 - \theta_1 + \xi_1\pi - \frac{\pi}{2}) \\ +arJ_1(\sigma\pi)J_2(\sigma\pi)\cos(2\omega_2 t - \omega_1 t + 2\theta_2 - \theta_1 + \xi_1\pi - \frac{\pi}{2}) \\ -\sqrt{2}r^2 J_1^{\,3}(\sigma\pi)J_0(\sigma\pi)\cos(2\omega_2 t - \omega_1 t + 2\theta_2 - \theta_1 + \frac{\pi}{4}) \\ -\sqrt{2}r^2 J_0^{\,2}(\sigma\pi)J_1(\sigma\pi)J_2(\sigma\pi)\cos(2\omega_2 t - \omega_1 t + 2\theta_2 - \theta_1 + \frac{\pi}{4}) \end{array} \right] \quad \text{(B.45)}$$

Equation (B.44) is Eq. (2.9a); and equation (B.45) is Eq. (2.9b).

REFERENCES

[1] U. Gliese, S. Norskov, and T. N. Nielsen, "Chromatic dispersion in fiber-optic microwave and millimeter-wave links," *IEEE Trans. Microwave. Theory Tech.*, vol. 44, no. 10, pp. 1716–1724, Oct. 1996.

[2] G. H. Smith, D. Novak, and Z. Ahmed, "Technique for optical SSB generation to overcome dispersion penalties in fiber-radio systems," *Electronic Letters*, vol. 33, no. 1, pp. 74–75, Jan. 1997.

[3] H. Ogawa, D Polifko, and S Banba, "Millimeter-wave fiber optical systems for personal radio communication," *IEEE Trans. on Microwave Theory and Technique*, vol. 40, No. 12, pp.2294-2302, Dec. 1992.

[4] D. Wake, D. Johansson, and D. Moodie, "Passive Pico-cell: a new concept in wireless network infrastructure," *Electron. Lett.,* vol.33, pp.404-406, Feb. 1997.

[5] S. Tonda-Goldstein, D. Dolfi, J-P. Huignard, G. Charlet, and J. Chazelas, "Stimulated brillouin scattering for microwave signal modulation depth increase in optical links," *Electronics Letters*, vol. 36, no. 11, pp. 944-946, May 2000.

[6] R.D. Esman and K. J. Willians, "Wideband efficiency improvement of fiber optical systems by carrier subtraction," *IEEE Photon. Technol. Lett.*, vol. 7, no. 2, pp. 218-220, Feb.1995.

[7] M.J. LaGasse, W. Charczenko, M. C. Hamilton, and S. Thaniyanvarn, "Optical carrier filtering for high dynamic range fiber optic links," *Electronic Letters,* vol. 30, no. 25, pp. 2157-2158, Dec. 1994.

[8] C. Lim and M. Attygalle, "Analysis of Optical Carrier-to-Sideband Ratio for Improving Transmission Performance in Fiber-Radio Links," *IEEE Transactions on Microwave Theory and Techniques,* Vol. 54 No.5, May 2006, pp. 2181-2187.

[9] H. Toda, T. Yamashita, T. Kuri, and K. Kitayama, "25-GHz channel spacing DWDM multiplexing using an arrayed waveguide grating for 60-GHz band radio-on-fiber systems," in *Proc. Microw. Photon.,* Budapest, Hungary, Sep. 2003, pp. 287-290.

[10] H. Al-Raweshidy and S. Komaki, "Radio over fiber technologies for mobile communication networks", *Artech House*, Boston, London, pp. 188-414, 2002

[11] H. B. Kim, "Radio over fiber architecture," Electronic and Information Technology, University of Berlin, Berlin, M.Sc. thesis, Chapter 3, 2005.

[12] D. Wake, "Radio over Fiber Systems for Mobile Applications" in *Radio over Fiber Technologies for Mobile Communications Networks*, H, Al-Raweshidy, and S. Komaki, ed. (Artech House, Inc, USA, 2002).

[13] D. Wake and K. Beachman, "A Novel Switched Fiber Distributed Antenna System", in *Proceedings of European Conference on Optical Communications (ECOC'04)*, Vol. 5, 2004, pp. 132 – 135.

[14] J. Capmany, B. Ortega, D. Pastor, and S. Sales, "Discrete-Time Optical Processing of Microwave Signals", *Journal of Lightwave Technology*, Vol. 23, No. 2, 703 - 723, (2005).

[15] G. Maury, A. Hilt, T. Berceli, B. Cabon, and A. Vilcot, "Microwave Frequency Conversion Methods by Optical Interferometer and Photodiode", *IEEE Trans. On Microwave Theory and Techniques*, Vol. 45, No. 8, 1481 - 1485, (1997).

[16] D. Wake, S. Dupont, J-P. Vilcot, A. J. Seeds, "32-QAM Radio Transmission Over Multimode Fiber Beyond the Fiber Bandwidth", in *Proceedings of the IEEE International Topical Meeting on Microwave Photonics (MWP'01), 2001.*

[17] D. Wake, S. Dupont, C. Lethien, J-P. Vilcot, and D. Decoster, "Radiofrequency Transmission over Multimode Fiber for Distributed Antenna System Applications", *Electronic Letters*, Vol. 37, No. 17, pp 1087 – 1089 (2001).

[18] C. Liu, A. Seeds, J. Chadha, P. Stavrinou, G. Parry, M. Whitehead, A. Krysa, and J. Roberts, "Bi-Directional Transmission of Broadband 5.2 GHz Wireless Signals Over Fiber Using a Multiple-Quantum-Well Asymmetric Fabry-Perot Modulator/Photo detector", in *Proceedings of the Optical Fiber Communications (OFC) Conference.* 2003, Vol. 2, pp. 738 – 740.

[19] H. Al-Raweshidy, S. Komaki, ed., "Radio over Fiber Technology for the Next Generation" in *Radio over Fiber Technologies for Mobile Communications Networks*, (Artech House, Inc, USA, 2002).

[20] U. Gliese, T. N. Nielsen, S. Norskov, and K.E. Stubkjaer, "Multifunction Fiber-Optic Microwave Links Based on Remote Heterodyne Detection", *IEEE Trans. On Microwave Theory and Techniques*, Vol. 46, No. 5, 458-468, (1998)

[21] S. A. Havstad, A. B. Sahin, O. H. Adamczyk, Y. Xie, A. E. Willner, "Distance-Independent Microwave and Millimeter Wave Power Fading Compensation Using a Phase Diversity Configuration," *IEEE Photon. Technol. Lett.*, vol. 12, pp. 1052-1054, Aug. 2000.

[22] B. Masella, "Techniques for Nonlinear Distortion Suppression in Radio over Fiber Communication Systems," Department of Electrical and Computer Engineering, Concordia University, Montreal, PH.D. thesis, Chapter 2, 2009.

[23] G. H. Smith, D. Novak, and Z. Ahmed, "Technique for Optical SSB Generation to Overcome Dispersion Penalties in Fiber-radio Systems," *Electronics Letters,* vol. 33, pp. 74–75, Jan. 1997.

[24] W. W. Hu, K. Inagaki, T. Tanaka, T. Ohira and A. Xu, "High SNR 50 GHz Radio-over-Fiber Uplink System by Use of Low Biased Mach-Zehnder Modulator Technique," *Electronics Letters,* vol.42, pp.550-552, 2006.

[25] M. Zhou, "Novel Modulation Technique for Radio-over-Fiber Systems," Department of Electrical and Computer Engineering, Concordia University, Montreal, MASc. thesis, 2007.

[26] B. Hraimel, M. Twati, and Ke Wu "Closed-Form Dynamic Range Expression of Dual-Electrode Mach-Zehnder Modulator in Radio-over-Fiber WDM System" *J. Lightwave Technol.* 24, 2380-2387, 2006.

[27] J. Nayyer and H. Nagata, "Suppression of Thermal Drifts of High Speed Ti:LiNbO3 Optical Modulators," *IEEE Photonics Technol. Lett.*, vol.6, no. 8, pp.952-955, 1994.